THE LONG-TERM CHANGE OF EL NIÑO SOUTHERN OSCILLATION IN AN ENSEMBLE REANALYSIS AND CLIMATE COUPLED MODELS

A Dissertation

by

CHUNXUE YANG

Submitted to the Office of Graduate Studies of
Texas A&M University
in partial fulfillment of the requirements for the degree of

DOCTOR OF PHILOSOPHY

Approved by:

Co-Chairs of Committee,	Benjamin Giese
	Lixin Wu
Committee Members,	Ping Chang
	Courtney Schumacher
Head of Department,	Piers Chapman

December 2012

Major Subject: Oceanography

ABSTRACT

Long-term changes of El Niño/Southern Oscillation (ENSO) are studied with the ensemble run of Simple Ocean Data Assimilation (SODA 2.2.6) and the Coupled Model Intercomparison Project Phase 5 (CMIP5). An eight member ocean reanalyses (SODA 2.2.6) from 1871 to 2008 is produced by using forcing from eight ensemble members of an atmospheric reanalysis. The ensemble reanalysis shows that El Niño has prominent decadal variability. Weak El Niños occur throughout the entire record whereas the occurrence of strong El Niños varies, with strong El Niño at the beginning and end of the record. The strength of La Niña is weaker than for El Niño, and has less variability. Although for any given El Niño year all ensemble members show the occurrence of El Niño, in some ensemble members the El Niño is strong while in others it is weak. When the timing of the onset of Westerly Wind Bursts (WWBs) occurs earlier in the year and the strength of WWBs is stronger, strong El Niño occurs.

To study the importance of the background state in the tropical Pacific Ocean on ENSO, long-term trends of tropical Pacific SST, wind stress, subsurface temperature and the sub-tropical cells (STCs) are analyzed. The reanalysis shows that there is a slight cooling trend of SST in the central tropical Pacific due to an enhanced tropical Pacific circulation. Subsurface temperature also has a cooling trend. The STCs, which consist of equatorial upwelling, Ekman transport, extra-tropical subduction and pycnocline transport from the sub-tropical to the tropical region, strengthen from 1900 to 2008. When the STCs are accelerated, equatorial upwelling increases bringing cold water from

the subsurface that cools the surface.

ENSO variability is also analyzed in the CMIP5 historical experiments. Results show that most of the models have a realistic representation of the strength of ENSO; however, the location of warming generally extends too far to the west. Overall, properties of ENSO do not show a significant change in most of the CMIP5 models. One distinguishing difference between the CMIP5 models and SODA 2.2.6 is that ENSO in SODA 2.2.6 has prominent asymmetry between El Niño and La Niña, whereas ENSO in the CMIP5 models tends to have fairly symmetric El Niño and La Niña. In contrast with the reanalysis most of the CMIP5 models have warming trends at the surface and the transport of the STCs has a decreasing trend.

DEDICATION

To my family

ACKNOWLEDGEMENTS

I would like to sincerely thank my advisor, Dr. Benjamin Giese, for his guidance, understanding and patience during my studies at Texas A&M University. His mentorship provided me with great experiences that are very important to my long-term career goals. His encouragement and infectious enthusiasm have been major driving forces throughout my graduate studies. I would have never been able to finish my dissertation without his help and support. I appreciate his kindness and generosity especially the hospitality of his family. I enjoyed every moment that I spent with his family and I will never forget how welcome I felt when I first moved to a foreign country.

I would like to express my appreciation and thanks to my co-chair, Dr. Lixin Wu, who helped guide me to science. Without his guidance and encouragement I would have never started my scientific career. I appreciate the great opportunity he provided me to foster my career. His inspiration helped me trekking forward on the right path.

I would like to thank my committee member, Dr. Ping Chang, for his guidance throughout my graduate studies. I appreciate his encouragement and support in helping me push through my doctorial career. I would also like to thank Dr. Courtney Schumacher for the suggestions and support she provided for my research.

Many thanks also go to my friends, colleagues, and the department faculty and staff for making my time at Texas A&M University a great experience. I would also like

to extend my gratitude to the Chinese Scholarship Council that provided the financial support necessary for my graduate studies at Texas A&M University.

Finally, and most importantly, I would like to thank my family. Their love, support and encouragement helped me to get through the good as well as the bad times.

TABLE OF CONTENTS

Page

LIST OF FIGURES

Page

CHAPTER I

INTRODUCTION

Global warming has received great attention not only because of its scientific importance, but also because changing climate will have a significant impact on global economics and policy. Increasing concentrations of greenhouse gases, a major cause of global mean temperature rise, have been analyzed in coupled ocean and atmosphere models [*Meehl et al.,* 2007]. Understanding the response pattern of the climate system to global warming forcing helps us understand how climate change arises and will improve climate predictions. The response of tropical Pacific sea surface temperature (SST) to global warming forcing has been investigated because of its considerable significance to global climate, with impacts on global drought [*Schubert et al.*, 2004; *Seager et al.*, 2005], tropical cyclone activity [*Vecchi and Soden*, 2007a] and biological productivity [*Chavez et al.*, 2011]. However, there is still uncertainty about how the tropic Pacific Ocean will respond to global warming.

There are two scenarios for how the tropical Pacific Ocean will respond to global warming [*Vecchi et al.*, 2008]. In one scenario a warmer ocean reduces the zonal gradient of temperature and is accompanied by weaker easterly trade winds and the response is "El Niño-like". In the other scenario a strengthened gradient of temperature causes stronger than normal easterly trade winds, forcing a response that is "La Niña-like". Modeling studies yield ambiguous results as to what the tropical Pacific response to global warming will be. The Cane-Zebiak model displays a "La Niña-like" pattern in

the tropical Pacific [*Cane et al.*, 1997; *Clement et al.*, 1996] while some slab-ocean models and fully coupled General Circulation Models (GCMs) show warming signals over the eastern tropical Pacific consistent with an "El Niño-like" pattern [*Held and Soden*, 2006; *Knutson and Manabe*, 1995]. Analysis of global warming projections simulated with global climate models used for Intergovernmental Panel on Climate Change (IPCC) assessments present a consistent "El Niño-like" pattern with a weakening of the overturning atmospheric circulation [*DiNezio et al.*, 2009; *Liu et al.*, 2005]. Observations and reconstructed SST datasets similarly show a range of trends in the eastern equatorial Pacific that range from cooling to warming. The Hadley Centre SST version 2 (HadSST2), Minobe SST, and National Oceanic and Atmospheric Administration Extended Reconstructed SST version 3 (ERSSTv3) all exhibit warming trends in the central tropical Pacific, while there is a cooling trend in Hadley Centre sea ice and SST version 1 (HadISST1) and Kaplan Extended SST version 2 (Kaplanv2) [*Deser et al.*, 2010]. However, by analyzing reconstructed datasets on a seasonal scale, *Karnauskas et al.* [2009] show that in all datasets the tropical Pacific zonal SST gradient has strengthened from 1880 to 2005 during the boreal fall when the gradient is normally strongest. *Zhang et al.* [2010] show that the second empirical orthogonal function mode of tropical Pacific SST is characterized by cooling in the Pacific cold tongue but warming elsewhere in the tropical Pacific.

Differing physical mechanisms behind these two different responses have been proposed by previous studies. For the "El Niño-like" pattern, based on the mass and energy balances of the atmosphere, the zonal atmospheric meridional overturning

circulation has been weakening in response to global warming and the equatorial Pacific east-west SST gradient has been reduced [*Held and Soden*, 2006]. Based on the Clausius-Clapeyron equation, water vapor concentration in the atmosphere should increase 7% for each 1-°K increase in temperature with fixed humidity. However, the precipitation rate increases approximately 2% for each 1-°K increase in temperature [*Held and Soden*, 2006; *Knutson and Manabe*, 1995]. The differential rate between water vapor and precipitation in response to increasing temperature implies that the convective mass flux must decrease between the boundary layer and the free troposphere, which means that the atmospheric circulation must slow down. The weakening atmospheric zonal circulation (Walker Circulation) leads to a reduction of easterly winds and thus the tropical Pacific SST gradient [*Vecchi and Soden*, 2007b; *Vecchi et al.*, 2006].

For the "La Niña-like" pattern, *Clement et al.* [1996] proposed the "ocean dynamical thermostat". In this case a vertical heat flux through equatorial upwelling compensates for the imposed forcing over the eastern tropical Pacific Ocean, which results in colder temperature in the eastern tropical Pacific than in the western tropical Pacific Oceans. The zonal tropical SST gradient increases resulting in easterly winds anomalies that are further amplified by the Bejerknes feedback [*Bjerknes*, 1969]. The role of ocean dynamics in regulating tropical Pacific Ocean SST is also discussed by *Seager and Murtugudde* [1997] and *Cane et al.* [1997] in which coupled models are used.

Despite the debate between "El Niño-like" and "La Niña-like" responses of tropical Pacific climate to global warming, *Liu et al.* [2005] suggest that the latitudinal SST gradient is more robust than the zonal SST gradient, and so the mechanism associated with equatorial warming is fundamentally different from an "El Niño-like" response. Recent studies with global climate models suggest that mechanisms of thermocline change and precipitation impacts in response to global warming for tropical Pacific climate change are different from the response to El Niño [*DiNezio et al.*, 2010].

The other important reason to investigate the response of the tropical Pacific Ocean to global warming is that the background state change may affect the change of El Niño Southern Oscillation (ENSO), the most prominent climate phenomenon in the tropical Pacific Ocean. ENSO, which occurs every two to seven years is characterized by warming in the eastern tropical Pacific and is accompanied by weakening of easterly trade winds. ENSO is driven by coupled ocean-atmosphere processes, in which the ocean component is called "El Niño" and the atmospheric component is called "Southern Oscillation". El Niño was first used to describe the unusual warming phenomenon along the South American coast during Christmas. El Niño started to be widely used in the scientific community after scientists realized that El Niño is associated with a basin-scale warming temperature anomaly in the central and eastern tropical Pacific Ocean that extends far beyond the South American coast. The Southern Oscillation, described by *Walker* [1923, 1924] and *Walker and Bliss* [1932], is characterized by a seasaw in tropical Pacific sea level pressure (SLP) between Tahiti in the central Pacific and Darwin in Australia, and is associated with weakening and

strengthening of the easterly trades wind. *Bjerknes* [1969] subsequently found that El Niño is the ocean manifestation and the Southern Oscillation is the atmospheric manifestation of the same phenomenon.

Bjerknes [1969] proposed a positive ocean-atmosphere feedback involving the Walker Circulation. An initial warming of SST in the eastern and central tropical Pacific Ocean leads to reduction of the zonal tropical SST gradient and hence weakens the strength of the Walker Circulation. As the easterly trade winds weaken there is a reduction of the zonal SST gradient. This ocean-atmosphere positive feedback, often called the Bejerknes feedback, causes the warming state of ENSO (El Niño) in the tropical Pacific Ocean. The opposite phase of El Niño, called La Niña, is characterized by a cooling anomaly in the tropical Pacific cold tongue associated with strengthening of easterly trade winds. However, the Bejerknes feedback does not explain the phase change between El Niño and La Niña.

The physical mechanisms responsible for ENSO have been discussed in several studies. *Battisti and Hirst* [1989] and *Graham and White* [1988] argue that El Niño operates as a natural oscillator driven by stochastic coupled processes between ocean and atmosphere, while *Jin et al.* [1994] and *Tziperman et al.* [1994] suggest that ENSO is chaotic and is driven by the seasonal cycle. Mechanisms for the transition between El Niño and La Niña events also have been proposed, for example delayed oscillator theory [*Battisti and Hirst*, 1989], recharge and discharge oscillator theory [*Jin*, 1997], and the advective reflective oscillator theory [*Picaut et al.*, 1997].

Westerly wind bursts (WWBs), defined as a westerly anomaly with strength larger than $7ms^{-1}$ and duration of 5-20 days [*Giese and Harrison*, 1990], have been involved in the onset of many El Niño events. Studies that investigate the high frequency influence on ENSO [*Barnston et al.*, 1999; *Landsea and Knaff*, 2000] show that without WWBs forcing the forecast of ENSO intensity is not correct for the 1997-1998 El Niño event.

One reason to explore ENSO is that even though it originates in the tropical Pacific Ocean, it not only affects regional ecosystems, but also has larger effects on the global climate system. These impacts lead to influence on global economics and societies. During El Niño years, due to positive SST anomalies in the eastern and central tropical Pacific Ocean, the Walker Circulation shifts eastward. This leads to negative precipitation anomalies in the western Pacific resulting in drought in India and Australia and positive precipitation anomalies in South America. In contrast, during La Niña years, the Walker Circulation shifts westward resulting in positive precipitation anomalies in the western Pacific and negative precipitation anomalies in the eastern Pacific.

However, changes are not limited to the tropical Pacific Ocean. The change of atmospheric circulation due to ENSO affects global climate systems. Through the Pacific North American (PNA) pattern [*Horel and Wallace*, 1981; *Wallace and Gutzler*, 1981], geopotential anomalies propagate to North America, which result in a change of the Aleutian Low. During El Niño years northern United States and western Canada have a mild winter, whereas the southeast parts of the United States have positive

rainfall anomaly. During La Niña years, winter tends to be colder than normal in the northern United States, and is dry in the southeast. ENSO also has impacts on the tropical Atlantic Ocean [*Saravanan and Chang*, 2000]. Due to the connection between ENSO and the tropical Atlantic Ocean, European climate is affected indirectly during El Niño years, with cold and dry conditions during warm events in the northeastern regions and dry conditions over the Mediterranean. During La Niña years, winters tend to be warm across much of Europe.

Since ENSO plays an important role in global climate, ecosystems and societies, it is of great interest to document and understand ENSO variations. ENSO extremes are characterized by a weak east-west tropical Pacific SST gradient during El Niño and a strong SST gradient during La Niña. These surface changes are accompanied by changes of strength of the trade winds and the structure of subsurface ocean. Therefore, characteristics and variations of ENSO are strongly controlled by the background mean state [*Fedorov and Philander*, 2000; *Fedorov and Philander* 2001; *Neelin et al.*, 1994]. *Fedorov and Philander* [2001] propose that high-frequency, local SST modes result from SST changes due to reduced upwelling and advection (SST-mode) and that low-frequency, delayed oscillator SST modes depend on SST changes due to the adjustment of a deep thermocline (Thermocline-mode). Several other studies show that atmospheric damping associated with latent and sensible heat fluxes and long wave and short wave fluxes on SST anomalies tends to reduce ENSO variability [*Lloyd et al.*, 2009]. Atmospheric variability, associated with intraseasonal variability and the Madden-Julian Oscillation (MJO), is also important to trigger and amplify ENSO variability [*Gebbie et*

al., 2007; *Lengaigne et al.*, 2004; *Zavala-Garay et al.*, 2008]. *Matei et al.* [2008] suggest that sub-tropical South Pacific climate variations are very important to ENSO decadal modulation.

The mean climate of the tropical Pacific undergoes significant changes in response to global warming. However, there is no consensus about ENSO changes in a changing climate, especially in a warming climate. For example some studies show that the amplitude of El Niño increases in response to global warming [*Guilyardi*, 2006; *Merryfield*, 2006], while some other studies argue that there is no significant or little change for the overall properties of ENSO under global warming [*Philip and Van Oldenborgh*, 2006; *van Oldenborgh et al.*, 2005; *Zelle et al.*, 2005]. Using an ocean reanalysis, *Ray and Giese* [2012] found that there is no strong evidence that the strength, frequency, duration, location or direction of propagation of El Niño and La Niña change due to global warming from 1871 to 2008. Despite progress in understanding impacts of climate change on ENSO variations through different ocean and atmosphere processes, we are still not confident about whether ENSO activity will be amplified or damped, or the frequency and location will change [*Collins et al.*, 2010; *Latif and Keenlyside*, 2009; *Vecchi and Wittenberg*, 2010]. However, the response of ENSO to global warming is still an essential research topic, and analysis methods, numerical models, and observations need to be improved.

In terms of numerical models, it is important to determine how well coupled general circulation models (GCMs) represent ENSO. Compared to previous coupled models, some of the third coupled model intercomparison project (CMIP3) models used

for the fourth assessment report (AR4) of the Intergovernmental Panel on Climate Change (IPCC) realistically capture the background state and qualitatively capture ENSO without use of flux correction. Despite improvements, GCMs still have deficiencies in simulating the mean climate and annual cycle of the tropical Pacific [*Guilyardi et al.*, 2009]. One important issue that has not been solved is the simulation of the equatorial Pacific cold tongue in coupled models. Compared to observations, the modeled cold tongue is generally too narrow and extends too far west into the western tropical Pacific [*Latif et al.*, 2001]. The other common feature for coupled models is the simulation of a double intertropical convergence zone (ITCZ). The double ITCZ is associated with tropical cold bias and results in a precipitation bias. These climate models also have systematic errors in the simulated background mean state and ENSO variability [*Capotondi et al.*, 2006; *Guilyardi*, 2006; *Guilyardi et al.*, 2009]. *Capotondi et al.* [2006] show that in coupled models the simulated wind stress is too narrow merionally and extends too far west along the equator, which leads to strong but short duration ENSO. Several other studies argue that model errors come from atmospheric components, such as cloud-albedo feedback, greenhouse effects of water vapor feedback and convective cloud schemes, that contribute to inaccurate simulation of ENSO [*Braconnot et al.*, 2007; *Sun et al.*, 2009].

In addition to these parameterization errors the horizontal and vertical resolution in coupled models needs to be increased, especially over the tropics. In the tropical oceans, high-resolution models are needed to simulate small-scale ocean processes such as tropical instability waves, equatorial upwelling and boundary currents, which may

also affect the simulation of ENSO. The resolution of atmospheric models also needs to be increased to solve coupled processes over the tropics in order to improve ENSO simulation [*Guilyardi et al.*, 2004].

An important element that contributes to tropical Pacific SST variability comes from the Sub-tropical Cells (STCs), which consist of subduction of sub-tropical water into the equatorial thermocline, equatorial upwelling, and surface Ekman return flow from the tropical region to the sub-tropical region [*McCreary and Lu*, 1994]. Impacts of transport of the STCs on tropical Pacific SST have been analyzed by several studies [*Gu and Philander*, 1997; *Kleeman et al.*, 1999; *Schneider et al.*, 1999]. *Gu and Philander* [1997] argue that an SST anomaly due to a change of westerly winds in the higher latitude subducts into the ocean and is advected to the equatorial ocean through the lower branch of the STC. The SST anomaly transferred to the equatorial region results in a change of the equatorial thermocline and equatorial upwelling, and so affects equatorial SST.

However, *Schneider et al.* [1999] argue that SST anomalies formed at higher latitudes advected by the lower branch of the STC can not reach the equatorial region. *Kleeman et al.* [1999] found that decadal variability of the STC is in response to the tropical Pacific decadal mode through a change of equatorial upwelling. Using hydrographic data, *McPhaden and Zhang* [2002] found that the STCs weakened from the 1970s to the 1990s, resulting in a decreasing of equatorial upwelling, which is associated with a SST anomaly of about 0.8°C. However, the transport of the STC

rebounded from the 1990s to the 2000s, which is accompanied by a cooling tropical Pacific SST anomaly [*McPhaden and Zhang*, 2004].

Results from numerical models are consistent with observations. *Lee and Fukumori* [2003] show that interior and western boundary transports compensate for each other, and interior transport is more important to the decadal variability of tropical-sub-tropical exchange than western boundary transport. Using a coupled climate model, *Merryfield and Boer* [2005] show that STC transports are significant to tropical Pacific heat content, and STC variability is correlated with the tropical Pacific low frequency variability. Using an ocean general circulation model, *Lohmann and Latif* [2005] find that the variability of STC transports are important to drive tropical Pacific decadal mode. *Capotondi et al.* [2005] also find that STC convergence transports are strongly correlated with central and eastern tropical Pacific SST, and also with equatorial upwelling. *Cheng et al.* [2007], using an eddy resolving model show that STC variability is correlated with the tropical Pacific decadal mode. By analyzing climate models, *Zhang and McPhaden* [2006] find an anti-correlation between the STC transport and SST anomalies in the central and eastern tropical Pacific Ocean. Results from ocean reanalysis also agree with observations that STC variability is related to tropical Pacific SST anomaly, especially on interannual time scales [*Schott et al.*, 2007; *Schott et al.*, 2008].

Because of the short observational record of STCs it has been difficult to identify its decadal variability. There is a pressing need to identify and describe decadal STC variability. A recent study by *Wang and Cane* [2011] shows that in CMIP3 climate

models, the strength of the STC has a weakening trend in the Northern Hemisphere and a strengthening trend in the Southern Hemisphere. The change of the STC is associated with a change of large-scale surface wind stress over the tropical Pacific Ocean.

Due to the lack of observations, our ability to investigate tropical Pacific climate change has been hampered, especially before the1950s. However, scientists have started to create reconstructed SST data [*Kaplan et al.*, 1998; *Rayner et al.*, 2003], which is the combination of available temporal records of SST at some locations, with different numerical methods. A limitation of these reconstructed data is that the spatial pattern of SST variability does not change with time, which is not realistic. An alternative method is to use an ocean model to assimilate available observations to estimate the ocean state. Different data assimilation schemes have been developed and Simple Ocean Data Assimilation (SODA) [*Carton and Giese*, 2008; *Carton et al.*, 2000a; *Carton et al.*, 2000b] is used in this research.

A new version of SODA from 1871 to 2008 with 8 ensemble members is available. SODA uses forcing from the 20th century reanalysis version 2 (20CRv2) [*Compo et al.*, 2006; *Compo et al.*, 2011; *Whitaker et al.*, 2004]. The long record of coverage and ensemble experiments is helpful to investigate long-term change of tropical Pacific climate. The other advantage of SODA compared to reconstructed data is it has vertical structure of the ocean state, which helps us to investigate the role of ocean dynamics to tropical Pacific climate change.

Coupled models have been widely used in studies of tropical Pacific climate change, and recently the fifth phase of the Coupled Model Intercomparison Project

(CMIP5) for IPCC Fifth Assessment Report (AR5) is available. Despite developments of coupled models, a deficiency of coupled models still exists. Under recent efforts on model development of coupled models, the new set of coupled models, CMIP5, will help us to investigate tropical Pacific climate change with a new perspective. Since CMIP5 is also going to be used for climate prediction, the evaluation of coupled models is necessary, thus results from the CMIP5 are compared with SODA. Historical runs of CMIP5 cover from 1850 to 2005 and are used in this research to explore tropical Pacific climate change. The reason to use historical runs is that they are comparable to SODA from 1871 to 2008. Ensemble experiments are also conducted in the CMIP5 historical runs, which is also comparable to the SODA ensemble runs. The details of the CMIP5 are discussed in methods section.

The first objective of this research is to analyze long-term changes of the tropical Pacific climate, especially ENSO, in the last century. Since ocean dynamics play a significant role in regulating tropical Pacific SST, the second question is the role of ocean dynamics, especially the long-term change of tropical Pacific circulation, the STC, in tropical Pacific climate variability. Due to the limitation of observations, previous studies mainly focus on short-term variability of tropical Pacific climate change. The data in this research covers from 1865 to 2010 and gives us an opportunity to investigate long-term change of tropical Pacific climate. Reanalysis of the CMIP5 is also included, and the evaluation of the CMIP5 models will be helpful for climate predictions.

CHAPTER II

METHODS

Simple Ocean Data Assimilation (SODA)

To investigate tropical Pacific climate change, we use the SODA methodology [Carton and Giese, 2008] consisting of the Parallel Ocean Program (POP) [*Smith et al.*, 1992] ocean model and SODA software. SODA has been used in several studies [*Giese and Ray*, 2011; *Giese et al.*, 2010], however for this research a new version of SODA (SODA 2.2.6) is used. The ocean model is based on POP version 2.0.2 with a horizontal resolution that is 0.4°×0.25° with 40 vertical levels with 10-m spacing near the surface. The model covers the global domain with a distorted grid in the Northern Hemisphere to allow for a displaced North Pole in order to resolve the Arctic Ocean. The meridional resolution increases poleward to reduce the grid anisotropy that results from the Mercator coordinate grid due to the convergence of meridians at high latitudes. K-profile parameterization is used for vertical mixing, whereas biharmonic parameterization is used for horizontal mixing. River input is included with climatological seasonal discharge. There is no explicit sea ice model, however the surface heat flux is modified when the surface temperature reaches the freezing point of sea water.

The surface boundary conditions for the ocean model are provided from 20CRv2 (20th century reanalysis version 2) [*Compo et al.*, 2006; *Compo et al.*, 2011; *Whitaker et al.*, 2004]. The 20CRv2 reanalysis is used for forcing because it is the only global atmospheric reanalysis that extends back to the middle of the nineteenth century.

A detailed description of 20CRv2 is provided by *Compo et al.* [2011]. The model used by 20CRv2 is a coupled atmosphere land model based on the NCEP Global Forecast Systems (GFS) with a horizontal resolution of T62 and a vertical resolution of 28 hybrid sigma-pressure levels. The lower boundary conditions are provided by UK Met Office HadISST 1.1 dataset [*Rayner et al.*, 2003] including SST and sea ice concentration interpolated from monthly resolution. 20CRv2 only assimilates surface pressure observations from the International Surface Pressure Databank (ISPD) version 2. The observations of ISPD come from land stations, marine observations and tropical cyclone 'best track' pressure observations and reports. Sea Level Pressure (SLP) from marine observations is provided by International Comprehensive Ocean-Atmosphere Data Set (ICOADS) 2.4 for the period of 1952-2008 and ICOADS 2.5 for the period of 1871-1951. Tropical cyclone data is provided by the International Best Track Archive for Climate Stewardship (IBTrACs). Quality control procedures are conducted on ISPD observations before surface pressure is assimilated into model. The assimilation scheme used by 20CRv2 is an Ensemble Kalman Filter algorithm based on an ensemble square root filter [*Whitaker and Hamill*, 2002] and multi stream schemes are used to produce data efficiently. For each stream, an ensemble of 56 9-hour forecasts is generated and 56 6-hour analyses are produced. Since 20CRv2 is the first dataset attempting to generate a synoptic analysis back to 1871 when few observations were available, evaluation of the dataset is conducted by estimating the uncertainty of the analysis fields at every time step. Compared to independent observations such as radiosonde data and National

Weather Prediction (NWP) forecasts, 20CRv2 accurately captures much of the observed variability [*Compo et al.*, 2011].

The surface wind stress from atmospheric reanalysis is used for computing surface momentum fluxes, and solar radiation, specific humidity, cloud cover, 2m air temperature, precipitation and 10m wind speed are used for computing heat and fresh water fluxes.

In SODA 2.2.6, only SST from ICOADS 2.5 is assimilated, which is a prominent difference from previous versions of SODA. The temperature and salinity profile data is not assimilated to reduce spurious climate signals such as decadal climate variability resulting from the increasing number of measurements since the 1950s. Assimilation of observations is carried out using a sequential 10-day update cycle, and the model error covariance is determined from a simulation without assimilation. The procedure for the assimilation is as follows, a simulation for 5 days from time t to time t+5 is conducted. At day t+5 an analysis is performed to produce the estimation of temperature and salinity. Innovations are calculated as the difference between the analysis and the first guess. The model is restarted at day t and integrated to t+10 with temperature and salinity innovations added incrementally at every time step. At day t+10, the procedure is repeated. The model outputs 5-day averages that are mapped onto a uniform global 0.5°×0.5°horizontal grid with the horizontal grid spherical coordinate remapping and interpolate package of *Jones* [1999].

The other significant difference of SODA 2.2.6 from older versions is that ensemble experiments are conducted. We randomly selected 8 out of 56 ensemble

members of 20CRv2 reanalysis as boundary conditions, and the same assimilation procedure is conducted to produce 8 ensemble members of SODA assimilation. This is important because weather noise is averaged out when there are few observations (such as in the early part of the record), and so there is change in the statistics of the atmosphere ensemble average. An ensemble reanalysis also provides the uncertainty of climate variability that could be used as a benchmark to evaluate coupled climate models.

Coupled Model Intercomparison Project Phase 5 (CMIP5)

Climate models have been developed over the last decades, however, there has been little opportunity for scientists outside of the model groups to access these datasets. In the mid-1990s, the World Climate Research Programme (WCRP)/Climate Variability and Predictability (CLIVAR) Working Group on Coupled Models (WCGM) organized the first coupled model intercomparison project that included control runs and an idealized 1% per year CO2 increase experiments [*Meehl et al.*, 1997]. After the first phase of CMIP, there were subsequent projects such as CMIP2 and CMIP2+ [*Meehl et al.*, 2000; *Meehl et al.*, 2005]. The model output was collected and archived at the Program for Climate Model Diagnosis and Intercomparison (PCMDI). In 2003, in order to prepare the IPCC fourth assessment, the climate modeling committee of WCRP realized the need for a better organized CMIP project which brought the production of the third phase of CMIP, CMIP3. The fifth phase of CMIP, CMIP5, follows the highly successful CMIP3 effort by making a coordinated set of global coupled model

experiments. CMIP5 has a broader scope than the CMIP3, including not only long term integrations, but also near-term integrations (10-30 years) [*Taylor et al.*, 2011]. The long-term integrations typically start from pre-industrial control integrations. The near term integrations, also called decadal prediction experiments, are initialized with observations. It is also the first time that Earth System Models (ESMs) were incorporated into coupled model comparisons.

There are more than 20 model groups involved in the CMIP5 project. Here we use 12 models, these available at the time of writing. Description of the models is presented in Table 1. The historical runs are compared with the ocean reanalysis data that covers from 1871 to 2008. The historical run is forced by observed atmospheric composition changes (both anthropogenic and natural sources), and covers from the pre-industrial period to the present. Most of the models start the experiments from 1850 except for GFDL and HadCM3 that start in 1860. To assess the statistical significance of differences between different simulations and the differences between the simulations and observations, ensemble simulations have been conducted. Different models have different numbers of ensemble members (from as few as 3 to as many as 10) and the resolutions of the models are also different (Table 1). Most of the model groups provide the data on a regular grid. For those models that have output on irregular grids, Ferret is used to remap output to a regular 1°×1° grid.

Table 1. CMIP5 models description

Model	Institution	Ensemble Members	Resolution Atmosphere	Resolution Ocean	Reference
BCC-CSM1-1	Beijing Climate Center, China Meteorological Administration	3	T42, L26	Tripolar, 1° longitude × (1°-(1/3)°) latitude, L40	*Wu et al.* [2012]
CanESM2	Canadian Centre for Climate Modeling and Anaylsis	5	T63, L35	1.41°×0.94°, L40	http://www.cccma.ec.gc.ca/models
CNRM-CM5	Centre national de Recherches Meteorologiques, Meteo-France	10	TL127, L31	TL127, L31	http://www.cnrm.meteo.fr/cmip5
CSIRO-MK3-6-0	Australian Commonwealth Scientific and Industrial Research Organization	10	T63, 1.875°×1.875° L18	1.875°×0.9375°, L31	*Rotstayn et al.* [2010]
GFDL-CM3	NOAA GFDL	5	Tripolar 360×200L50	C48L48	http://nomads.gfdl.noaa.gov
GISS-E2-R	NASA/GISS(Goddard Institute for Space Studies)	5	2°×2.5°, L40	1°×1.25°, L32	www.giss.nasa.gov/research/modeling
HadCM3	Met Office Hadley Centre, UK	10	N48, L19	1.25°×1.25°, L20	*Smith et al.* [2010]
IPSL-CM5A-LR	Institute Pierre Simon Laplace, France	4	LMDZ4_v5, 96×95×39	NEMOV2_3, 2°×2°, L31	http://icmc.ipsl.fr
MIROC-ESM	AORI, NIES, JAMSTEC, Japan	3	T42, L80	256×192, L44	*Watanabe et al.* [2011]
MPI-ESM1-M	Max Planck Institute for Meteorology	3	T63, L47	GR15, L40	*Raddatz et al.* [2007]
MRI-CGCM3	Meteorological Research Institute, Japan	5	TL159, L48	1°×0.5°, L51	*Yukimoto et al.* [2011]
NorESM1-M	Norwegian Climate Centre	3	F19, L26	gx1v6L53	*Bentsen et al.* [2012]

CHAPTER III

RESULTS

Ensemble Reanalysis

Ensemble Statistics

El Niño/Southern Oscillation (ENSO) has significant impact on world economics, society and ecology. As a consequence there have been many efforts to predict ENSO. Initial conditions and model error are two main factors that limit the skill of ENSO predictability. *Epstein* [1969] first proposed using an ensemble analysis for weather prediction in an effort to improve prediction skill affected by initial conditions. The first moment (ensemble mean) represents the best estimate of the true state, and the second moment (ensemble spread) represents the uncertainties in the initial conditions. When uncertainty is small a numerical forecast will be better than when the uncertainty is large, so that a narrow spread improves the forecast.

SODA 2.2.6 has eight ensemble members and the global ensemble spread of sea surface temperature (SST) is shown in Figure 1. The largest spread exists in western boundary current extension regions and in the Southern Ocean current system. Another region of large ensemble spread is the tropical Oceans, especially the eastern tropical Pacific Ocean as shown in Figure 2. In these areas, there are many small scale eddies caused by current shear, and because the variability of these eddies is uncorrelated between ensemble members there is large ensemble spread. The maximum ensemble spread in the eastern tropical Pacific Ocean occurs in the same area where El Niño and

La Niña anomalies are the largest (Figure 2). Thus it is possible that improved ENSO prediction could result from reducing the ensemble spread in the tropical Pacific Ocean.

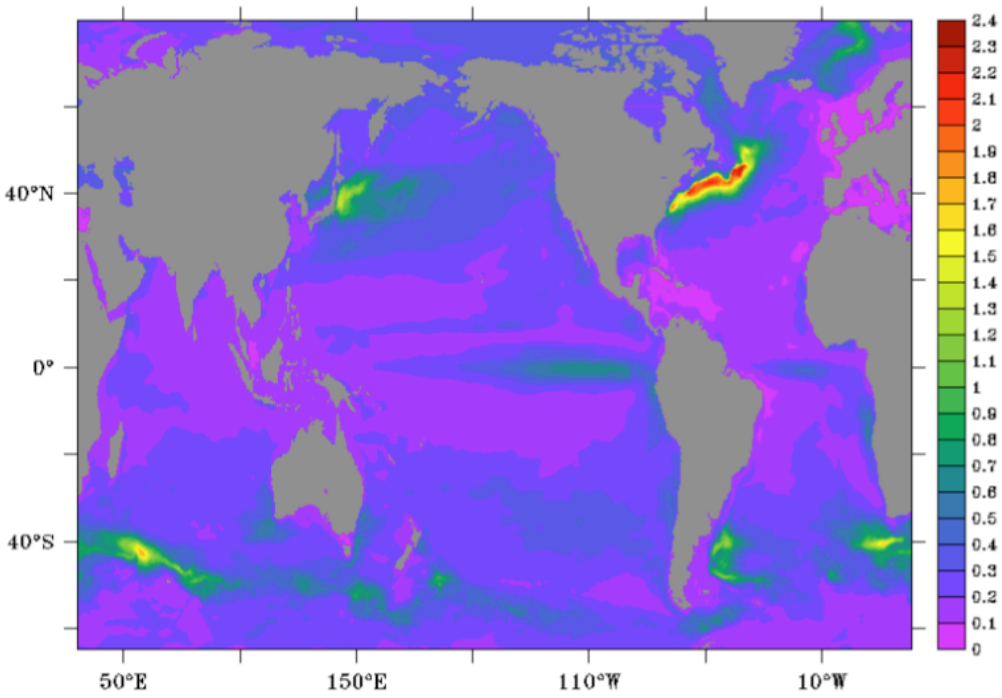

Figure 1. SST ensemble spread in °C in SODA 2.2.6.

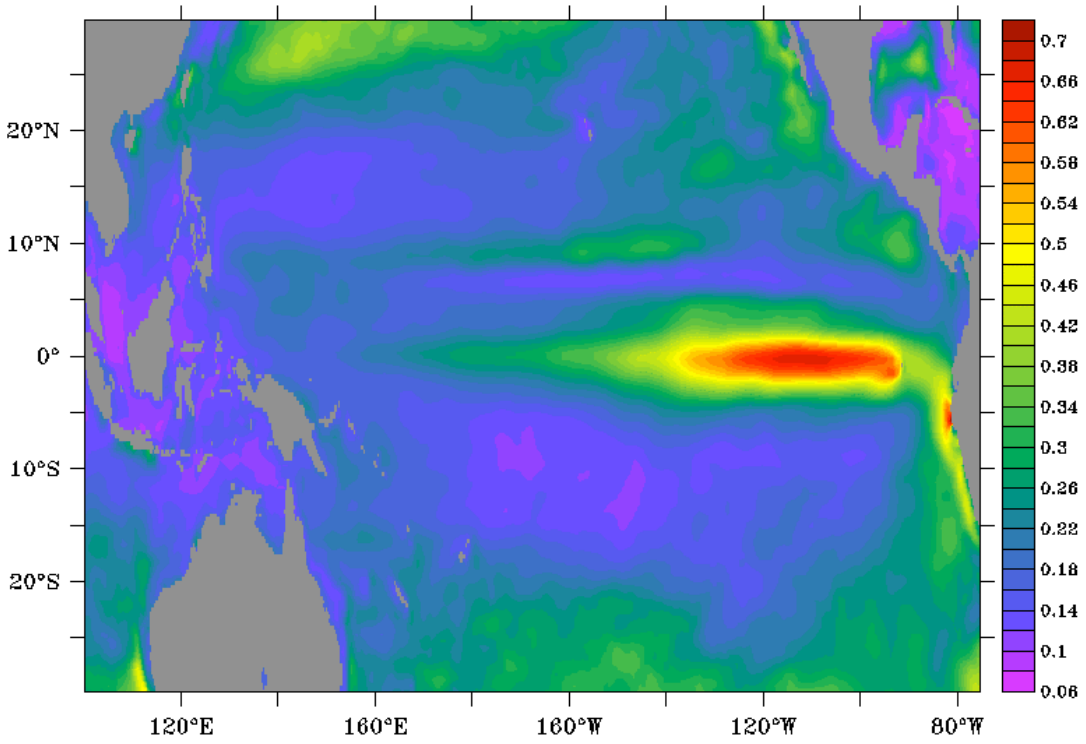

Figure 2. SST ensemble spread in °C of the tropical Pacific Ocean in SODA 2.2.6.

Global averaged SST spread (Figure 3) has a decreasing trend as a function of time. This is because as more and more observations become available in recent years the ensemble reanalyses become more similar to each other. In the tropical Pacific Ocean however, the ensemble spread of SST dose not decrease as much as the global average (Figure 4). This is because the ensemble spread in wind stress in 20CRv does not decrease as one might expect. This is likely due to the fact that 20CRv2 uses the same HadISST surface boundary conditions for all ensemble members. Further more, 20CRv2 does not change the uncertainty estimate for SST, so SST is considered to be as

well known in the early 1900s as today. In the tropics, SST variability is largely determined by the surface boundary conditions and so despite the increased number of ocean observations, the ensemble spread remains fairly constant.

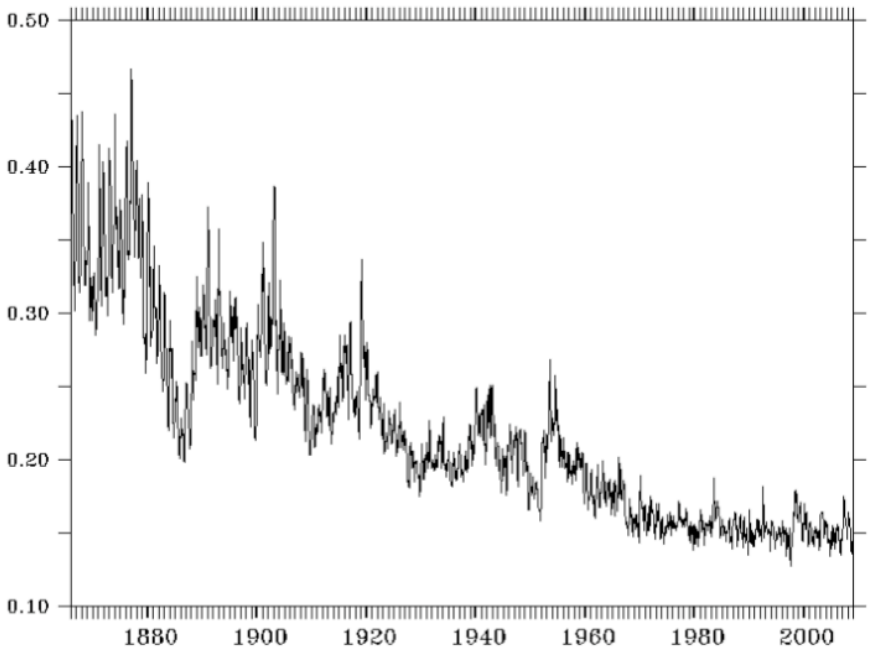

Figure 3. Global averaged SST spread in SODA 2.2.6.

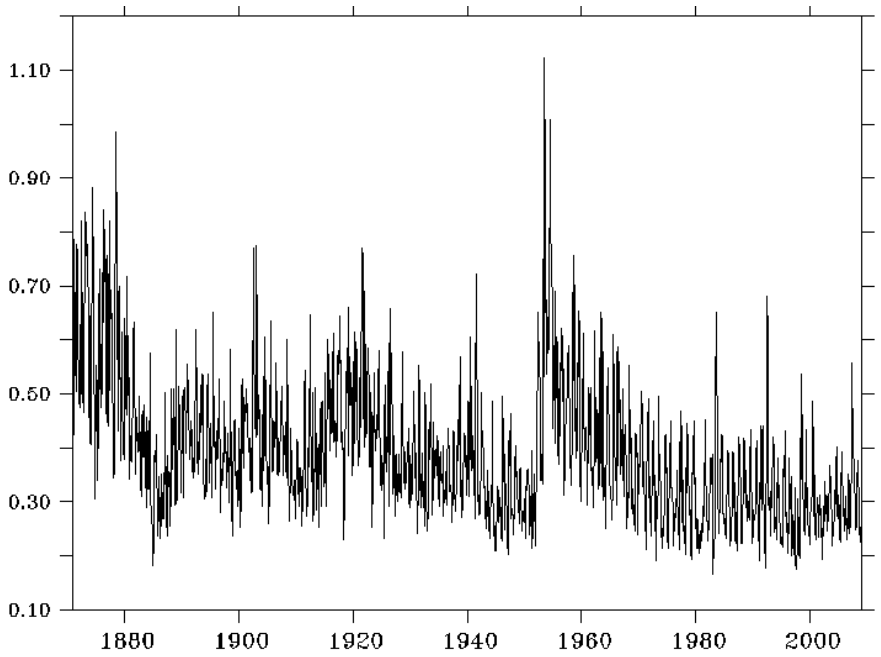

Figure 4. SST spread in SODA2.2.6 averaged from 140° W to 80° W and from 5° S to 5° N.

Seasonal Cycle

The accepted definition of El Niño is that El Niño exists when the 3-month running means of SST anomalies in the Niño 3.4 region [5° S-5° N, 120° W-170° W] exceeds 0.5°C for at least five consecutive months. To calculate SST anomalies, climatology has to be removed. For short records it is reasonable to use the entire record to calculate the climatology. However, for longer records, in which there may be prominent trends or low frequency variability, it is difficulty to determine which period should be used to calculate climatology. Since SODA 2.2.6 covers the period from 1871 to 2008, we use a climatology that evolves as a function of time. Niño 3.4 SST is shown in Figure 5. The actual SST is in blue, and the climatology based on an 11-year moving

window is shown in red. The first and last five years use a constant climatology based on the first and last 11 years of the record. The 11-year climatology has two components of change. On a centennial scale, the seasonal cycle is stronger from 1880 to 1940 than it is after 1940. There are also low frequency changes in temperature. For example, there is increasing temperature from the 1870s to about the 1900s, a slight decrease from 1900 to 1920, and a modest maximum centered near 1990. Because we do not want to have the changing seasonal cycle included as interannual variability we remove the 11-year seasonal cycle. *Giese and Ray* [2011] show that the effect of using this evolving climatology is relatively modest.

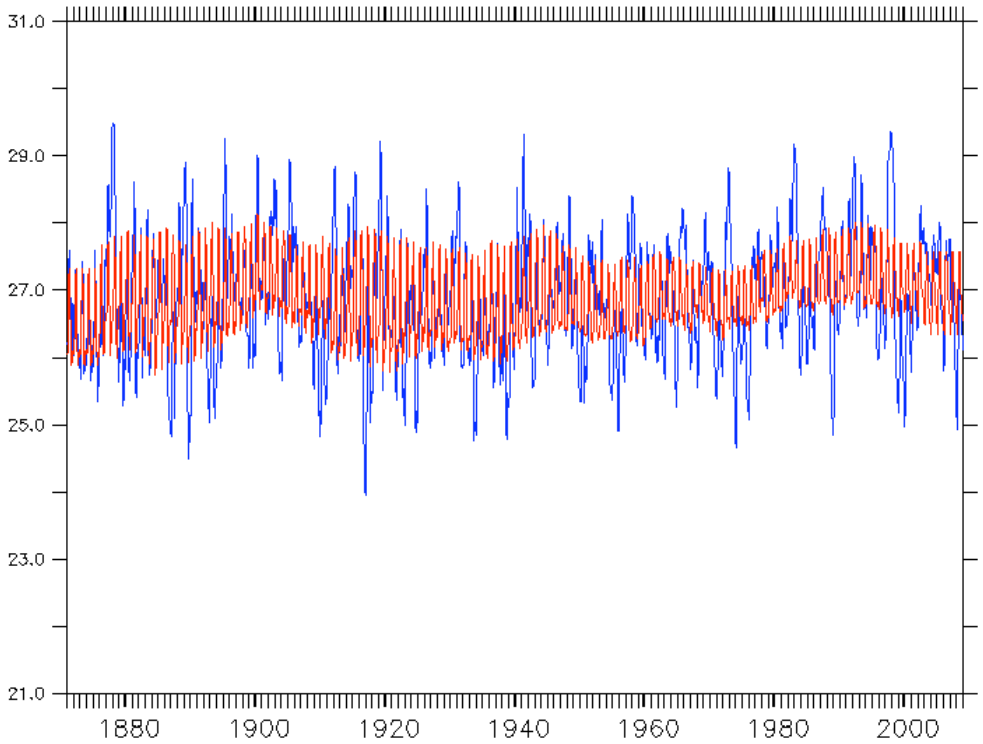

Figure 5. Niño 3.4 SST from SODA 2.2.6 (in blue) and the 11-year climatology (in red).

The first question is how large of an effect on ENSO comes from using ensemble forcing versus using ensemble mean forcing. To do this we compare SODA 2.2.6 and an assimilation forced by the ensemble mean of 20CRv2. ASSIM00 is a reanalysis identical to SODA 2.2.6, except using ensemble mean forcing. Niño 3.4 SST with a 23-months Parzen filter from ASSIM00 is shown with red line and the ensemble mean is shown as a blue line (Figure 6a). ASSIM00 has a slightly warmer Niño 3.4 SST than the SODA 2.2.6 ensemble mean. This difference is more pronounced in the early part of the record. Using ensemble mean forcing reduces the overall wind speed, because the weather noise is uncorrelated, especially in the early part of the record when there are few atmosphere observations. These lower wind speeds reduce latent heat release and so SST is warmer. Niño 3.4 SST anomalies are also calculated (Figure 6b) for SODA 2.2.6 and ASSIM00. A stronger zonal SST gradient results in slightly stronger SST anomalies. This effect is greater in the first half of the record.

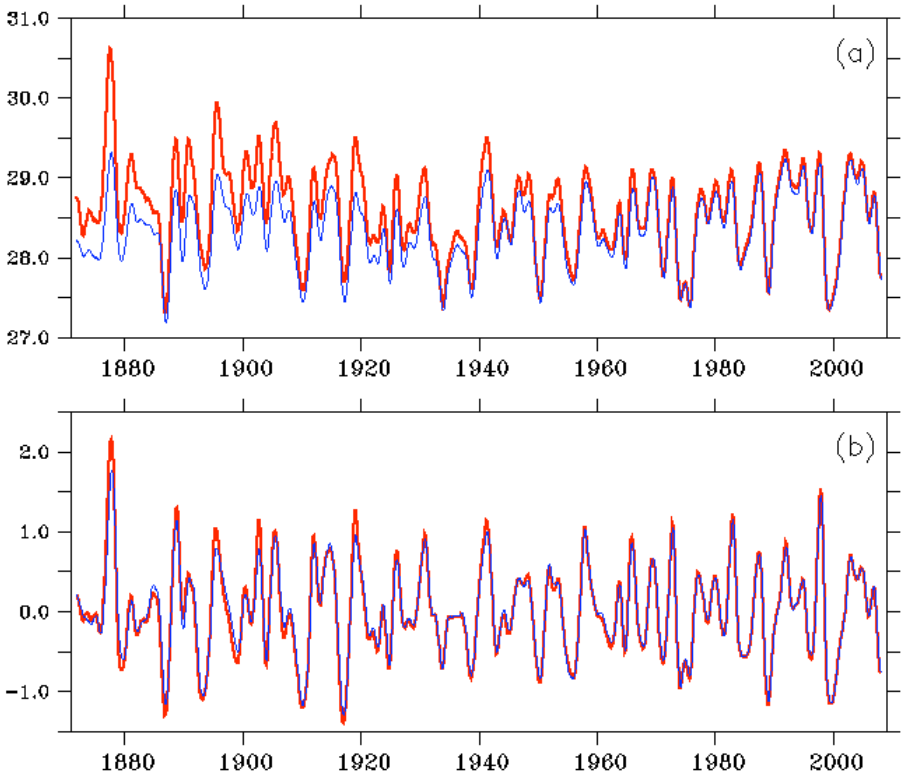

Figure 6. a) Niño 3.4 SST and b) Niño 3.4 SST anomaly from in ASSIM00 (in red) and the SODA 2.2.6 ensemble mean (in blue). The data has been smoothed with a 23-month Parzen filter.

El Niño/Southern Oscillation (ENSO)

Although Niño 3.4 SST anomaly is a well-accepted measure of El Niño, it is a fixed area measure and may not be a good measure if the spatial structure of El Niño varies. An alternative is the Center of Heat Index (CHI) [*Giese and Ray*, 2011]. CHI is the first moment of the SST anomaly, using only SST anomalies greater than 0.5°C within a strip that spans the tropical Pacific (120°E-70°W, 5°S-5°N). The area of warming must be greater than the Niño 3.4 region. CHI gives the temperature-weighted

center, in terms of longitude, of the warm anomaly. The CHI has three components, CHI longitude, CHI amplitude and CHI area. CHI longitude is calculated by

$$CHI\ \ longitude = \frac{\sum sst\_anom\ \times\ longitude}{\sum sst\_anom},$$

where sst_anom is the SST anomaly and must be greater than 0.5°C. CHI amplitude is calculated by

$$CHI\ \ amplitude = \frac{\sum sst\_anom\ \times\ area}{\sum area},$$

where the area is the area of temperature anomaly greater than 0.5°C. CHI area is the total area of SST anomaly greater than the area of the Niño 3.4 region and is calculated by

$$CHI\ \ area = \sum area.$$

CHI characteristics have been analyzed by *Giese and Ray* [2011] using an earlier version of SODA named SODA 2.2.4. In this study, the ensemble mean of SODA 2.2.6 is used to investigate ENSO variability and is compared with the results from SODA 2.2.4. The CHI amplitude from SODA 2.2.6 is plotted in Figure 7 from 1871 to 2008. The CHI amplitude (Figure 7a) shows prominent decadal variability of El Niño, with strong El Niño events from the beginning of the record to the 1920s, and from the 1970s to the end of the 20th century. From the 1920s to the 1960s there are few and relatively weak El Niños. Another interesting feature is that weak El Niños occur across the entire record but the occurrence of strong El Niño events changes. The fact that strong ENSO

occurs in the beginning of the record and at the end of the record shows decadal variability of El Niños. The central location of El Niño (CHI longitude) is shown in Figure 7b. The location of El Niños varies from east of the dateline to 100°W and has considerable variability but without clear decadal signal, which is different from CHI amplitude. The area covered by the warm anomaly is shown in Figure 7c, and it shows that El Niño events have a wide range of areas with prominent decadal variability in which from the 1870s to the 1920s the CHI area has a decreasing trend while there is an increasing trend from the 1920s to the 1960s. However, from the 1960s to the end of the record the area covered by warm events decreases again.

Compared with SODA 2.2.4, CHI longitude in SODA 2.2.6 has similar features while CHI amplitude and CHI area have different variability. In SODA 2.2.4, there are more strong El Niños in the beginning of the record, and CHI area has a decreasing trend that does not occur in SODA 2.2.6. In SODA 2.2.4 the surface forcing comes from the ensemble mean of 20CRv2, and so high frequency wind stress tends to be cancelled out. Thus wind speed is smaller in the western Pacific and SST is warmer. Warmer SST in the western tropical Pacific results in a stronger zonal SST gradient and strengthens the amplitude of El Niño. Because there were few observations in the beginning of the record the difference between these two reanalysis is more obvious. This may also explain the difference in CHI area between the two reanalyses. With a stronger SST gradient in SODA 2.2.4 it is possible that there is a greater area that meets the 0.5°C criteria threshold in the beginning of the record.

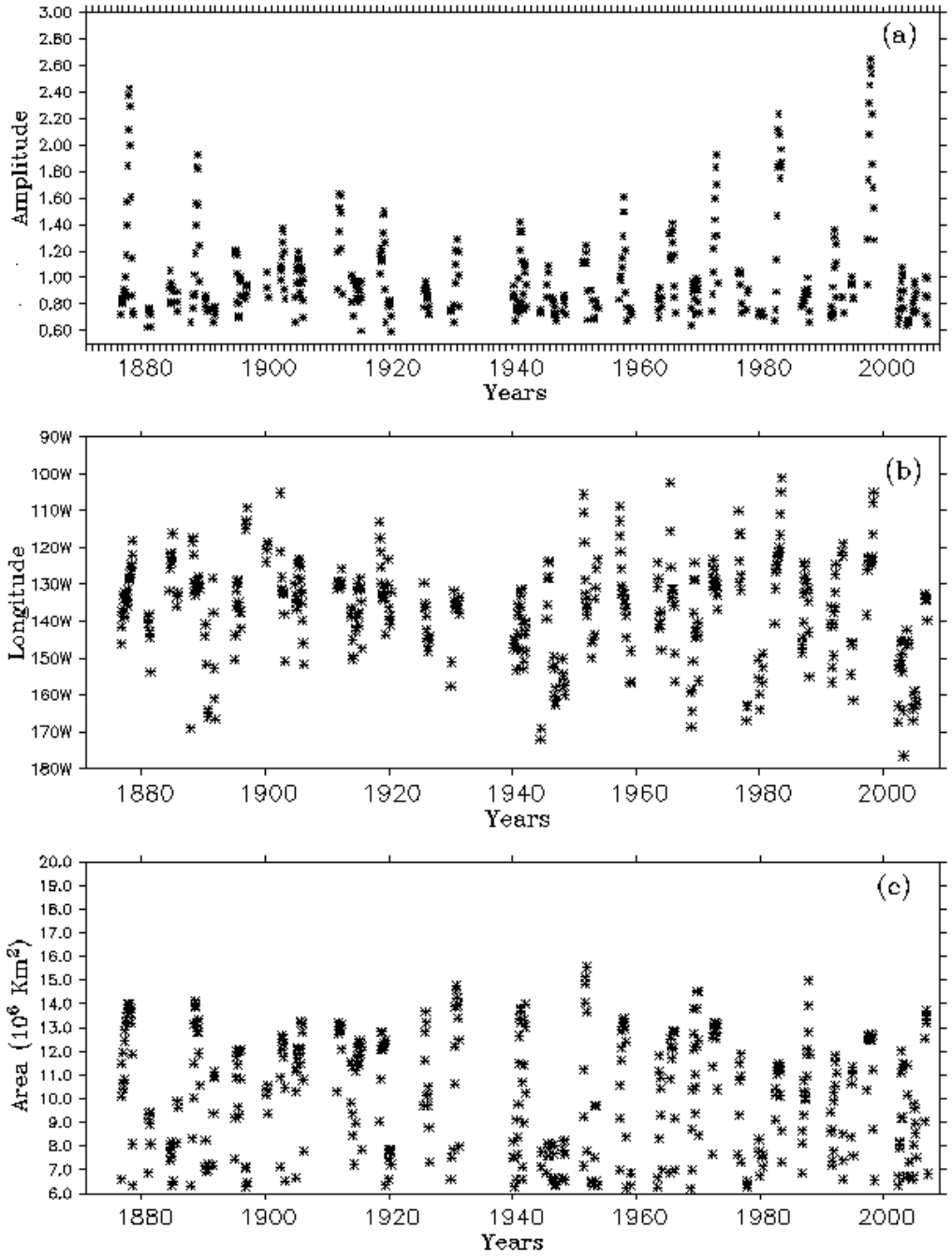

Figure 7. Warm event a) CHI amplitude in °C, b) CHI longitude in ° and c) CHI area in km^2.

The CHI characteristics of La Niña are calculated by replacing the 0.5°C criteria with -0.5°C (Figure 8). Compared with El Niño events, CHI amplitude for La Niña is small and has less variability. All three characteristics of La Niña events, CHI amplitude, CHI longitude and CHI area tend to be more uniform without distinguishable variation across the entire record. The different characteristics of El Niño and La Niña events agree with the asymmetry between El Niño and La Niña, which has been noted by several studies [*An and Jin*, 2004; *Hoerling et al.*, 1997; *Jin et al.*, 2003]. The mechanism responsible for the asymmetry between El Niño and La Niña events is discussed in the next section.

CHI gives us three characteristics of El Niño and La Niña events and the relationship between these three components is also analyzed (Figure 9 for El Niño events, Figure 10 for La Niña events). For El Niño events, weak El Niños occur from east of the Dateline to 100°W, but strong El Niños only occur in the eastern Pacific between 140°W and 120°W. The relationship between CHI area and CHI amplitude shows that weak El Niños have a wide range of areas but strong El Niños tend to cover larger areas than weak El Niños. However, for La Niña events, the plot of CHI amplitude as a function of CHI longitude shows that the amplitude of La Niña events is more uniform. As for El Niños, strong La Niñas tend to cover larger areas.

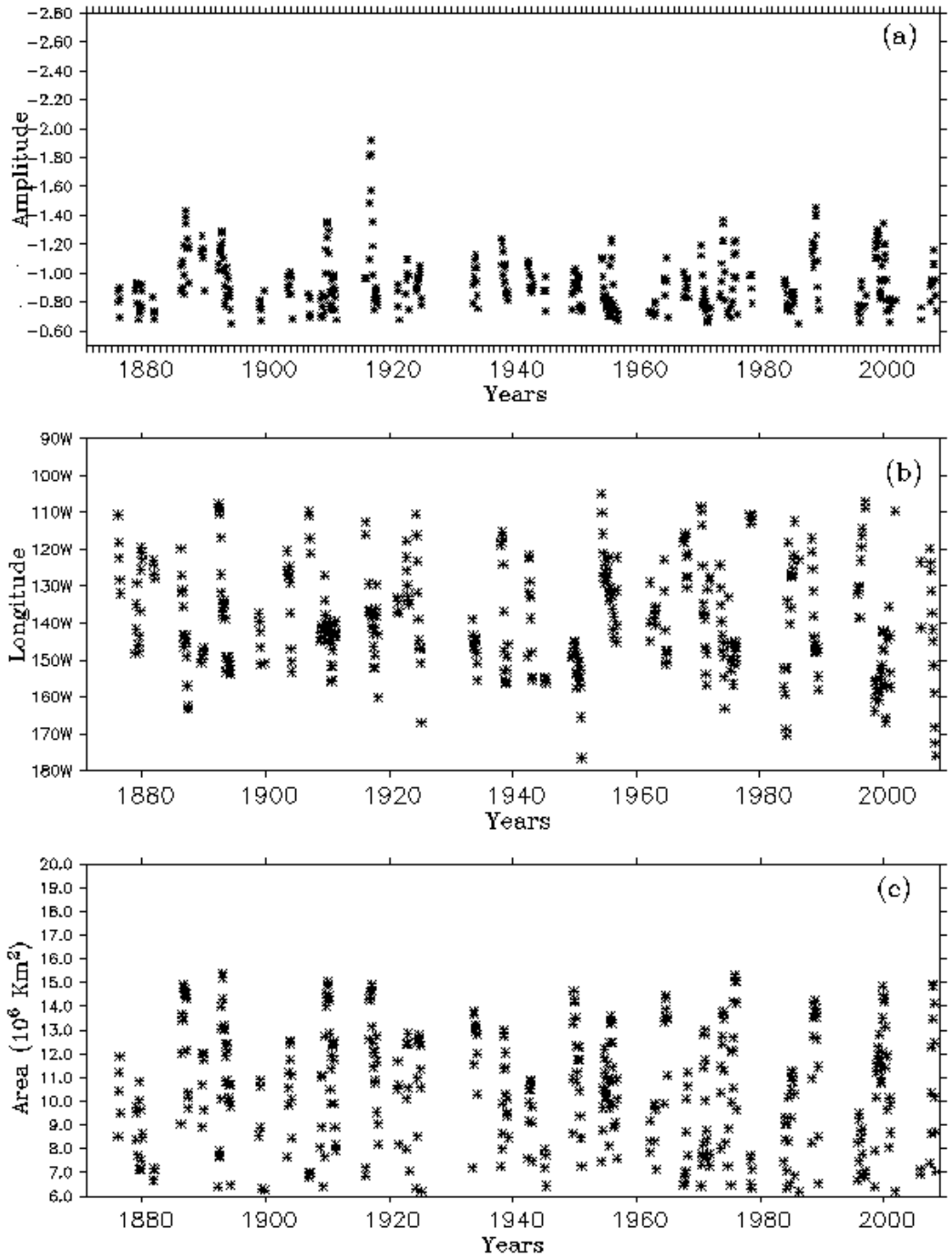

Figure 8. Cold event a) CHI amplitude in °C, b) CHI longitude in ° and c) CHI area in km^2.

CHI longitude and amplitude are used to compare ASSIM00 and SODA 2.2.6 (Figure 11). In this figure, values from before 1950 are shown in red and values from after 1950 shown in blue. After the 1950s ASSIM00 and SODA 2.2.6 have similar CHI longitude and amplitude, but before the 1950s there are significant differences. Before the 1950s, El Niño events in ASSIM00 are stronger, and the location of El Niños is further west than in SODA 2.2.6. ASSIM00 is forced with the ensemble mean of atmospheric reanalysis and so high frequency of wind stress has been averaged out, resulting in weak westerly wind speed. The weakening westerly wind anomaly results in a warmer west Pacific and so the tropical Pacific SST gradient is stronger. The warming background in ASSIM00 causes the amplitude of El Niño events to be stronger and further west compared to SODA 2.2.6.

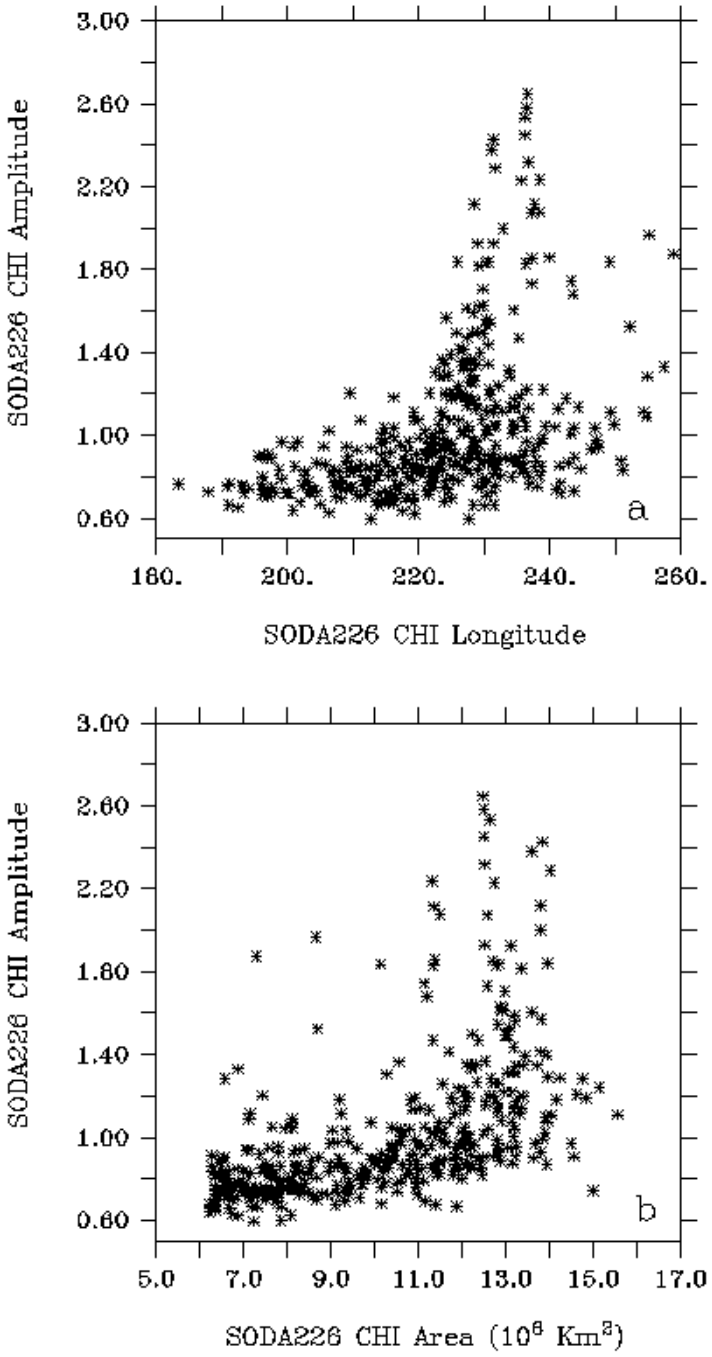

Figure 9. Warm event a) CHI amplitude plotted as a function of CHI longitude and b) CHI amplitude plotted as a function of CHI area.

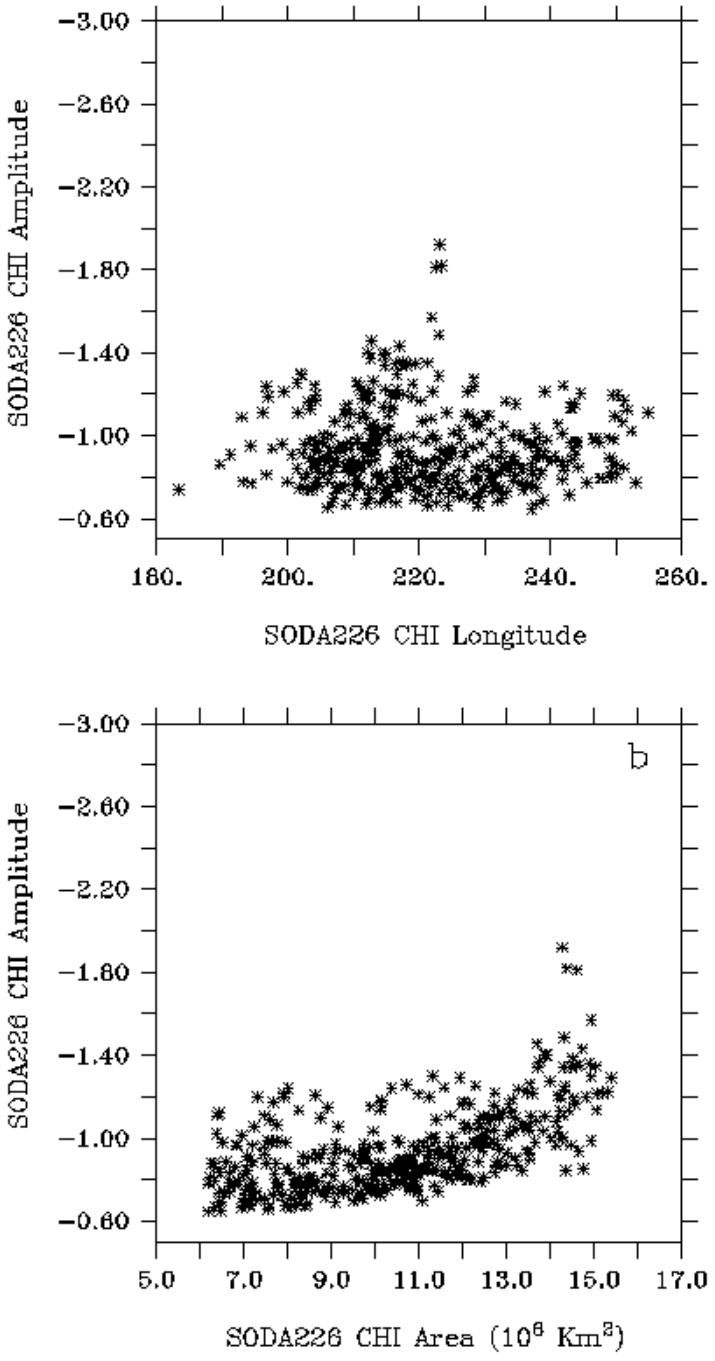

Figure 10. Cold event a) CHI amplitude plotted as a function of CHI longitude and b) CHI amplitude plotted as a function of CHI area.

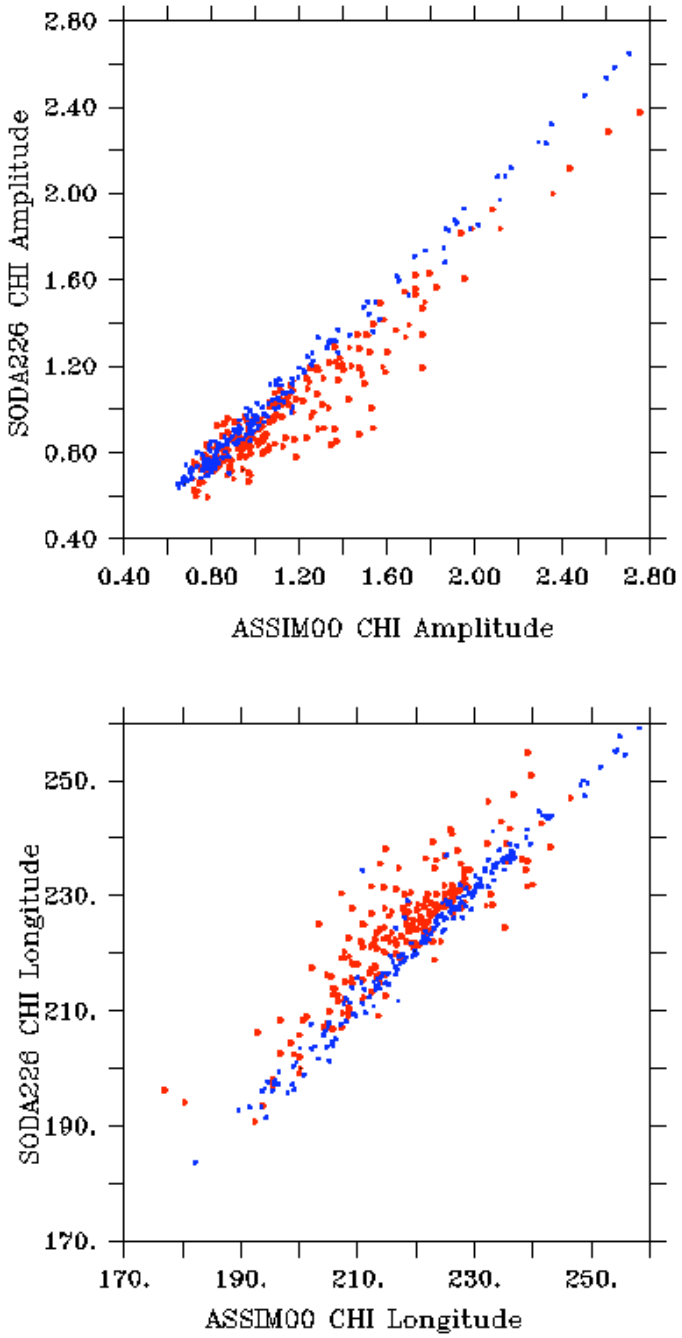

Figure 11. CHI amplitude (upper panel) and longitude (lower panel) in ASSIM00 and SODA2.2.6 before the 1950s (in red) and after the 1950s (blue).

The strength of ENSO has been analyzed in the eight ensemble members of SODA 2.2.6, and interestingly the results show that in different ensemble members ENSO has different strengths (Figure 12 for El Niño and Figure 13 for La Niña). For example, the 1918-1919 El Niño is strongest in the fifth ensemble member (ENS05) with CHI amplitude of 1.8°C and weakest in the seventh ensemble member (ENS07) with CHI amplitude of 1.4°C.

In order to investigate the reason for the difference between ensemble members, the evolution of 1918/1919 El Niño event is shown in Figure 14 for ENS05 and ENS07. We use 5-day data, which gives greater detail of the evolution of the El Niño. The onset of the 1918/1919 El Niño event using Sea Surface Height (SSH) anomaly is shown with shading and the zonal wind stress anomaly is shown by contours. One significant difference of the 1918/1919 El Niño event between these two ensemble members is the onset time of the event. In ENS05, Westerly Wind Bursts (WWBs) occur in the beginning of December 1918 followed by a strong SSH anomaly in the middle of December 1918. In ENS07, a WWB does not occur until the beginning of January 1919 followed by a SSH anomaly in the middle of January 1919. The amplitude of WWBs in ENS05 is also much stronger than that in ENS07 which results in a stronger SSH anomaly in ENS05 than that in ENS07. The earlier onset of WWB and the stronger amplitude of WWB in ENS05 cause a stronger El Niño event. The different strength of El Niño in different ensemble members suggests the importance of high frequency wind stress to the strength of ENSO.

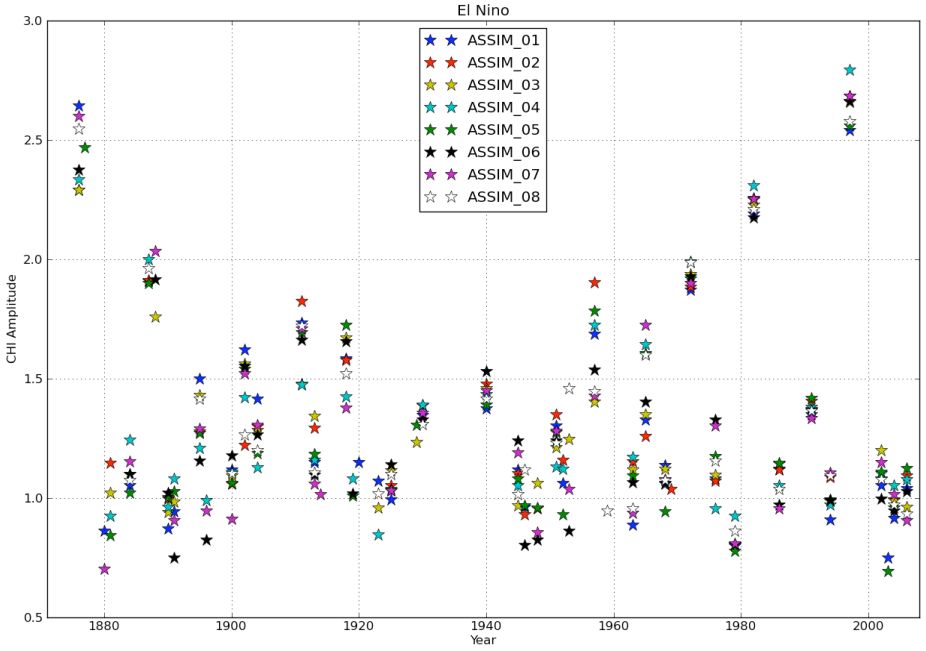

Figure 12. CHI amplitude of warm events in each ensemble member.

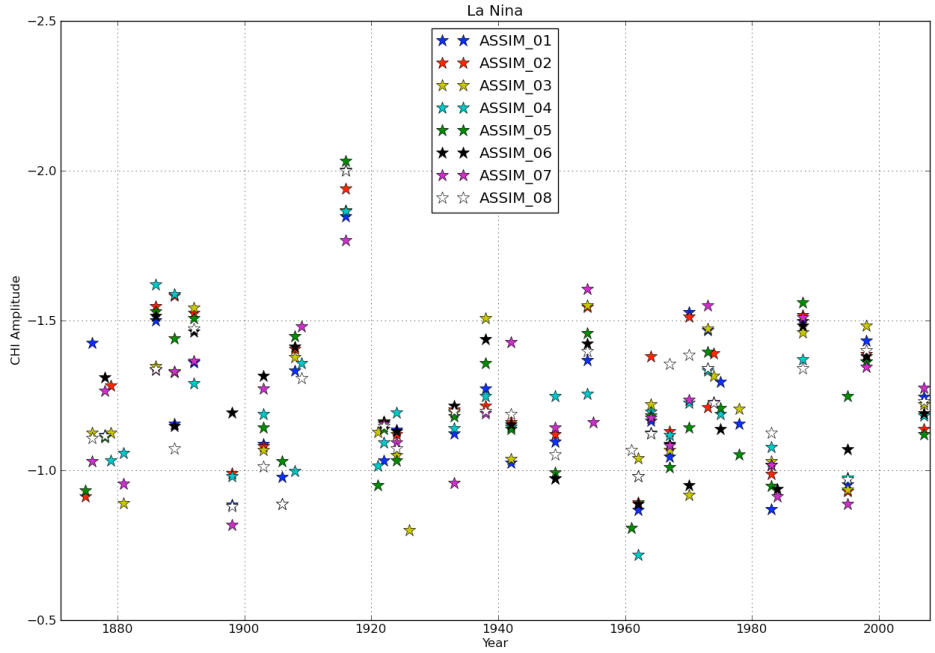

Figure 13. CHI amplitude of cold events in each ensemble member.

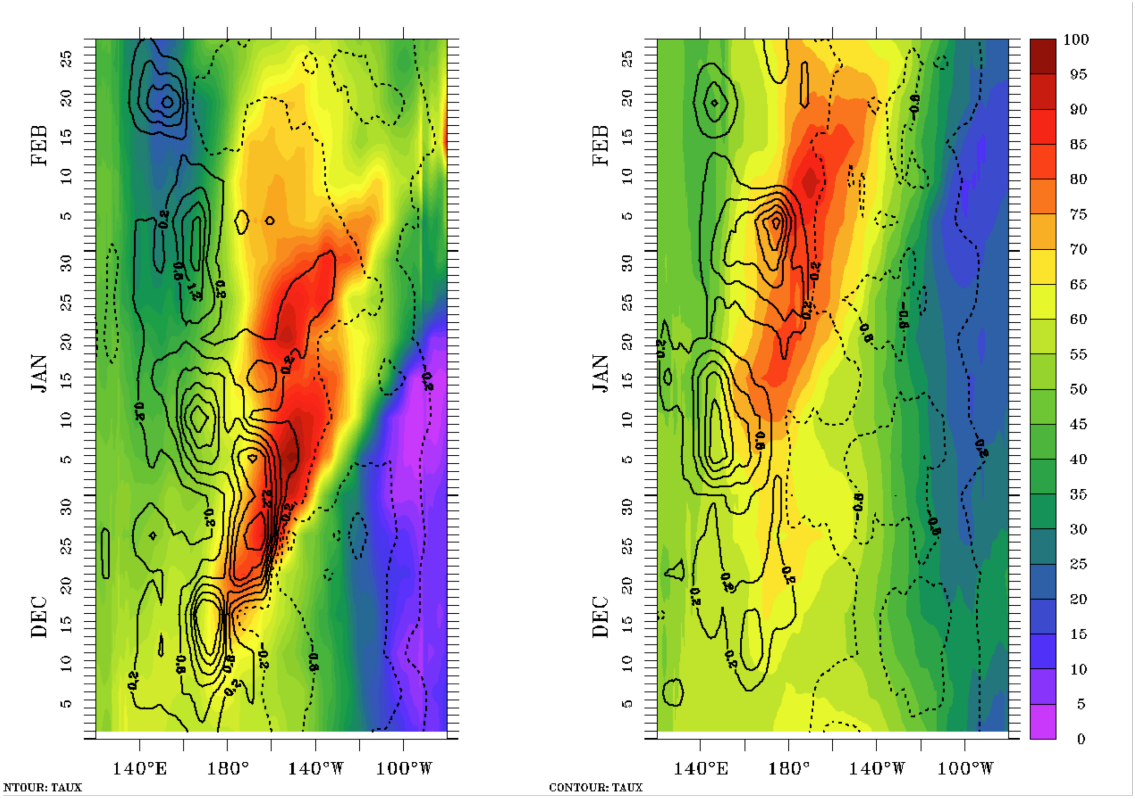

Figure 14. The 1918-1919 El Niño in ensemble 5 and ensemble 7. Sea surface height anomaly is shown by shading and the zonal wind stress anomaly is shown by contours.

Studies of predictability of ENSO show that atmospheric disturbances have limited the predictability of specific El Niño events, especially the strength of El Niño [*Fedorov et al.*, 2003]. *Fedorov* [2002] proposed that the timing of the WWBs has an impact on the strength of ENSO, such that WWBs can increase the amplitude of El Niño if the occurrence of WWBs is 6 or 10 months before the peak of warming. Likewise, a WWB decreases the strength of the following El Niño if the occurrence of WWBs is during La Niña event. In this study, the timing of WWBs is different in different ensemble members, resulting in different strengths of El Niño. This result is consistent

with the argument of [*Fedorov*, 2002]. The amplitude of WWBs in different ensemble members also accounts for the different strengths of the same El Niño event. For example, in SODA 2.2.6, the amplitude of WWBs in ENS5 is larger than in ENS7 so ENSO in ENS5 is bigger than in ENS7. Due to the importance of atmospheric noise and the interplay with the phase of Southern Oscillation, ensemble experiments and probabilistic forecasts are essential for successful ENSO forecasts [*Fedorov et al.*, 2003].

ENSO is characterized by warm events, called El Niño, and cold events, called La Niña. However, both observations and model simulations show a profound asymmetry between El Niño and La Niña, with the amplitude of El Niño being larger than the amplitude of La Niña [*An and Jin*, 2004; *Burgers and Stephenson*, 1999; *Dong*, 2005; *Jin et al.*, 2003; *Kang and Kug*, 2002; *McPhaden and Zhang*, 2009]. The mechanisms responsible for the asymmetry of El Niño and La Niña have been addressed by several studies [*Jin et al.*, 2003; *Kang and Kug*, 2002; *McPhaden and Zhang*, 2009]. *Kang and Kug* [2002] argue that an asymmetry of wind stress in the western and central tropical Pacific results in stronger SST anomalies during El Niño. *Frauen and Dommenget* [2010] proposed a nonlinear relationship between zonal wind stress and SST that is responsible for the asymmetry of El Niño and La Niña amplitude. *Jin et al.* [2003] suggest that nonlinear dynamical heating in ocean processes is significant for the large amplitude of El Niño relative to La Niña. *McPhaden and Zhang* [2009] argue that the different zonal propagation of El Niño and La Niña contributes to strong El Niño. The duration of El Niño and La Niña is also asymmetric as El Niño decays rapidly after

the mature phase in December but La Niña often lasts into the following year [*Kessler*, 2002; *Okumura and Deser*, 2010; *Okumura et al.*, 2011]. Nonlinear processes associated with atmospheric deep convection in response to equatorial SST anomalies may also contribute to short El Niño compared to La Niña [*Okumura and Deser*, 2010]. Since there is doubt about the mechanisms responsible for the asymmetry of El Niño and La Niña, further research is called for.

The mechanism responsible for the asymmetry of El Niño and La Niña is analyzed using the 5-day data of SODA 2.2.6. In this study, we focus on the role of high frequency variability from atmospheric forcing. The frequency of maximum westerly wind anomalies and easterly wind anomalies has been calculated and shown in Figure 15. The frequency of the maximum for westerly wind anomalies is shown as red bars and the frequency of maximum easterly wind anomalies is shown as blue bars. Figure 15 shows values smaller than 0.7 Nm^{-1} and Figure 16 shows values of the anomaly larger than 0.7Nm^{-1}. For weak wind stress anomalies the frequency of westerly and easterly winds is very similar, with a peak at 0.2-0.3Nm^{-1} of about 1000 events (Figure 15). However, there are many more strong westerly wind anomalies than strong easterly wind anomalies (Figure 16). Since a westerly wind anomaly may be important to the strength of El Niño events, and statistically there are more strong westerly wind anomalies than strong easterly anomalies, thus may account for the observed asymmetry of El Niño and La Niña.

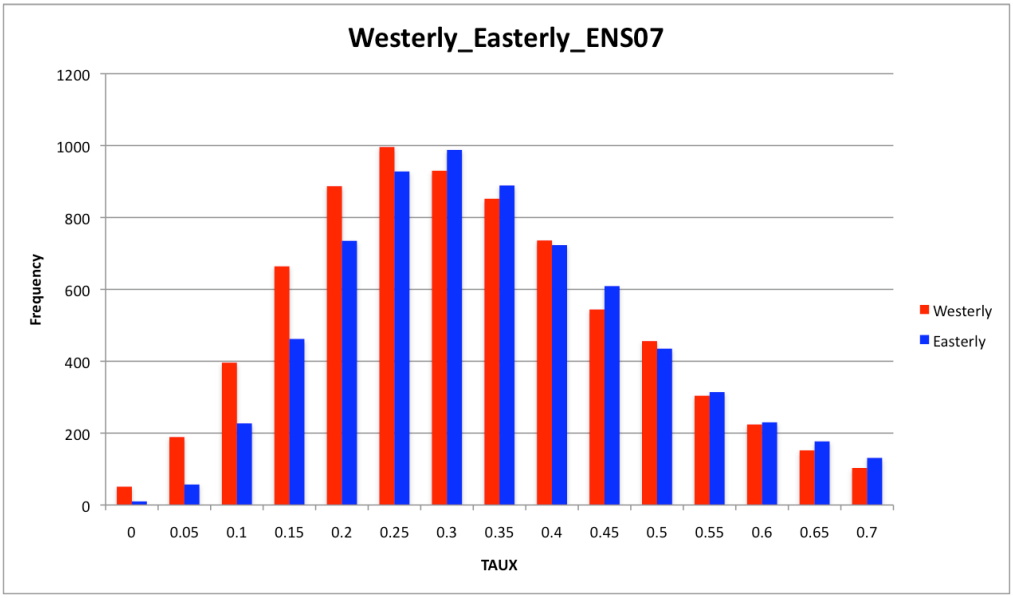

Figure 15. Frequency of the maximum of westerly wind anomalies (red) and easterly wind anomalies (blue) with values smaller than 0.7.

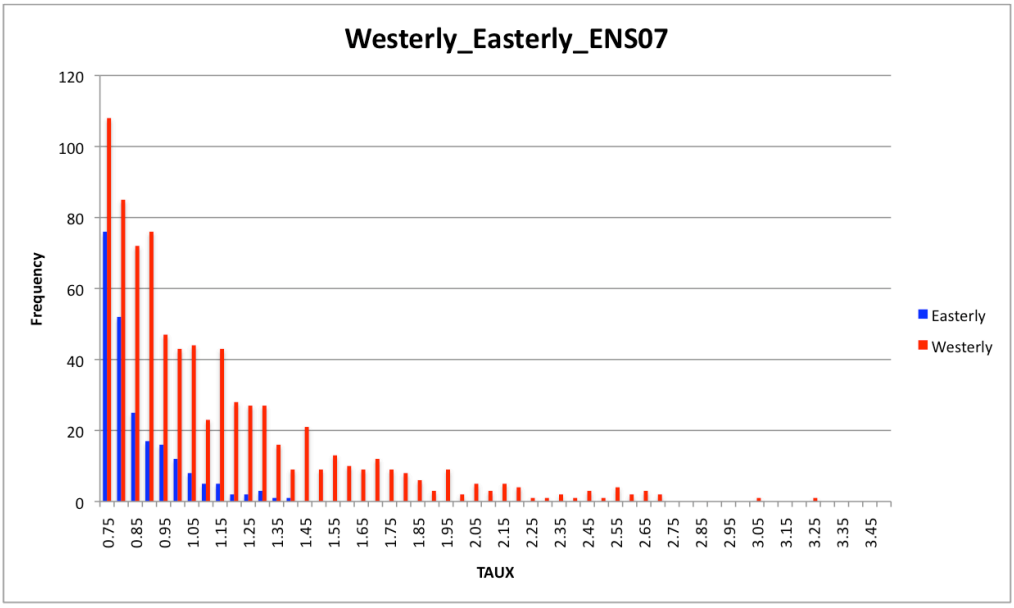

Figure 16. Frequency of the maximum of westerly wind anomalies (red) and easterly wind anomalies (blue) with values larger than 0.7.

The frequency of westerly wind anomalies is also investigated separately for El Niño events, La Niña events and for neutral conditions (Figure 17 and Figure 18). For El Niño events the frequency of the maximum westerly wind anomalies is shown with red bars, for La Niña events the frequency is shown with blue bars and for neutral conditions the frequency is shown with green bars. The frequency of the maximum weak westerly wind stress anomalies during different conditions is shown in Figure 17. The figure shows that for weak wind stress anomalies the frequency of maximum westerly wind anomalies is similar for all conditions and the maximum frequency of westerly wind anomalies have strengths of around 0.2-0.4Nm^{-1}. The frequency of strong westerly wind anomalies is plotted in Figure 18 and shows that there are more strong westerly wind bursts during El Niño events than during La Niña events and neutral conditions. This may also contribute to the asymmetry of El Niño and La Niña.

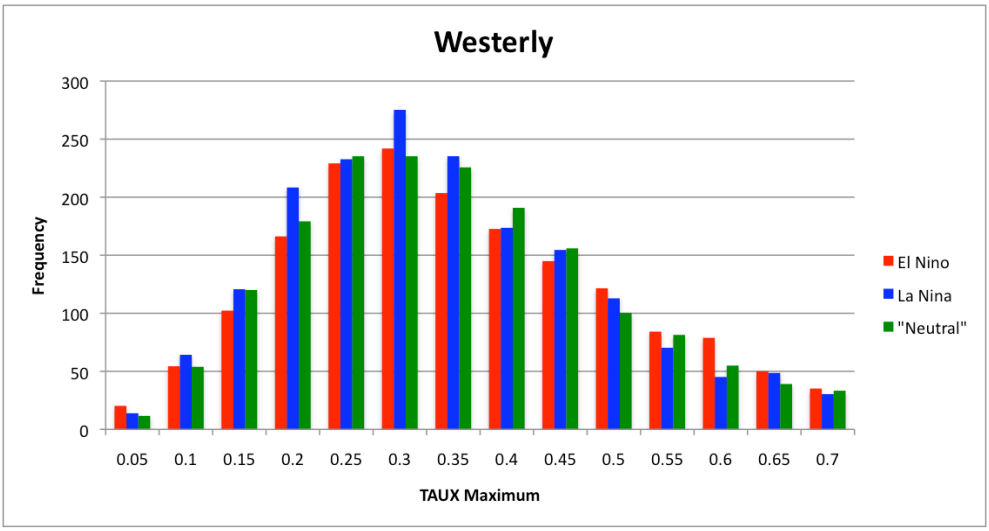

Figure 17. Frequency of the maximum of westerly wind anomalies during El Niño events (red), La Niña events (blue) and neutral condition (green) with values smaller than 0.7.

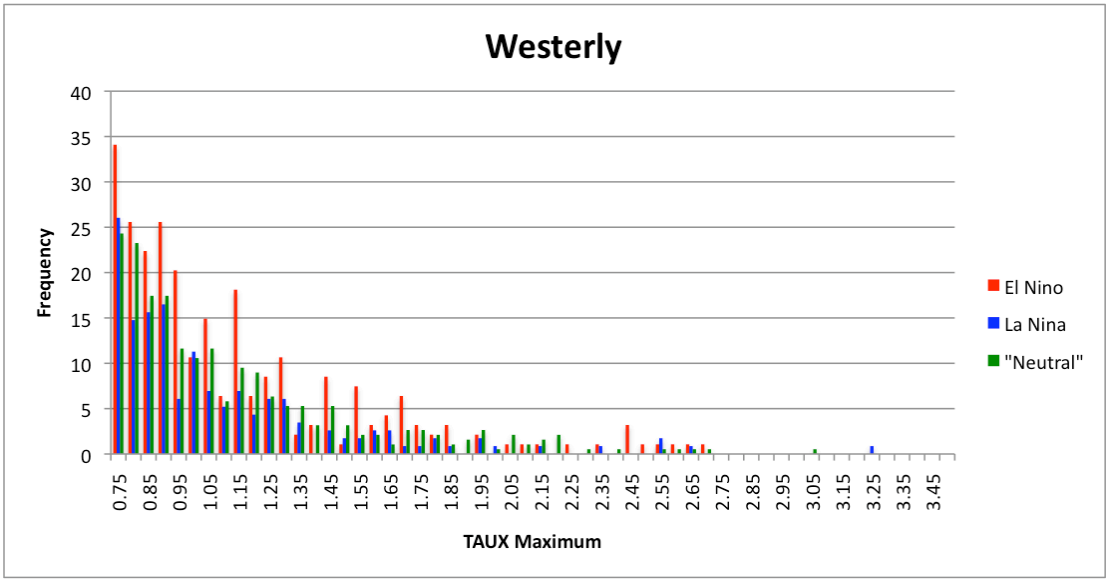

Figure 18. Frequency of the maximum of westerly wind anomalies during El Niño events (red), La Niña events (blue) and neutral condition (green) with values larger than 0.7.

The frequency of easterly wind anomalies during El Niño events, La Niña event and neutral conditions is shown in Figure 19. Interestingly, the frequency of the easterly wind anomalies is similar for all conditions and peaks at around negative 0.2-0.4Nm^{-1}. For weak easterly wind anomalies, the frequency of the maximum easterly wind anomalies is similar, which agrees with the distribution of westerly wind anomalies. But for strong easterly wind anomalies, the frequency of the maximum easterly wind anomalies is similar for all conditions, which is different from the distribution of westerly wind anomalies. There are more strong westerly wind anomalies than strong easterly wind anomalies and more strong westerly wind events occur during El Niño events that may be responsible for the asymmetry of El Niño and La Niña.

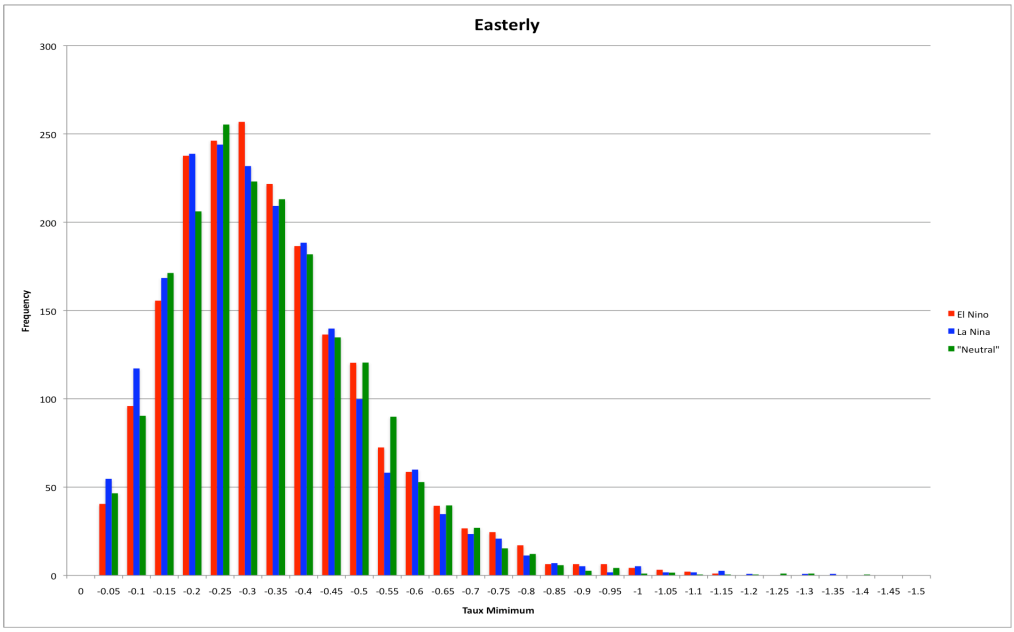

Figure 19. Frequency of the maximum easterly wind anomalies during El Niño events (red), La Niña events (blue) and neutral conditions (green).

Sub-tropical Cells (STCs)

The maintenance of the background state has significant impact on ENSO variability [*Fedorov and Philander*, 2000; *Fedorov and Philander* 2001; *Neelin et al.*, 1994]. The Sub-tropical Cell (STC) consists of subduction of sub-tropical water into the equatorial thermocline, equatorial upwelling, and surface Ekman return flow from the tropics to the subtropics [*McCreary and Lu*, 1994] and is an important factor in regulating tropical Pacific SST variability and the background state of the tropical Pacific and has significant impact on ENSO variability. In order to explore the mechanisms responsible for ENSO variability in SODA 2.2.6, the role of ocean dynamics is investigated with an emphasis on long-term changes of the STC. The

meridional stream function of the STC in SODA 2.2.6 (Figure 20) shows that seawater subducts into the deep ocean at around 30°S and 30°N and flows back to the equator through the pycnocline in both the Northern and Southern Hemispheres. The transport of the STC in the Southern Hemisphere is about 40Sv, a little stronger than the STC transport in the Northern Hemisphere of about 30Sv.

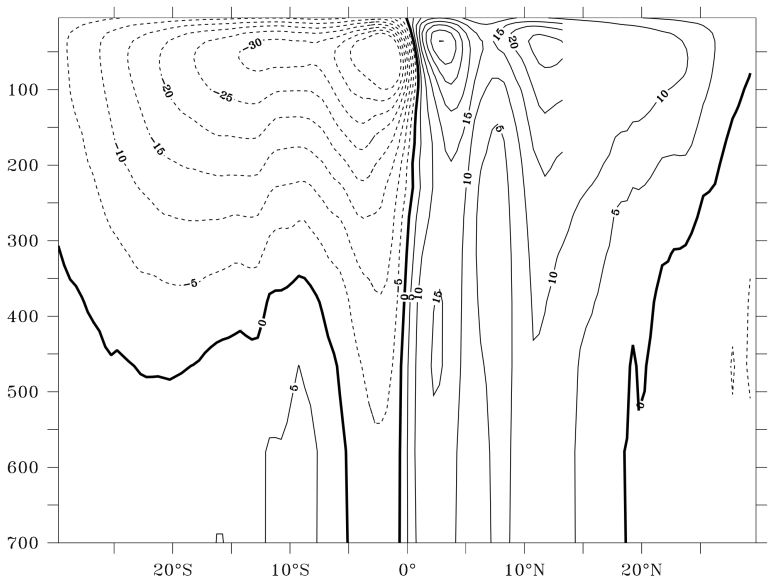

Figure 20. Long-term mean of the STC meridional stream function in Sv from SODA 2.2.6.

We first examine the linear trends of tropical Pacific SST in SODA 2.2.6 calculated with a least squares method using monthly averaged data from 1900 to 2008. There is a cooling trend over the central tropical Pacific of about -0.2°C century^{-1} and warming over the western tropical Pacific that is about 1.2°C century^{-1} (Figure 21a). Similar to SST the subsurface also displays a cooling trend, of about -1.4°C century^{-1} in

the central and eastern tropical Pacific at a depth of 100m-150m, and a warming trend in the western tropical Pacific of 2.0°C century^{-1} at 150m (Figure 21b). The consistency of ocean temperature trends between the surface and subsurface suggests the role of ocean dynamics in setting the pattern.

The linear trend of wind stress from 1900 to 2008 shows anomalously divergent winds over the cooling region with anomalous easterlies in the west and anomalous westerlies in the east (Figure 21c). The easterly wind anomalies cause the equatorial thermocline to shoal in the central equatorial Pacific and to deepen the equatorial thermocline in the west. Vertical movement of the thermocline accounts for both the SST and subsurface temperature changes. Off the equator, both the northeast and southeast trades intensify west of 120°W. Such changes in the wind stress presumably can accelerate the STC, which transports cold sub-tropical thermocline water to the equatorial theremocline.

We also calculated SST trends and subsurface temperature trends in ASSIM00 (Figure 22), which shows that there is a stronger cooling trend in the central tropical Pacific. The warming trend in the western tropical Pacific is a little weaker and the subsurface is cooler than that in SODA 2.2.6. Since ASSIM00 is forced with the ensemble mean of 20CRv2, the high frequency wind speed at the equator is weaker resulting in warmer SST in the central tropical Pacific especially in the beginning of the record which contains few observations. The warmer SST in the beginning of the record causes a stronger SST trend in the central tropical Pacific in ASSIM00 than SODA 2.2.6.

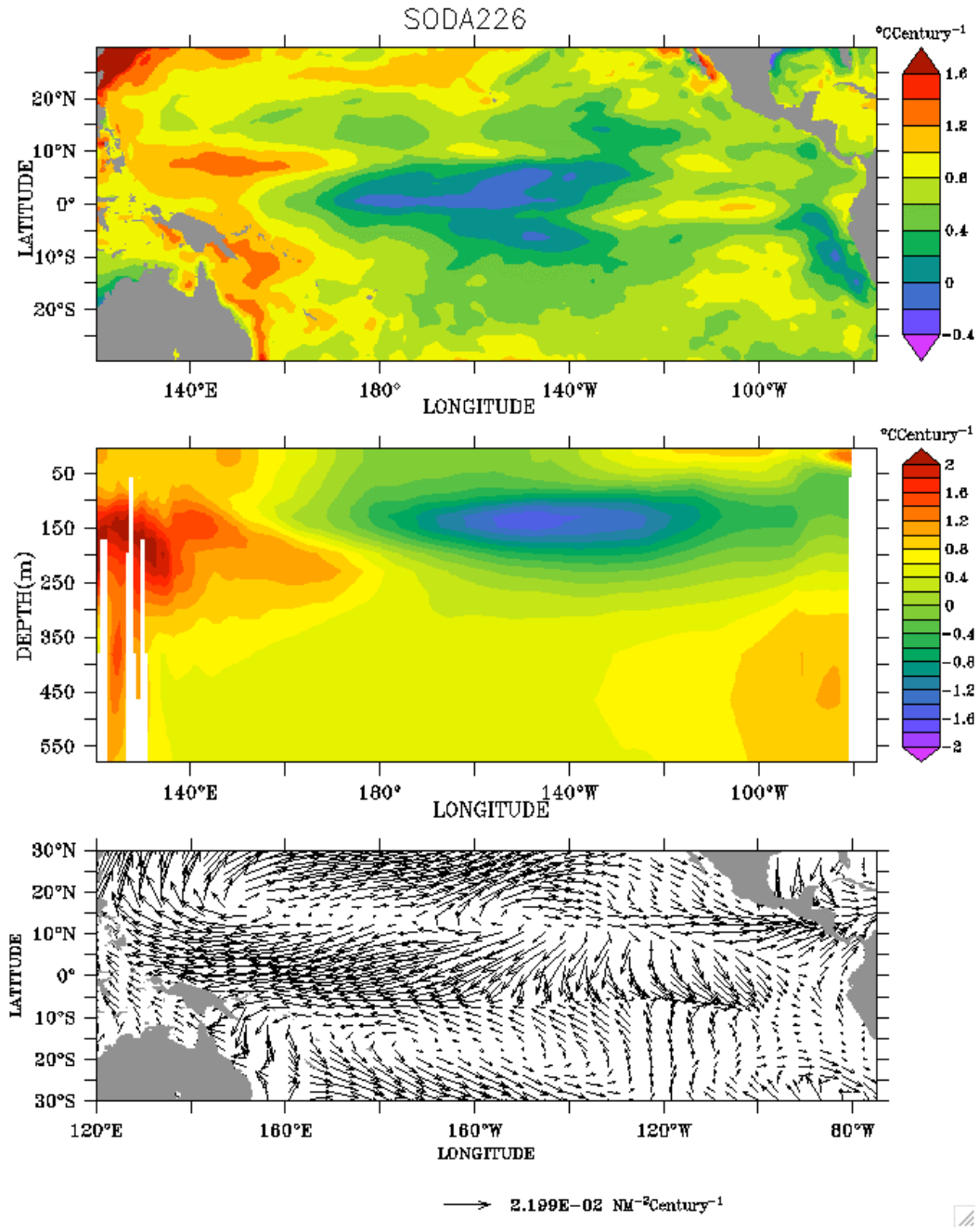

Figure 21. Linear trends in SODA 2.2.6 from 1900 to 2008 of (a) sea surface temperature, (b) temperature as a function of depth on the equator and (c) vectors of zonal and meridional wind stress.

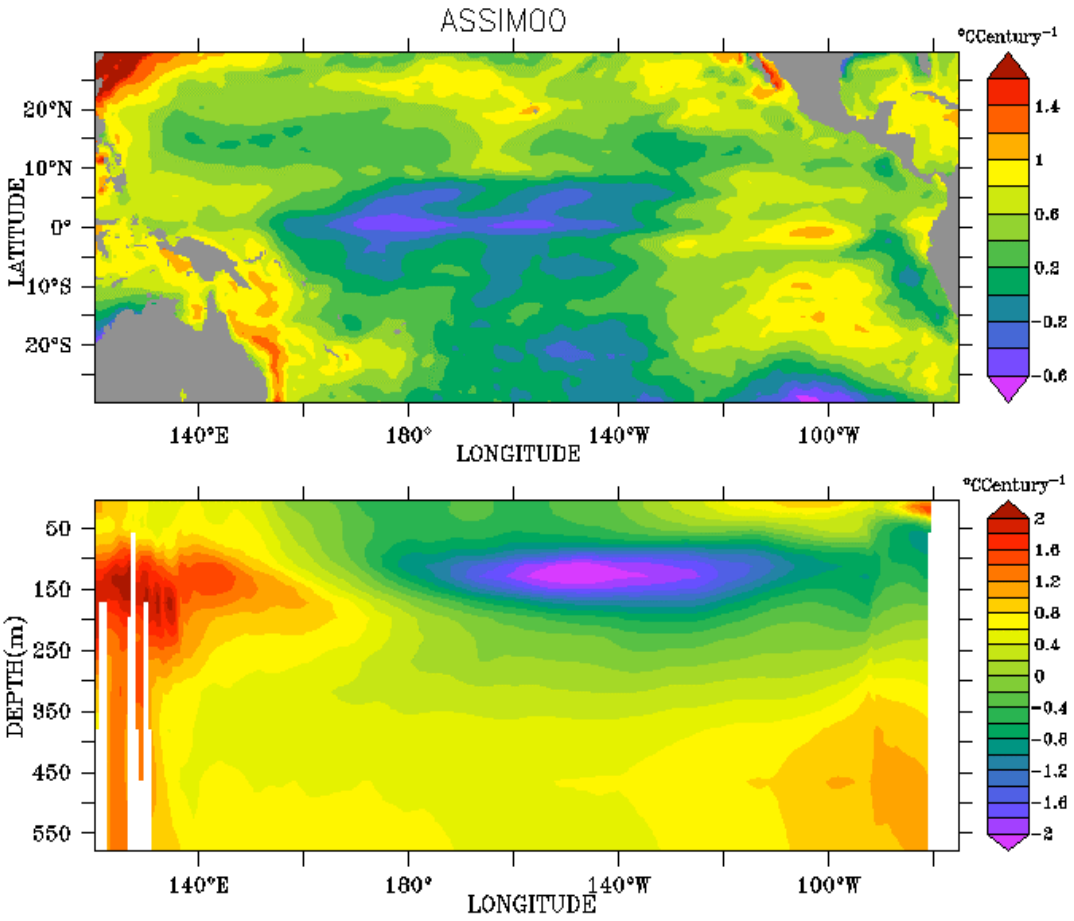

Figure 22. Linear trends in ASSIM00 from 1900 to 2008 of (a) sea surface temperature, (b) temperature as a function of depth on the equator.

The method we use to calculate transport of the STC is similar to that of *McPhaden and Zhang* [2002]. We use 900m as the reference level for geostrophic calculations, and the lower branch of the STC is defined as equatorward flow below the surface mixed layer (using a 0.125 kg m^{-3} density difference criteria), within the density range of between 1022.5 − 1026.2 kg m^{-3} for the Southern Hemisphere and between 1022.0 − 1026.0 kgm^{-3} for the Northern Hemisphere. A latitude of 9°N is chosen to

calculate the strength of the STC because the potential vorticity ridge along 9°N in the Northern Hemisphere is a choke point, reducing the exchange of mass between the equator and the subtropics. The Southern Hemisphere latitude of 9°S is used by way of symmetry. Since potential vorticity in the Southern Hemisphere is more uniform than that in the Northern Hemisphere the latitude choice is not as critical. Subducted water in the extratropics flows back to the equator through either interior transport or via the western boundary current (WBC) transport, so geostrophic interior transport is integrated from the eastern boundary to 140°E in the Northern Hemisphere, and to 160°E in the Southern Hemisphere. The integration of the WBC transport is from the western boundary to 140°E in the Northern Hemisphere, and to 160°E in the Southern Hemisphere. The total transport is integrated from the eastern boundary to the western boundary in both hemispheres.

Schott et al. [2008] examine changes of the STC during the period from 1958 to 2005 using an earlier version of SODA. They describe significant interannual and decadal variability in the STC and accompanying changes of SST. Here we re-examine their results by using the SODA 2.2.6 data set. Both the interior and the WBC transport of the STC at 9°S have an increasing linear trend over the last one hundred years, with a trend of 1.8±0.19 Sv century^{-1} for the interior transport and 2.3±0.36 Sv century^{-1} for the WBC transport. This amounts to an increase of convergent transport of 4.1±0.65 Sv century^{-1} (Figure 23a). The interior transport at 9°N has an increasing trend of 2.7±0.45 Sv century^{-1}, while the WBC transport has an increasing trend of 1.9±0.38 Sv century^{-1}. As a result there is an overall trend of the total transport of the STC at 9°N of 4.5±0.69

Sv century^{-1} that is a little stronger than that at 9°S (Figure 23b). The net transport by the STC in both hemispheres displays a pronounced upward trend over the past century with a convergence of transport that increased by about 8.7±0.73 Sv century^{-1} (Figure 23c).

In addition to the long-term trend, substantial interannual and decadal variability can also be clearly seen. For example, the net transport is weaker in the 1890s-1910s, the 1930s-1940s and the 1970s-1990s, and stronger in the 1920s-1930s, the 1950s-1960s and the 2000s. By way of comparison, STC transport derived from hydrographic observational data [*McPhaden and Zhang*, 2002; 2004] is also plotted in Figure 23c. The STC transport in SODA 2.2.6 is a little weaker than the observations in the last few decades.

This may be a consequence of not using XBT (Expendable Bathythermograph) data in SODA 2.2.6. In order to investigate the influence of the introduction of XBT data into an ocean reanalysis we compare the STC transport in SODA 2.2.4 that assimilates XBT data with the STC transport in SODA 2.2.6. The STC transport in SODA 2.2.4 is generally consistent with the observations (Figure 24). However, the long-term trend of the STC transport is stronger in SODA 2.2.4 than that in SODA 2.2.6 which means that the assimilation of XBT affects the long-term change of the STC.

Our analysis suggests an increasing trend of the STC transport over the last hundred years. Increasing of the STC transport means that more cold thermocline water in the subtropics is advected to the equatorial thermocline, consistent with the cooling trend in the subsurface equatorial ocean. Cold anomalies in the equatorial thermocline can reach the surface through enhanced equatorial upwelling.

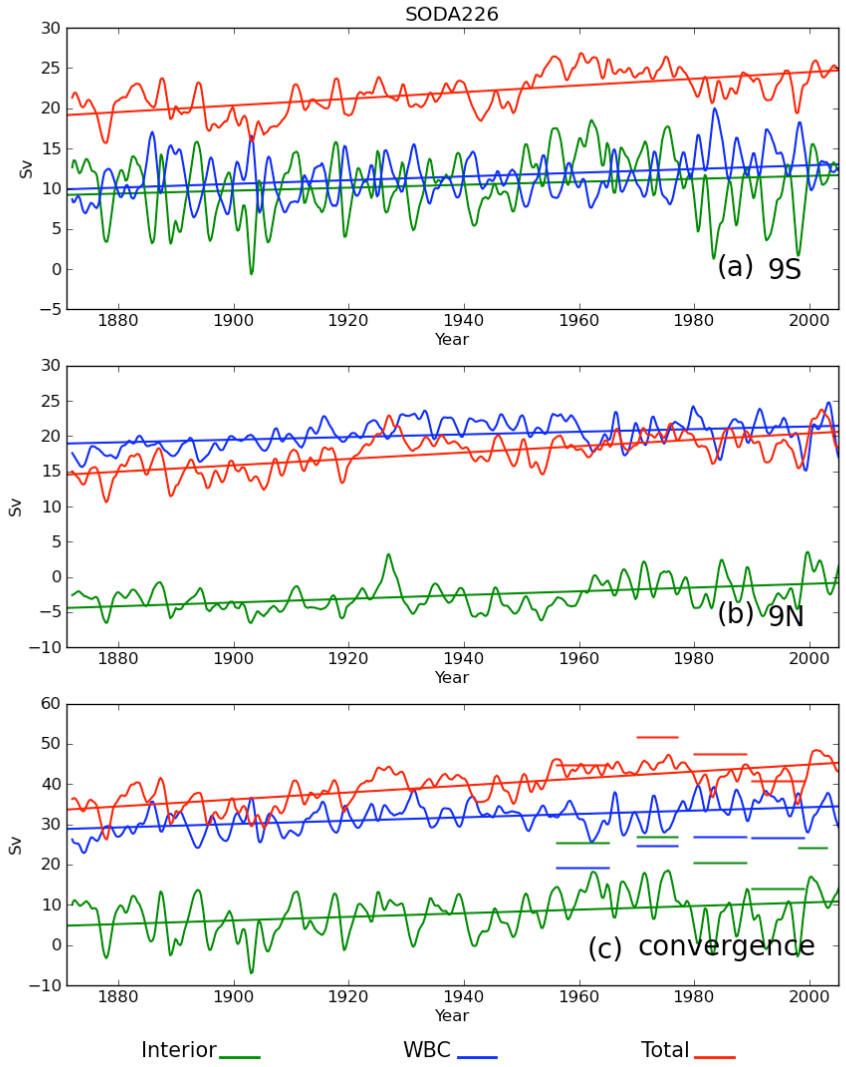

Figure 23. Transport of the STC in SODA 2.2.6 at (a) 9°S, (b) 9°N, and (c) convergence transport between 9°S and 9°N. Green lines indicate interior transport, blue lines represent western boundary current transport and red lines display total transport (see text for description). Values from *McPhaden and Zhang* [2002, 2004] are shown as bars in (c).

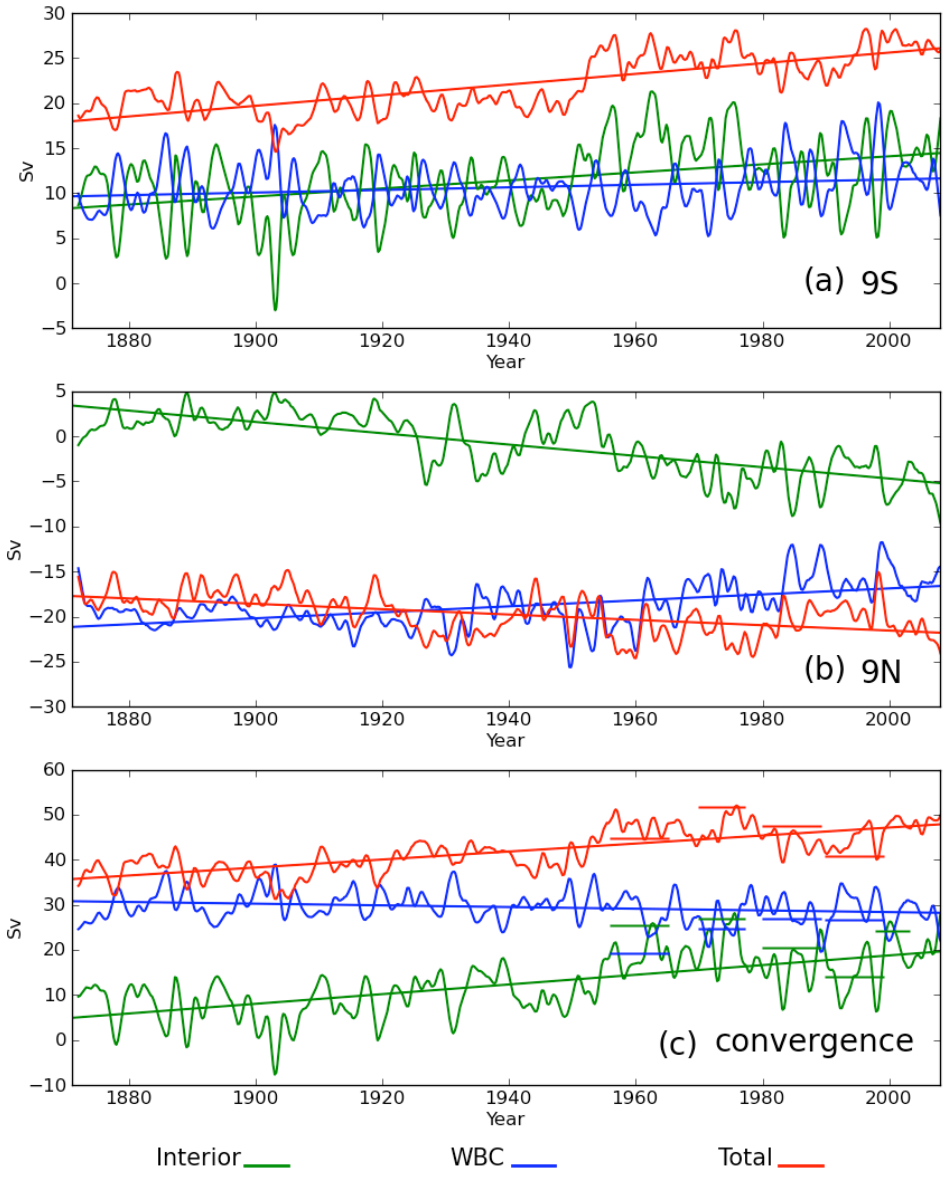

Figure 24. Transport of the STC in SODA 2.2.4 at (a) 9°S, (b) 9°N, and (c) convergence transport between 9°S and 9°N. Green lines indicate interior transport, blue lines represent western boundary current transport and red lines display total transport (see text for description). Values from *McPhaden and Zhang* [2002, 2004] are shown as bars in (c).

Coupled Model Intercomparison Project Phase 5 (CMIP5)

ENSO Metrics in CMIP5

As the newest coupled model intercomparison project, it is important to evaluate the quality of CMIP5 simulations. Due to the importance of ENSO to global climate, the simulation of ENSO is an important metric to validate coupled models. Since the Niño 3.4 SST anomaly is a widely used metric to represent the simulation of ENSO, we begin by comparing Niño 3.4 SST anomalies in the various models. Niño 3.4 SST in SODA 2.2.6 and from one ensemble member from CMIP5 models including HadCM3, MIROC-ESM and BCC, is shown in Figure 25 with a blue line and the 11-year climatology is shown with a red line. The reason we use the 11-year climatology is that most of the CMIP5 historical runs have prominent trends or low frequency variability. The background state has impacts on ENSO variability that makes it difficult to determine whether it is ENSO that is changing or it is the background state that is changing. A previous study shows that the use of 11-year has a little difference on ENSO amplitude [*Giese and Ray*, 2011].

The reason we choose these three models (HadCM3, MIROC-ESM and BCC) is that they span the range of seasonal cycle and interannual variability in CMIP5 models. In HadCM3, the amplitude of the seasonal cycle is very similar to that in SODA 2.2.6. ENSO in HadCM3 also has prominent decadal variability, also similar to that in SODA 2.2.6. However, the amplitude of the seasonal cycle in MIROC-ESM is very large, almost as twice as big as the seasonal cycle in SODA 2.2.6. Interannual variability in MIROC-ESM is very small and has little decadal variability. Another noticeable feature

of MIROC-ESM is that Niño 3.4 SST has an increasing trend of about 1°C over the last 150 years. In the BCC model the amplitude of the seasonal cycle is weak (at about just 1°C), and interannual variability is relatively strong. Similar to MIROC-ESM, Niño 3.4 SST in BCC has an increasing trend of around 1°C over the last 160 years.

In order to evaluate all the CMIP5 models, the amplitude of the seasonal cycle is plotted as a function of the amplitude of interannual variability and is shown in Figure 26. The amplitude of the seasonal cycle is taken to be the standard deviation of the climatology determined by the entire record, which is close to the standard deviation of the 11-year climatology with the linear trend removed. The interannual variability is the difference between Niño 3.4 SST and the 11-year climatology. Error bars represent plus and minus one standard deviation between all the ensemble members. Generally, most of the CMIP5 models have reasonable seasonal cycles and interannual variability that are close to ocean reanalysis. One noticeable feature is that the ensemble spread for interannaul variability is larger than the seasonal cycles. Some models (BCC, GISS-E2-R and NorESM1-M) have weak seasonal cycles, but with a larger range of interannual variability. MIROC-ESM has a very strong seasonal cycle but relatively weak interannual variability as shown in Figure 25. Overall, there is a weak correlation between seasonal cycle and interannual variability, such that the CMIP5 models tend to have strong ENSO if the models have strong seasonal cycles and vice versa.

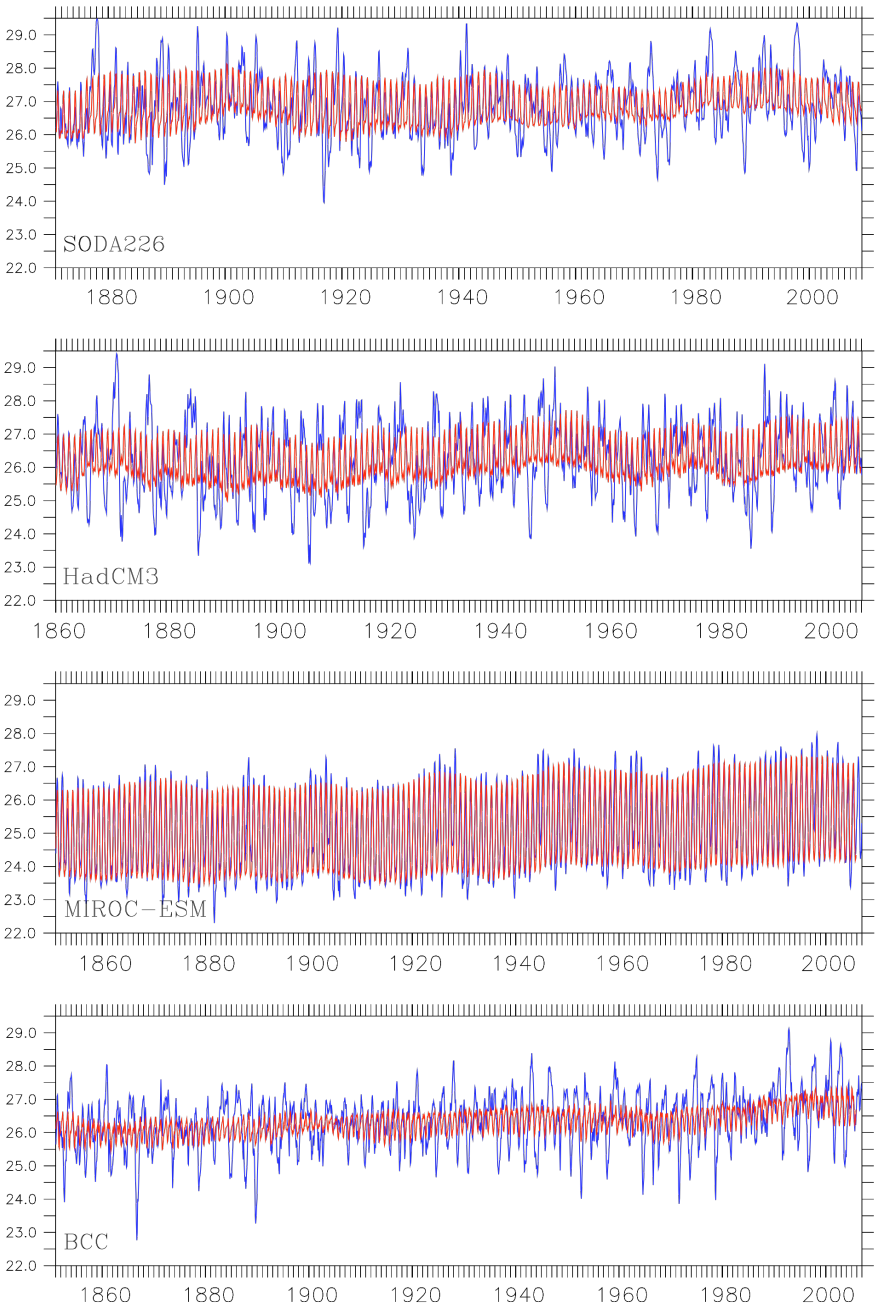

Figure 25. Niño 3.4 SST in blue and an 11-year climatology is shown in red for SODA 2.2.6, and the HadCM3, MIROC-ESM and BCC models.

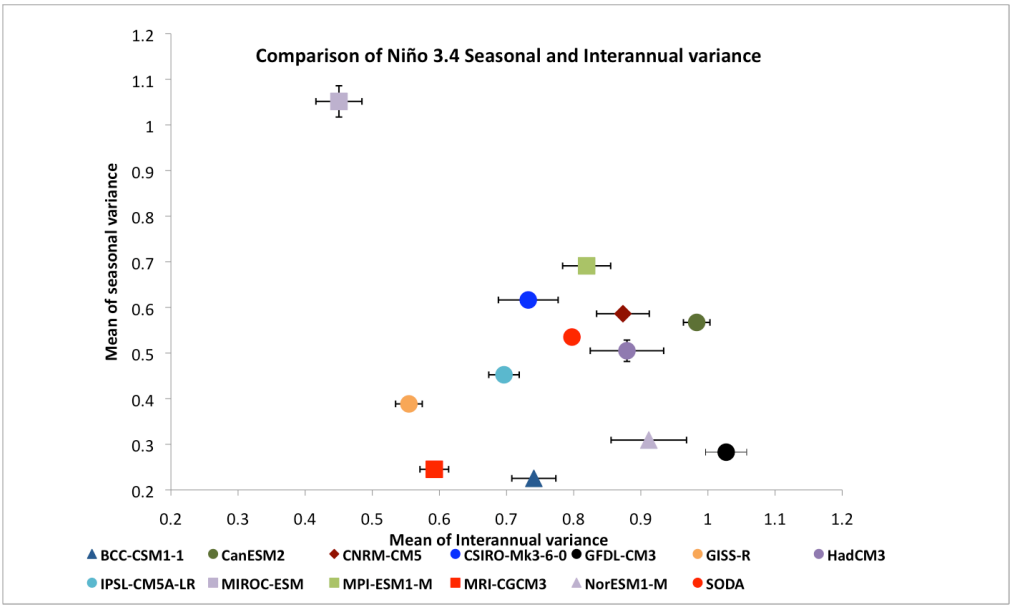

Figure 26. Seasonal cycle as a function of interannual variability in SODA 2.2.6 and for several CMIP5 models. The error bar shows +/-1 standard deviation between ensemble members.

CHI can be used to compare ENSO variability in CMIP5 with ENSO variability in SODA 2.2.6. Before investigating ENSO variability the spatial pattern of El Niño in the CMIP5 models is examined (Figure 27 and Figure 28) to get a sense of how the coupled models capture ENSO. The SST anomaly shown in the figure is the average of the SST anomaly for months when CHI exists. Figure 27a and Figure 28a shows the SST anomaly in SODA 2.2.6. In SODA 2.2.6, the warmest SST anomaly is located in the central-eastern tropical Pacific from 140°W to 110°W with a maximum of around 1.4°C. The warm anomaly in SODA 2.2.6 also extends to the coast of South America.

The spatial pattern of warm anomaly in the CMIP5 models is shown in Figure 28b-h and Figure 28b-f. The amplitude and the location of the warm anomalies have a wide range for the CMIP5 models. For example, in NorESM1-M and CNRM-CM5, the

amplitude of the warm anomaly is about 1.8°C, whereas in MIROC-ESM and IPSL-CM5A-LR the amplitude of the warm anomaly is about 0.8°C. The location of warm anomaly in most of the CMIP5 models extends to the western tropical Pacific Ocean. This is especially noticeable in CSIRO-Mk3-6-0. The other issue for most of the CMIP5 models is that there is little warming along the coast of South America. Despite the diversity of the spatial patterns of warm anomalies, in most of the models the maximum of the warm anomaly is located in the central tropical Pacific Ocean and the amplitude of the warm anomaly is fairly similar to the observations. Because of the diversity of the spatial patterns of warm anomalies in the CMIP5 models, a fixed SST anomaly index such as Niño 3.4 SST would not give accurate estimate of the strength of ENSO. The CHI, not based on a fixed longitude, may give a better estimate of ENSO characteristics.

The CHI amplitude that represents the strength of El Niño in SODA 2.2.6 and the CMIP5 models is plotted in Figure 29. The ensemble mean of CHI amplitude is shown as a red dot, and error bars represent minus and plus one standard deviation between ensemble members. In SODA 2.2.6, the strength of El Niño is around 1.05°C with a standard deviation of around 0.25°C. It is encouraging that overall the strength of El Niño in most of the CMIP5 models is close to the strength of El Niño in the ocean reanalysis. In some models, such as GISS-E2-R and MIROC-ESM El Niño is too weak, while in CanESM and NorESM1-M the strength of El Niño is too strong. However, the difference of El Niño strength between models and the ocean reanalysis is modest, which means that the strength of El Niño in most of the CMIP5 models is realistic.

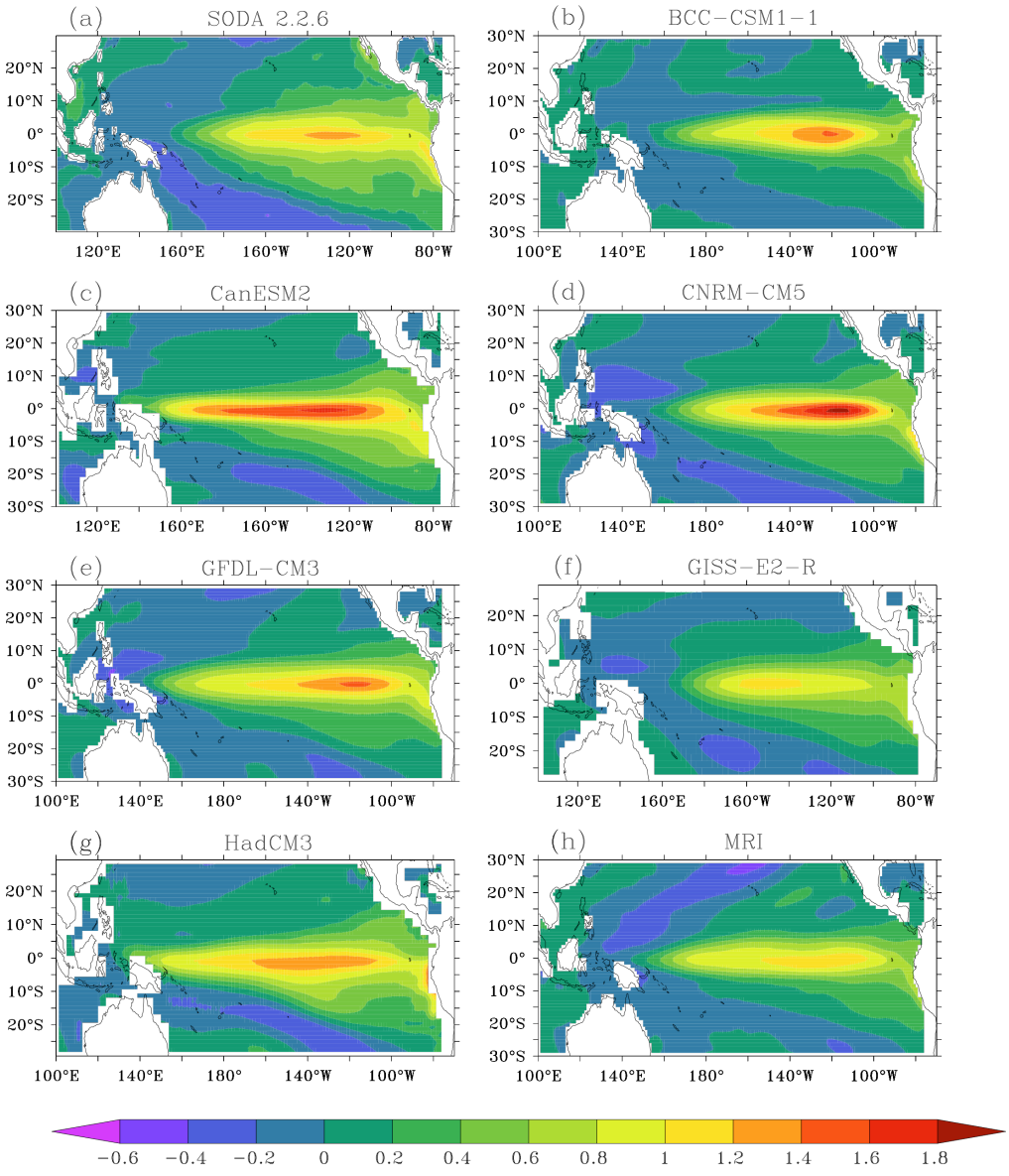

Figure 27. Averaged warm SST anomaly for months when CHI exists in SODA 2.2.6 and the CMIP5 models.

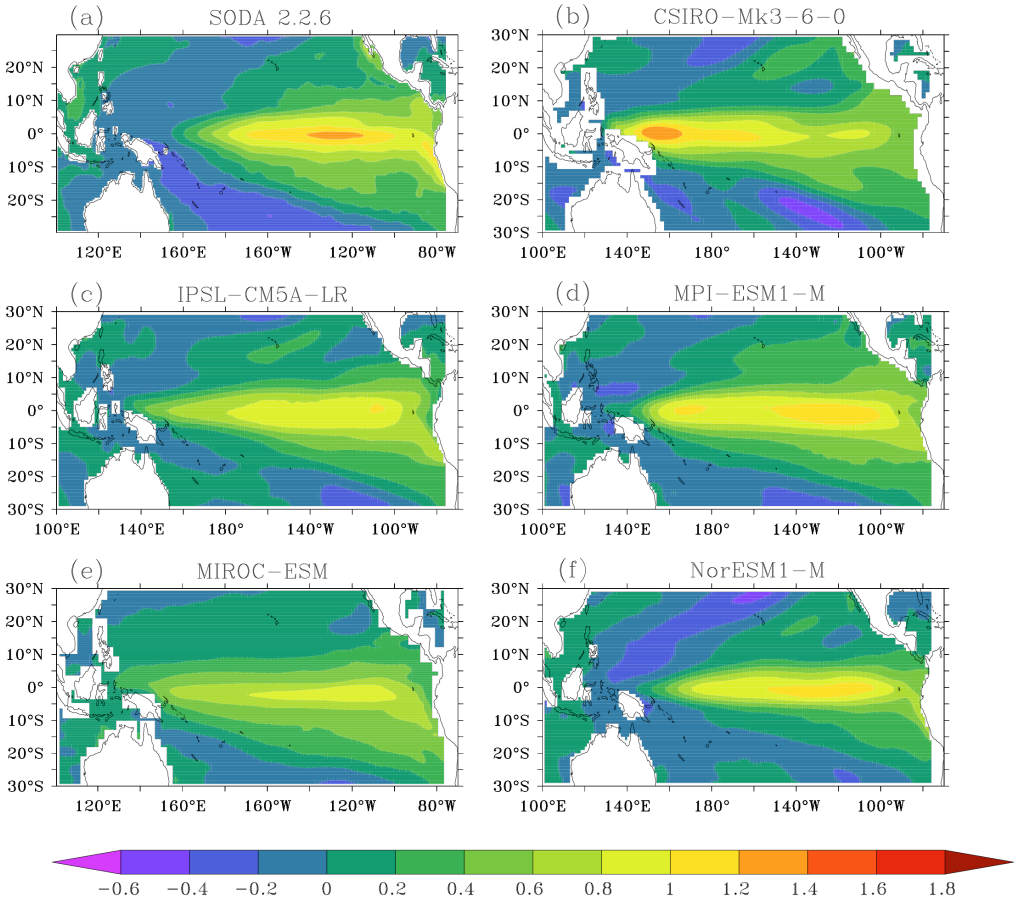

Figure 28. Averaged warm SST anomaly for months when CHI exists in SODA 2.2.6 and the CMIP5 models.

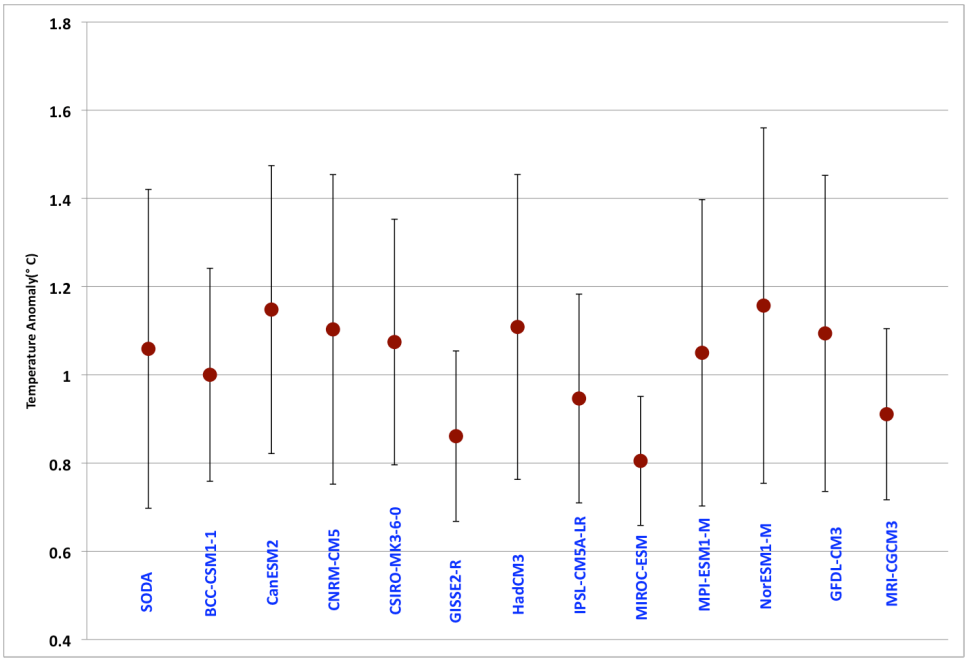

Figure 29. The ensemble mean of CHI amplitude for warm events in SODA 2.2.6 and the CMIP5 models with error bars representing CHI amplitude variability.

The CHI longitude that represents the location of the warm anomaly in SODA 2.2.6 and the CMIP5 models is shown in Figure 30. Similar to Figure 29, the ensemble mean of CHI longitude is plotted with a red dot and the errors bars represent one standard deviation between ensemble members. The averaged location of El Niños in SODA 2.2.6 is at around 139.5°W, which is located in the central tropical Pacific Ocean. Compared to the reanalysis, in most of the CMIP5 models the average location of El Niño is too far to the west in the tropical Pacific Ocean as shown in Figure 28. For example, in CSIRO, the average location of El Niño is at about 160°W as shown in Figure 28. However, in some models, the average location of El Niño is in the eastern tropical Pacific Ocean, such as NorESM in which El Niño is centered at 130°W. Overall,

in most of the CMIP5 models the location of El Niño extends too far west in the tropical Pacific Ocean.

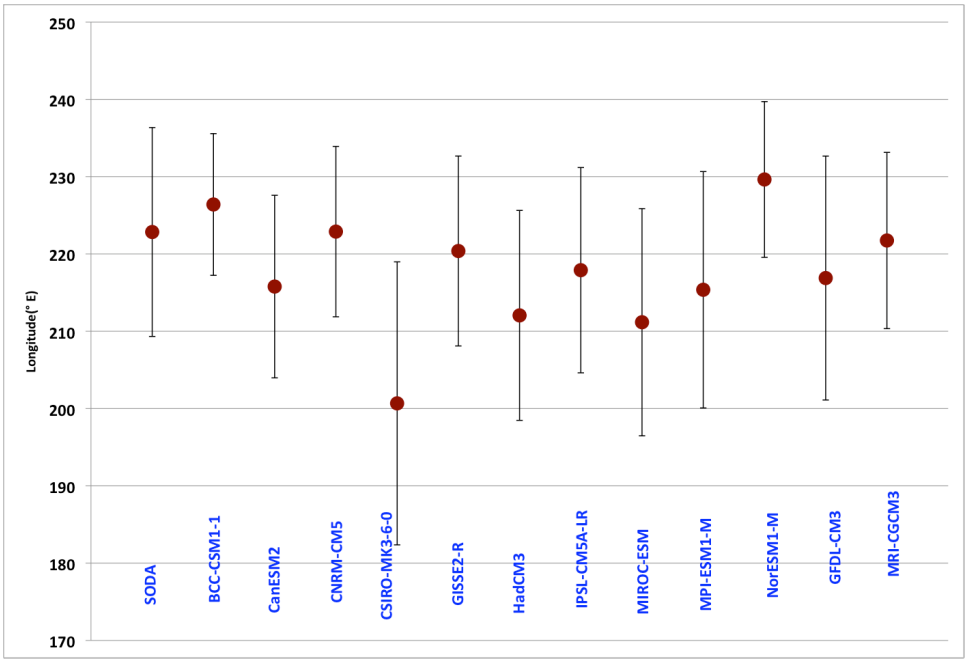

Figure 30. The ensemble mean of CHI longitude for warm events in SODA 2.2.6 and the CMIP5 models plotted with a red dot. The error bars represent CHI location variability.

The characteristics of La Niña in the CMIP5 models are also evaluated based on the CHI indices. The CHI amplitude that represents the strength of La Niña in SODA 2.2.6 and the CMIP5 models is shown in Figure 31. The blue dots show the ensemble mean of CHI amplitude in SODA 2.2.6 and the CMIP5 models, and the error bars represent the standard deviation between ensemble members. In SODA 2.2.6, the amplitude of La Niña is of about -0.95°C, and the standard deviation is about 0.2°C. Overall, in most of the CMIP5 models the strength of La Niña is close to SODA 2.2.6. In

some of the models, such as GISS-E2-R, MIROC-ESM and NRI-CGCM3, the strength of La Niña is very weak, while CanESM2 and GFDL-CM3 have relatively strong La Niñas. Compared to La Niña, the amplitude of El Niño in the CMIP5 models is closer to the reanalysis, which means that the CMIP5 models have better simulation of El Niño than La Niña.

The ensemble mean of the La Niña location is shown in Figure 32 with blue dots, and the error bars represent one standard deviation between ensemble members. La Niña in SODA 2.2.6 is located in the central tropical Pacific at around 140°W. In most of the CMIP5 models the location of La Niña extends too far west in the tropical Pacific, which is similar to El Niño conditions. The extremes are represented by CSIRO in which the location of La Niña is at about 160°W. In NorESM, La Niña is located further east in the tropical Pacific. Generally, the CHI amplitude for El Niño events in the CMIP5 models is more realistic than for La Niña events, and the location of both El Niño and La Niña extends too far west.

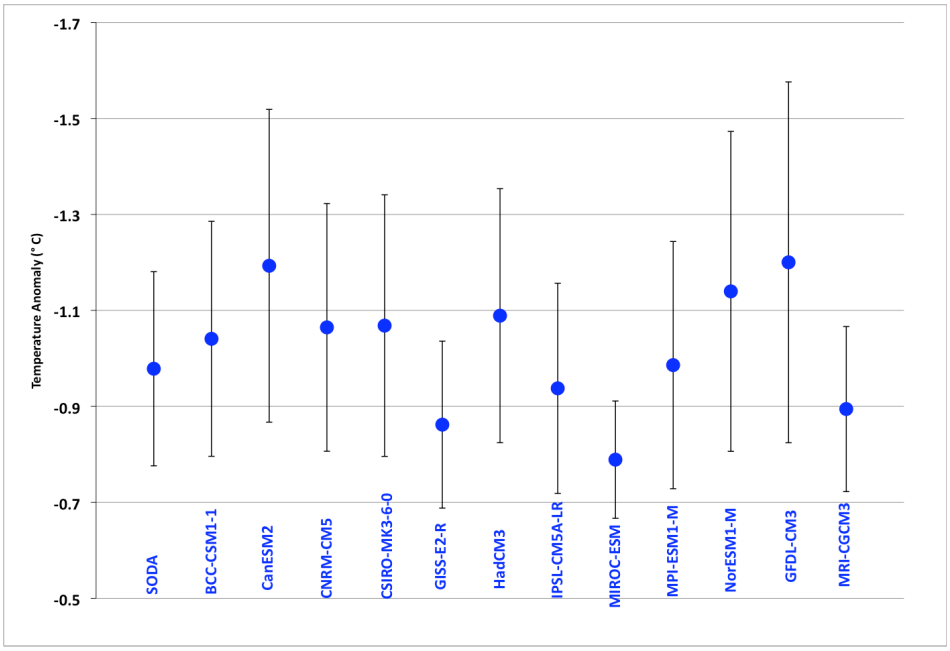

Figure 31. The ensemble mean of CHI amplitude for cold events in SODA 2.2.6 and the CMIP5 models.

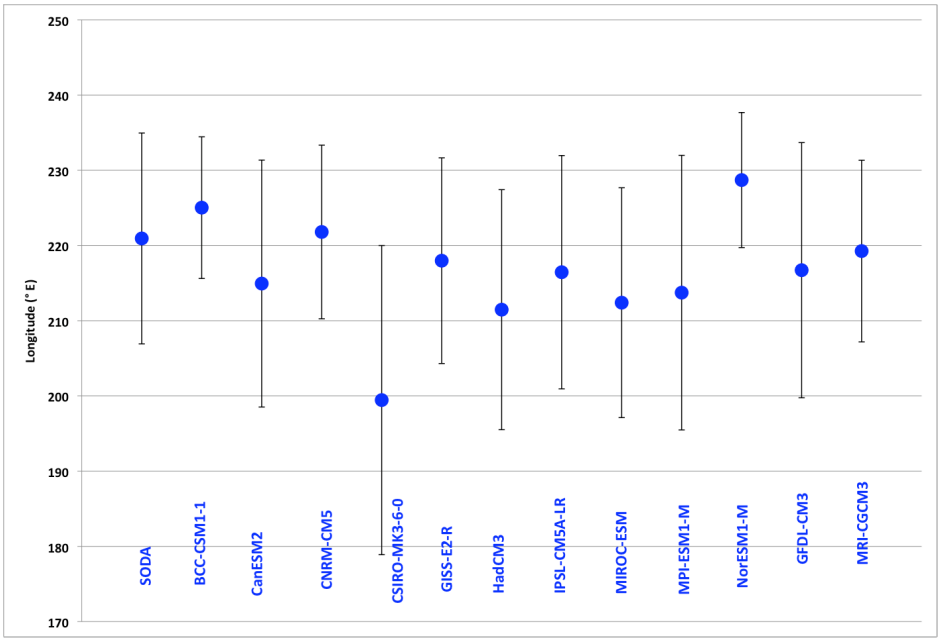

Figure 32. The ensemble mean of CHI longitude for cold events in SODA 2.2.6 and the CMIP5 models.

The CHI amplitude for warm events in SODA 2.2.6 shown in Figure 29 is around 1.1°C, and for cold events (Figure 31) the CHI amplitude is around -1.0°C, which indicates that El Niño is stronger than La Niña in SODA 2.2.6. The location of El Niño and La Niña shown in Figure 30 and Figure 32 is also different. The different strength and location of El Niño and La Niña show an asymmetry of El Niño and La Niña and high frequency wind stress plays an important role in this phenomenon. The asymmetry of El Niño and La Niña is an important feature that the CMIP5 models should capture. Unfortunately, most of the coupled models fail to capture the asymmetry of El Niño and La Niña or just exhibit different features of the asymmetry from observations [*Hannachi et al.*, 2003; *Monahan and Dai*, 2004].

In order to evaluate the CMIP5 models, the amplitude of El Niño and La Niña in SODA 2.2.6 and the CMIP5 models is summarized in Figure 33. The CHI amplitude of El Niño and La Niña in SODA 2.2.6 is shown with a red dot, and the error bars represent the CHI amplitude variability. The strength of El Niño in SODA 2.2.6 is about 1.1°C and the strength of La Niña is about -1.0°C. The CHI amplitude in the CMIP5 models is shown with black dots and the error bars represent the CHI amplitude variability. Generally, in most of the CMIP5 models the amplitude of El Niño and La Niña is similar. The exception is for CNRM, in which El Niño is slightly stronger than La Niña. In CanESM, even though the amplitude of El Niño and La Niña is different, La Niña is a little stronger than El Niño giving an asymmetry that is the opposite of the observations. Overall, most of the CMIP5 models do not capture the asymmetry of El Niño and La Niña.

There are two possible reasons for the symmetry of El Niño and La Niña in the CMIP models. First, from the spatial pattern of El Niño in the CMIP5 models we can see that El Niño extends too far to the west (Figure 28), and likewise the spatial pattern of La Niña (not shown) also shows that La Niña extends too far to the west. This bias may come from the representation of the cold tongue in the CMIP5 models, which is too narrow and extends too far to the west. The cold bias may affect the simulation of La Niña more than El Niño. Figures 30 and 32 shows that the amplitude of El Niño in the CMIP5 models is closer to the ocean reanalysis than the amplitude of La Niña in the CMIP5 models. In order to have an accurate simulation of ENSO, the representation of cold tongue in the CMIP5 models must improve. The other possible reason may come from the low resolution of the coupled models. In the last section, we suggest that high frequency wind stress may play an important role in the asymmetry of El Niño and La Niño. In coupled models the resolution, especially in the tropical Pacific, is low so that the models may not accurately simulate high frequency variability. Increasing the resolution of the coupled models may help to improve the simulation of the asymmetry between El Niño and La Niña.

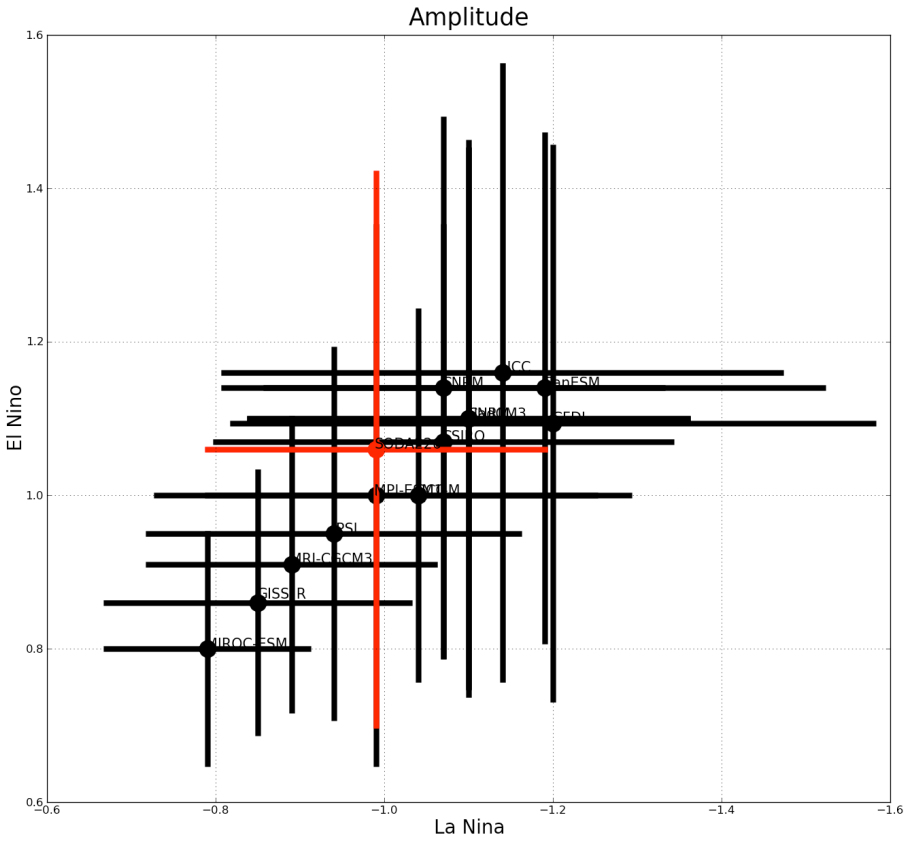

Figure 33. CHI amplitude for El Niño and La Niña in SODA 2.2.6 (red) and the CMIP5 models (black).

The importance of ENSO on global climate has made it the subject of intensive studies. Long-term changes of ENSO have also been discussed by previous studies [*Giese and Ray*, 2011], especially the response of ENSO to global warming [*Merryfield*, 2006; *Vecchi and Wittenberg*, 2010]. However, there is still little understanding of the long-term changes in ENSO, and there is still debate about the response of ENSO to global warming in coupled models. In the ensemble reanalysis, ENSO has prominent

decadal variability and a weak long-term trend. To compare with the ensemble ocean reanalysis, we analyzed long-term trends of ENSO in the CMIP5 models.

The long term trend of CHI amplitude of El Niño in SODA 2.2.6 and the CMIP5 models is shown in Figure 34 with the red dots representing the ensemble mean and error bars giving the ensemble spread. In SODA 2.2.6, the strength of El Niño does not change much in the last century. In most of the CMIP5 models, similar to SODA 2.2.6, the long-term trend of El Niño amplitude is close to zero. In HadCM3, El Niño has a weak decreasing trend with a value of -0.1°C century^{-1} and in MRI-CGCM3 El Niño is weakens in the last century. Some of the CMIP5 models have an increasing trend for El Niño, for example MPI-ESM1-M has an increasing trend of about 0.12°C century^{-1}. Every model has several ensemble members, and the ensemble spread is relatively large. Therefore, in some of the ensemble members El Niño tends to be weakening, while in other ensemble members El Niño tends to be strengthening. Overall, the long-term trend of El Niño amplitude is not significant in most of the CMIP5 models. The long-term change of El Niño location is also analyzed in the CMIP5 models (Figure 35). Similar to Figure 34, the red dots represent the ensemble mean of the long-term trend of El Niño location and the error bars give the ensemble spread of the long-term trend. In SODA 2.2.6, the location of El Niño tends to move toward to the western tropical Pacific by 2.2°century^{-1}. In most of the CMIP5 models, the location of El Niño does not change in the last century. In MIROC-ESM and IPSL El Niño tends to move toward the western tropical Pacific similar to SODA 2.2.6. In GISS-E2-R and NorESM El Niño tends to move toward the eastern tropical Pacific Ocean with a linear trend of about 2°century^{-1}.

The long-term trend of La Niña amplitude and location has also been analyzed for SODA 2.2.6 and the CMIP5 models (Figures 36 and 37). In SODA 2.2.6, La Niña amplitude has a weak increasing trend similar to El Niño. However, in most of the CMIP5 models, La Niña does not change very much in the 20th Century. Three noticeable exceptions are CSIRO, GISS-E2-R and MPI-ESM. These models have La Niña that is weakening in the 20th Century. The location of La Niña in SODA 2.2.6 moves toward the western tropical Pacific Ocean in the 20th Century similar to El Niño in SODA 2.2.6. As with strength in most of the CMIP5 models the location of La Niña does not change very much in the 20th Century. The exceptions are GISS-E2-R and GFDL in which La Niña tends to move to the eastern tropical Pacific Ocean. In MIROC-ESM La Niña tends to move to the western tropical Pacific Ocean, similar to that observed in SODA 2.2.6. Interestingly, the ensemble spread for the long-term trend of CHI amplitude and CHI location are large. Thus the uncertainty of trends is large enough that the trends are not significantly different from zero.

Overall, in most of the CMIP5 models, ENSO does not change much in the 20th Century, a result that is similar to what is found in SODA 2.2.6. The location of the ENSO in most of the CMIP5 models does not change much either, and this is different from SODA 2.2.6 where both El Niño and La Niño tend to move toward the western tropical Pacific Ocean.

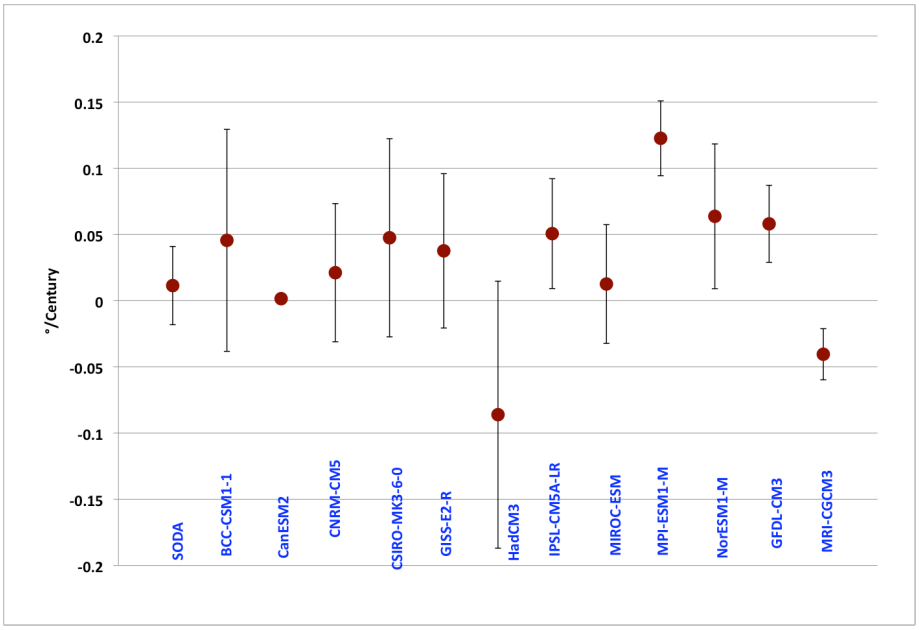

Figure 34. Long-term trends of CHI amplitude for warm events in SODA 2.2.6 and the CMIP5 models with error bars representing the ensemble spread.

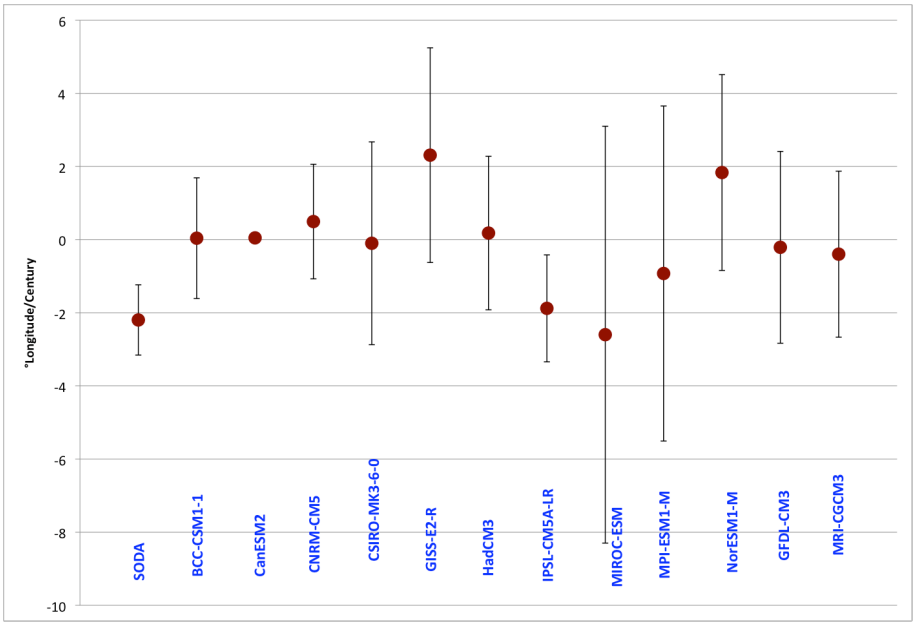

Figure 35. Long-term trends of CHI longitude for warm events in SODA 2.2.6 and the CMIP5 models with error bars representing the ensemble spread.

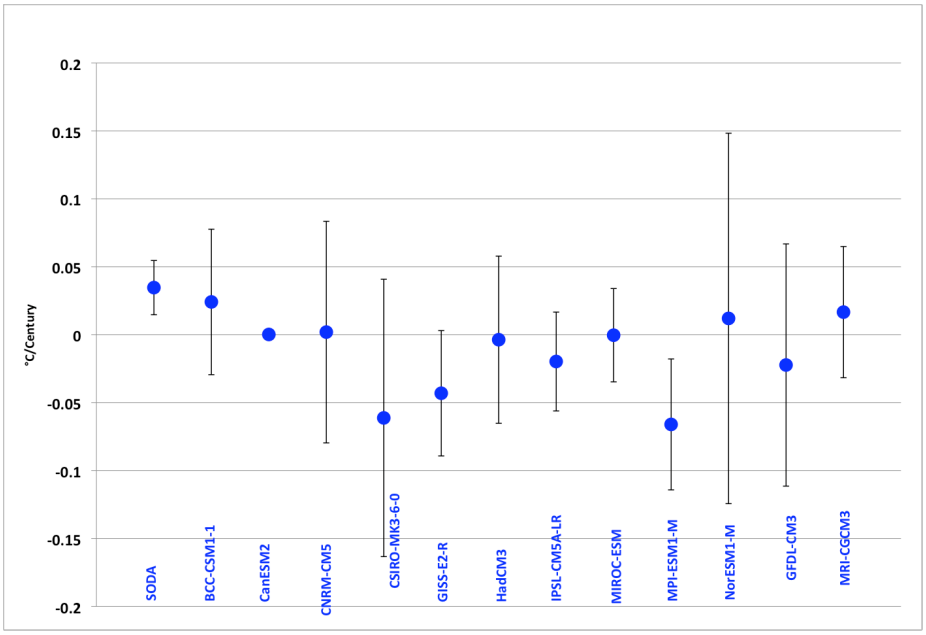

Figure 36. Long-term trends of CHI amplitude for cold events in SODA 2.2.6 and the CMIP5 models with error bars representing the ensemble spread.

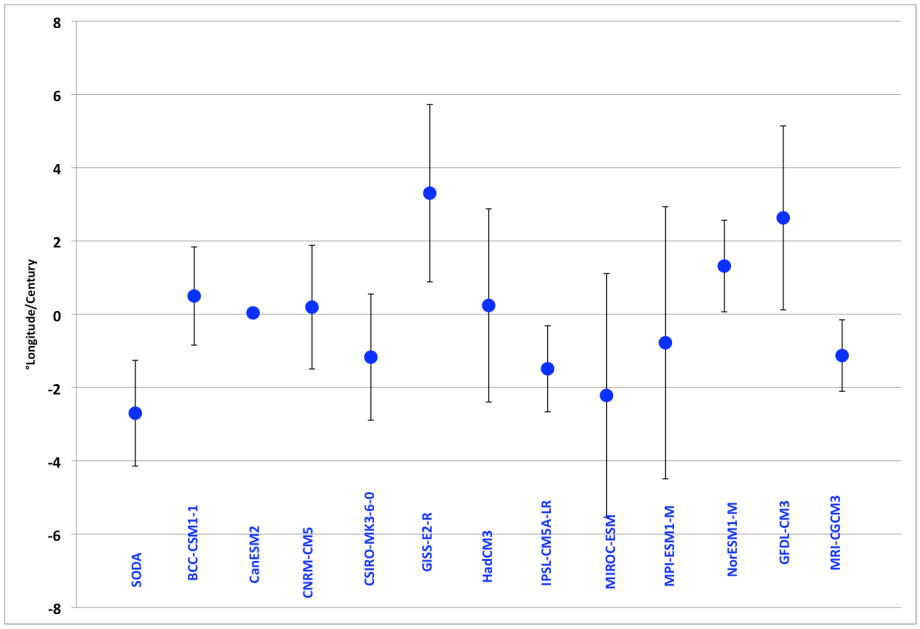

Figure 37. Long-term trends of CHI longitude for cold events in SODA 2.2.6 and the CMIP5 models with error bars representing the ensemble spread.

Sub-tropical Cells (STCs)

Most of the CMIP5 models realistically simulate ENSO although the variability of ENSO is different than in SODA 2.2.6. The background state of the tropical Pacific Ocean has significant impact on ENSO variability and the role of ocean dynamics in the long-term changes of ENSO in SODA 2.2.6 has been discussed. In order to verify the robustness of the role of ocean dynamics in regulating tropical Pacific climate we investigate the long term change in the tropical Pacific background state in the CMIP5 models.

We first examined long-term trends of tropical Pacific SST from 1900 to 2005 using the same least squares method that was used for SODA 2.2.6. Most of the CMIP5 models have a warming SST trend but with a wide range of amplitudes (Appendix A1-A12). The pattern of warming area is considerably different between the CMIP5 models. Several of the CMIP5 models have strong warming trends of around 0.9°C century^{-1} across the tropical Pacific Ocean (BCC, CanESM, IPSL, MIROC-ESM and MPI), however, the pattern of warming in these models is different from each other. For example, the strongest trend in BCC is in the central tropical Pacific Ocean of 0.9°C century^{-1}, whereas in CanESM it is very narrow in the western Pacific while wide in the eastern tropical Pacific Ocean. IPSL has a uniformly strong trend from the western to the eastern tropical Pacific Ocean. The strongest warming trend in MIROC-ESM is located in the western tropical Pacific Ocean, but in MPI it is located in the eastern tropical Pacific Ocean.

In HadCM3 and MRI there is also a strong warming trend but in both models the warming is located in the western tropical Pacific Ocean. In HadCM3, the SST trend in the eastern tropical Pacific Ocean is weak except along the west coast of South America. In MRI there is a cooling trend in the eastern tropical Pacific Ocean of around -0.4°C century^{-1}. In the remaining models (CNRM, CSIRO, GFDL and NCC) tropical Pacific SST has a very weak warming trend. Especially in GFDL there is almost no trend in the tropical Pacific Ocean, and interestingly, there is warming that is located in the eastern southern Pacific Ocean.

In order to better understand the mechanisms responsible for the warming trend of tropical Pacific SST, long-term trends of subsurface temperature on the equator are also calculated. Most of the CMIP5 models have a cooling trend in the western tropic Pacific Ocean at a depth of around 200 m (Appendix Figure A1- Figure A12) although the amplitude of the trend has a wide range. Some of the models (CNRM, CSIRO, HadCM3 and NCC) have a weak subsurface cooling trend consistent with the weak warming trend in the surface. In contrast, in the BCC model the cooling trend in the subsurface is weak while the warming trend of SST is relatively strong. Some of the models have a strong cooling trend in the subsurface (CanESM, MIROC-ESM, MRI, GISS and MPI) accompanied by a strong SST warming trend. Even though the GFDL model has a weak warming trend, the subsurface of GFDL has a strong cooling trend. In IPSL, the subsurface ocean has a weak warming trend that stands in contrast to all other CMIP5 models.

In the tropical Pacific Ocean ocean-atmosphere interaction feedback plays an important role in regulating tropical Pacific climate. To explore the impact of this feedback the long-term trend of wind stress from 1900 to 2005 in the CMIP5 models is analyzed. In most of the CMIP5 models equatorial wind stress weakens (Appendix Figure A1-Figure A12). The weakening of the wind stress reduces the slope of equatorial thermocline and so in the eastern tropical Pacific Ocean the depth of equatorial thermocline is deeper and in the western tropical Pacific Ocean it is shallower. In the eastern tropical Pacific Ocean the weakening of wind stress reduces the equatorial upwelling resulting in warming both the surface and the subsurface water. In the western tropical Pacific Ocean, due to the shoaling of the thermocline, the subsurface has a cooling trend that might give rise to cooler SST. However, in the western tropical Pacific Ocean there is a warming SST trend. This may come from increasing latent heat flux resulting from the weakening of equatorial wind speed. Weakening equatorial wind speed causes warming SST and subsurface temperature in the eastern and cooling subsurface temperature in the western tropical Pacific Ocean. The latent heat flux plays an important role in producing the warming surface temperature in the western tropical Pacific Ocean.

In SODA 2.2.6, the easterly trade winds strengthen which accelerates the transport of the STC. In contrast, in most of the CMIP5 models, the easterly trade winds weakens, which presumably will decelerate the strength of the STCs and reduce the equatorial upwelling. In order to investigate the role of the STC, transports of the STC are calculated with the same method as that used for SODA 2.2.6. These results are

shown in Appendix Figures A13-A24. Due to the large number amount of figures, only the total transport of the STC (the integration of from the eastern boundary to the western boundary) is shown. The dashed lines show the STC transport from each ensemble member, and the thick black line is the ensemble mean of the STC transport. The linear trend of the transport is shown with a red line. The STC in most of the models (BCC, CanESM, CNRM, GFDL, HadCM3, MIROC-ESM, MRI and NCC) has a weakening trend, which is consistent with the weakening of the wind stress. In the CSIRO and GISS models, the STC does not change significantly which is consistent with the weak trend of the SST. In IPSL, even though there is a warming trend at the surface and the subsurface, in the Southern Hemisphere the trade winds strengthen, accelerating the STC.Generally, most of the CMIP5 models have weakening equatorial upwelling due to the weakening of the STC. Less cold water from the deep ocean comes to the surface resulting in a warming surface consistent with the warming trend of SST. The lower branch of the STC from the subtropics to the tropics slows down at the same time resulting in a warming subsurface. Even though SODA 2.2.6 has a cooling trend at the surface, in most of the CMIP5 models there is a warming SST trend, the change of the STC and equatorial wind stress are consistent with this change in SST.

CHAPTER IV

SUMMARY AND CONCLUSIONS

An ensemble ocean reanalysis that spans from 1871 to 2008 is used to analyze ENSO variability. The advantage of using the ensemble reanalysis is that uncertainty in the variability can be evaluated by the ensemble spread. This ensemble reanalysis, SODA 2.2.6, consists of eight members, each forced with output from different ensemble members from the 20CRv2 atmosphere reanalysis. In order to avoid spurious variability due to the introduction of new observation systems, we only assimilate ICOADS 2.5 SST into SODA 2.2.6. This is different from previous versions of SODA which assimilated all available hydrographic data.

Using Center of Heat Index (CHI) metrics including CHI amplitude, CHI longitude and CHI area, ENSO variability is analyzed using the ensemble mean of SODA 2.2.6. The SST anomaly is calculated by subtracting an 11-year running climatology to avoid the influence of changing background state on ENSO variability. In SODA 2.2.6, CHI amplitude, which measures the strength of ENSO events, for a warm event has prominent decadal variability with strong El Niño events from the beginning of the record to the 1920s, and from the 1970s to the end of the 20th century. Weak El Niños occur across the entire record but the occurrence of strong El Niño events changes. The location of El Niño varies from east of the Dateline to 100°W and has considerable variability. However, unlike CHI amplitude, there is no clear decadal signal for CHI longitude. The CHI area displays pronounced decadal variability with large area

events from the 1870s to the 1920s and the 1970s to 2008. The CHI area is smaller from the 1920s to the 1970s.

Compared to SODA 2.2.4, which is forced with the ensemble mean of an atmospheric reanalysis, CHI longitude in SODA 2.2.6 is similar to CHI longitude in SODA 2.2.4. However, CHI amplitude and CHI area are different in SODA 2.2.6. In SODA 2.2.4, there are strong El Niños in the beginning of the record and CHI area has a slightly decreasing trend that does not occur in SODA 2.2.6. Because forcing in SODA 2.2.4 comes from the ensemble mean of 20CRv2, high frequency wind stress variability is averaged out so that in the western Pacific the wind speed is weaker. The weaker wind speed in the western tropical Pacific results in a strong zonal SST gradient and so strengthens El Niño. Since there were few observations in the beginning of the record, it is during this time that the difference between these two reanalyses is more obvious. With a weaker SST gradient it is also possible that there is less area that meets the greater than 0.5°C criteria in SODA 2.2.6 in the beginning of the record, so that this run does show the same decrease in CHI area in SODA 2.2.4.

The characteristics of cold events in SODA 2.2.6 are calculated based on CHI metrics. Compared with El Niño events, the CHI amplitude for La Niña is smaller and has less variability. All three characteristics of La Niña events, CHI amplitude, CHI longitude and CHI area tend to be more uniform without distinguishable variation across the entire record.

El Niño is stronger than La Niña in SODA 2.2.6, consistent with the asymmetry seen in the observations. The role of high frequency wind stress in the asymmetry of El

Niño and La Niña is investigated with the 5-day data from SODA 2.2.6. For weak wind stress anomalies the frequency of westerly wind anomalies and easterly wind anomalies are very similar. There are more strong westerly wind anomalies than strong easterly wind anomalies. Some studies suggest that a westerly wind event may trigger El Niño events, and so more westerly wind anomalies may result in stronger and more El Niño events. This may explain the asymmetry between El Niño and La Niña. The frequency of westerly wind anomalies is also investigated separately for El Niño events, La Niña events and neutral conditions. This analysis shows that for weak wind stress anomalies, the frequency of maximum westerly wind anomalies is similar for all conditions and the magnitude at the peak frequency is about 0.2-0.4Nm^{-1}. For strong wind stress anomalies, there are more strong westerly wind bursts during El Niño events than during La Niña events or neutral conditions. Again this may contribute to the asymmetry between El Niño and La Niña.

The frequency of easterly wind anomalies during El Niño events, La Niña events and neutral conditions is also investigated. For weak easterly wind anomalies, the frequency of the maximum easterly wind anomalies is similar for all three conditions, similar to what we found for westerly wind anomalies. But for strong easterly wind anomalies, the frequency of the maximum easterly wind anomalies is similar for all conditions, which differs from the distribution of westerly wind anomalies. Overall, there are more strong westerly wind anomalies than strong easterly wind anomalies. That more strong westerly wind events occur during El Niño events that may be responsible for the asymmetry of El Niño and La Niña.

The strength of ENSO is analyzed with the eight ensemble members of SODA 2.2.6, and the results show that in different ensemble members ENSO has remarkably different strengths. By analyzing the 1918/1919 El Niño in ensemble members ENS05 and ENS07, we found that the different timing of WWB onset and the amplitude of WWB in ENS05 and ENS07 may be responsible for the different strengths of the 1918/1919 El Niño in different ensemble members. It also suggests the importance of high frequency wind stress in the development of ENSO.

Previous studies show that although the occurrence of ENSO is accurately predicted most ENSO prediction models are unable to predict the accurate amplitude of El Niño accurately. This study suggests that high frequency wind forcing is important to the development of ENSO, especially to the strength of El Niño. The CHI amplitude is plotted as a function of CHI longitude for warm events (Figure 38) in SODA 2.2.6. The figure shows that although El Niños cover a wide range of longitude strong El Niño only occurs in the eastern Pacific Ocean. Weak El Niños may relate to low frequency variability and are predictable in most of the models. It is possible that strong El Niños in the eastern tropical Pacific may be related to the occurrence of high frequency wind stress. On the other hand most of the models predict low frequency variability but not high frequency wind stress. One possibility is that El Niños in the prediction are weak. One way to improve ENSO amplitude prediction may require better the representation of high frequency wind stress.

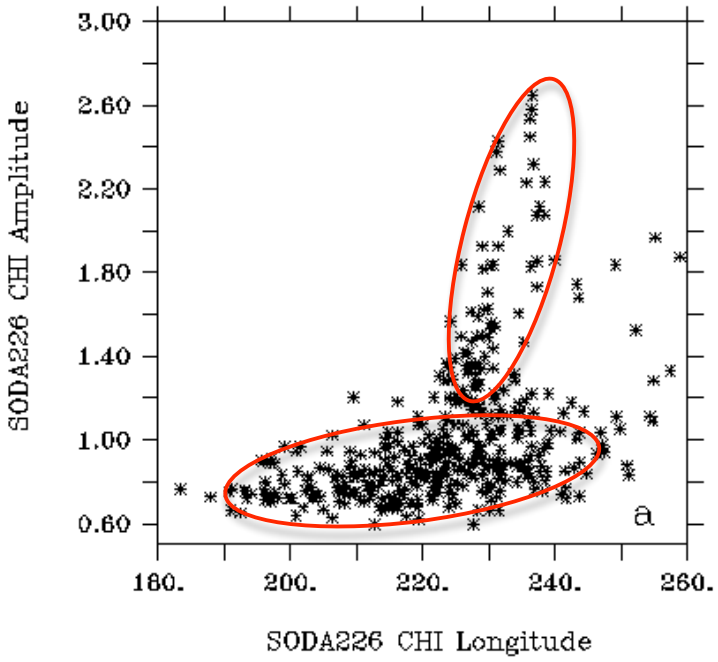

Figure 38. CHI amplitude in °C plotted as a function of CHI longitude in ° for warm event.

The background state of the tropical Pacific has significant impacts on ENSO variability. In order to explore the mechanisms responsible for ENSO variability in SODA 2.2.6, the role of ocean dynamics is investigated with a focus on long-term changes of STCs. STCs, which consist of subduction of sub-tropical water into the equatorial thermocline, equatorial upwelling, and surface Ekman return flow from the tropics to the subtropics, is an important factor in regulating tropical Pacific SST variability. We first examined the linear trends of tropical Pacific SST in SODA2.2.6 calculated with a least squares method using monthly averaged data from 1900 to 2008. There is a cooling trend over the central tropical Pacific of about -0.2°C century^{-1} and warming over the western tropical Pacific that is about 1.2°C century^{-1}. Similar to SST,

the subsurface also displays a cooling trend, of about -1.4°C century^{-1}, in the central and eastern tropical Pacific at a depth of 100m-150m, and a warming trend in the western tropical Pacific of 2.0°C century^{-1} at 150m. The consistency of ocean temperature trends between the surface and subsurface suggests a role of ocean dynamics in setting the pattern.

The linear trend of wind stress from 1900 to 2008 shows anomalously divergent winds over the cooling region with anomalous easterlies in the west and anomalous westerlies in the east. The easterly wind anomalies cause the equatorial thermocline to shoal in the central equatorial Pacific and to deepen the equatorial thermocline in the west. Vertical movement of the thermocline accounts for both the SST and subsurface temperature changes. Off the equator, both the northeast and southeast trades intensify west of 120°W. Such changes in the wind stress presumably can accelerate the STC, which transports cold sub-tropical thermocline water to the equatorial theremocline. The net transport by the STC in both hemispheres displays a pronounced upward trend over the past century with a convergence of transport that increased by about 8.7±0.73 Sv century^{-1}.

Our analysis suggests an increasing trend of the STC transport over the last hundred years. This increasing in the STC transport means that more cold thermocline water in the subtropics is advected to the equatorial thermocline, consistent with the cooling trend in the subsurface equatorial ocean. Cold anomalies in the equatorial thermocline can reach the surface through enhanced equatorial upwelling.

Recently the fifth phase of the Coupled Model Intercomparison Project (CMIP5) for IPCC the fifth Assessment Report (AR5) became available and an evaluation of the quality of CMIP5 simulations was conducted. Due to the importance of ENSO in global climate, the simulation of ENSO is an important criterion validating coupled models. The characteristics of El Niño and La Niña are analyzed in the CMIP5 models based on CHI metrics. Generally, the simulation of El Niño and La Niña is realistic in most of the CMIP5 models. The strength of El Niño and La Niña covers a large range within the CMIP5 models, and the location of El Niño and La Niña in most of the CMIP5 models extends too far to the west of the tropical Pacific. Compared to SODA 2.2.6, most of the CMIP5 models do not capture the warming anomaly along the coast of South America during warming events. However, the difference between the CMIP5 models and the ensemble ocean reanalysis is not significant.

The asymmetry of El Niño and La Niña is a prominent feature of ENSO in the observations. In SODA 2.2.6 the strength of El Niño is stronger than La Niña as in the observations. However, most of the CMIP5 models do not capture the asymmetry of El Niño and La Niña. One possible reason is the location of El Niño and La Niña extends too far west in the tropical Pacific Ocean due to the cold bias in most of the CMIP5 models. Another reason may be due to the low resolution of the CMIP5 models preventing high frequency wind stress from playing a role in the asymmetry of El Niño and La Niña. In coupled models the resolution, especially in the tropical Pacific, is low which may not allow accurate simulation of high frequency variability. Increasing the

resolution of the coupled models may help to improve the simulation of the asymmetry of El Niño and La Niña.

In the ensemble reanalysis, ENSO has prominent decadal variability and a weak long-term trend. For comparison, we analyzed long-term trends of ENSO in CMIP5 models. In SODA 2.2.6, the strength of El Niño does not change much, while the location of El Niño tends to move to the west in the tropical Pacific Ocean. In most of the CMIP5 models, both the strength and the location of El Niño have little change over the 20th century. The large ensemble spread in the CMIP5 models shows that in some of the ensemble members the strength of El Niño is increasing while in some other ensemble members is decreasing. Cold events in SODA 2.2.6 have little change in CHI amplitude while the CHI longitude moves to the west over the 20th Century similar to what happened with warm events. In most of the CMIP5 models, both the strength and the location of La Niña have little change, again similar to the behavior of El Niño events in the CMIP5 models.

In SODA 2.2.6, ocean dynamics play a significant role in regulating tropical Pacific climate. ENSO variability in SODA 2.2.6 and in the CMIP5 models is different and in order to test the robustness of the role of ocean dynamics we also analyzed long-term trends of tropical Pacific climate.

In most of the CMIP5 models tropical Pacific SST has a warming trend accompanied by a weakening of equatorial wind stress. The weakening wind stress reduces the slope of equatorial thermocline such that the depth of the equatorial thermocline is deeper in the eastern and shallower in the western tropical Pacific Ocean.

The subsurface in the eastern tropical Pacific Ocean warms while in the western tropical Pacific it cools. The cooling subsurface in the western tropical Pacific due to the shallowing of the thermocline could plausibly be accompanied by a cooling at the surface. However, in most of the CMIP5 models, there is warming in the western tropical Pacific Ocean. This likely comes from the decreasing of latent heat flux resulting from the weakening of wind speed.

In SODA 2.2.6, the strengthening of wind stress accelerates the STCs that brings more cold water from the deep ocean to cool the surface. The increasing transport of pycnocline water from the extra-tropics to the tropics results in a cooling of the subsurface in the central-eastern tropical Pacific Ocean. The variability of STCs in the CMIP5 models is also analyzed. In most of the CMIP5 models, the STC has been weakening consistent with the weakening of the equatorial wind stress. The weakening of the STC reduces the equatorial upwelling resulting in a warming surface and a decreasing pycnocline transport from the subtropics to the equatorial area results in a warm subsurface in the central-eastern tropical Pacific Ocean. The long-term change of tropical Pacific climate in SODA 2.2.6 and the CMIP5 models is different. However, the change of STCs is consistent with the change of tropical Pacific SST and the subsurface ocean. The role of ocean dynamics in regulating tropical Pacific climate is robust in both the ocean reanalysis and the CMIP5 coupled models.

ENSO variability and long-term changes of the background state in the tropical Pacific Ocean are analyzed in both the ensemble reanalysis and the CMIP5 models. In SODA 2.2.6, there is a cooling trend at the surface of the tropical Pacific, accompanied

by a weak change of El Niño. The location of El Niño moves slightly westward. In most of the CMIP5 models, there is a warming trend at the surface of the tropical Pacific, and there is a slight increase of El Niño strength and the location of El Niño does not change much.

Due to the lack of observations, previous studies focused on the short-term change in the STC and the long-term trend is little known. The long record of ocean reanalysis with the vertical structure gives us a general picture of the long-term change in the STC in the last century and the role of the STC in regulating tropical Pacific temperature. The results in the ocean reanalysis suggest the importance of the STC in tropical Pacific climate change in the last century.

The ocean reanalysis can also be used as a benchmark to validate coupled models. Since the CMIP5 models are going to be used for IPCC AR5, the evaluation of the CMIP5 models is necessary and urgent. The comparison of the ensemble reanalysis with the ensemble historical run of the CMIP5 models gives us the confidence to use the CMIP5 models to simulate the climate system especially ENSO. ENSO variability in the CMIP5 models gives us a general picture of how ENSO changed in the last century. The comparison of ENSO variability in the CMIP5 models and the ensemble reanalysis provides an evaluation of ENSO change in the CMIP5 models. The CMIP5 models are going to be used for the prediction of tropical Pacific climate especially for ENSO and these predictions are very important to economics, society and ecosystem due to the global impacts of ENSO. Our study provides certainty confidence to use the CMIP5 models to do climate predictions.

There are several new research topics suggested by this study. The long-term change of ENSO has been discussed in the context of SODA 2.2.6 and the CMIP5 models. Since the impact of ENSO is worldwide, the teleconnections of ENSO on global climate in the last century is an interesting topic to pursue. The long-term change of the STC has been discussed in both the ensemble reanalysis and the CMIP5 models, and only the effects of tropical regions are discussed. Sub-tropical subduction, one component of the STC, needs to be analyzed to explore the impacts of extra-tropics to tropics in the last century. The ability of the CMIP5 models to simulate the climate system has improved but there are still biases in the simulations. Improvements are still needed for coupled models to simulate climate systems. Also ENSO variability and the background state change in the tropical Pacific Ocean is different in the ensemble reanalysis and the CMIP5 models, and the reason for these differences needs to be investigated.

REFERENCES

An, S. I., and F. F. Jin (2004), Nonlinearity and asymmetry of ENSO, *Journal of Climate*, *17*(12), 2399-2412.

Barnston, A. G., Y. He, and M. H. Glantz (1999), Predictive skill of statistical and dynamical climate models in SST forecasts during the 1997—98 El Niño episode and the 1998 La Niña onset, *Bulletin of the American Meteorological Society*, *80*(2), 217-243.

Battisti, D. S., and A. C. Hirst (1989), Interannual variability in a tropical atmosphere–ocean model: Influence of the basic state, ocean geometry and nonlinearity, *Journal of the Atmospheric Sciences*, *46*(12), 1687-1712.

Bentsen, M., et al. (2012), The Norwegian Earth System Model, NorESM1-M – Part 1: Description and basic evaluation, *Geosci. Model Dev. Discuss.*, *5*(3), 2843-2931.

Bjerknes, J. (1969), Atmospheric teleconnections from the equatorial Pacific, *Monthly Weather Review*, *97*(3), 163-172.

Braconnot, P., F. Hourdin, S. Bony, J. Dufresne, J. Grandpeix, and O. Marti (2007), Impact of different convective cloud schemes on the simulation of the tropical seasonal cycle in a coupled ocean–atmosphere model, *Clim Dynam*, *29*(5), 501-520.

Burgers, G., and D. B. Stephenson (1999), The "normality" of El Niño, *Geophys Res Lett*, *26*(8), 1027-1030.

Cane, M. A., A. C. Clement, A. Kaplan, Y. Kushnir, D. Pozdnyakov, R. Seager, S. E. Zebiak, and R. Murtugudde (1997), Twentieth-century sea surface temperature trends, *Science*, *275*(5302), 957-960.

Capotondi, A., A. Wittenberg, and S. Masina (2006), Spatial and temporal structure of tropical Pacific interannual variability in 20th century coupled simulations, *Ocean Model*, *15*(3-4), 274-298.

Capotondi, A., M. A. Alexander, C. Deser, and M. J. McPhaden (2005), Anatomy and decadal evolution of the Pacific Sub-tropical-Tropical Cells (STCs), *Journal of Climate*, *18*(18), 3739-3758.

Carton, J. A., and B. S. Giese (2008), A reanalysis of ocean climate using Simple Ocean Data Assimilation (SODA), *Monthly Weather Review*, *136*(8), 2999-3017.

Carton, J. A., G. Chepurin, and X. H. Cao (2000a), A simple ocean data assimilation analysis of the global upper ocean 1950-95. Part II: Results, *J Phys Oceanogr*, *30*(2), 311-326.

Carton, J. A., G. Chepurin, X. H. Cao, and B. Giese (2000b), A simple ocean data assimilation analysis of the global upper ocean 1950-95. Part I: Methodology, *J Phys Oceanogr*, *30*(2), 294-309.

Chavez, F. P., M. Messié, and J. T. Pennington (2011), Marine primary production in relation to climate variability and change, *Annual Review of Marine Science*, *3*(1), 227-260.

Cheng, W., M. J. McPhaden, D. X. Zhang, and E. J. Metzger (2007), Recent changes in the Pacific sub-tropical cells inferred from an eddy-resolving ocean circulation model, *J Phys Oceanogr*, *37*(5), 1340-1356.

Clement, A. C., R. Seager, M. A. Cane, and S. E. Zebiak (1996), An ocean dynamical thermostat, *Journal of Climate*, *9*(9), 2190-2196.

Collins, M., el al. (2010), The impact of global warming on the tropical Pacific ocean and El Niño, *Nat Geosci*, *3*(6), 391-397.

Compo, G. P., J. S. Whitaker, and P. D. Sardeshmukh (2006), Feasibility of a 100-year reanalysis using only surface pressure data, *Bulletin of the American Meteorological Society*, *87*(2), 175.

Compo, G. P., et al. (2011), The twentieth century reanalysis project, *Quarterly Journal of the Royal Meteorological Society*, *137*(654), 1-28.

Deser, C., A. S. Phillips, and M. A. Alexander (2010), Twentieth century tropical sea surface temperature trends revisited, *Geophys. Res. Lett.*, *37*(10), L10701.

DiNezio, P., A. Clement, and G. Vecchi (2010), Reconciling differing views of tropical Pacific climate change, *Eos Trans. AGU*, *91*(16).

DiNezio, P. N., A. C. Clement, G. A. Vecchi, B. J. Soden, B. P. Kirtman, and S. K. Lee (2009), Climate response of the equatorial Pacific to global warming, *Journal of Climate*, *22*(18), 4873-4892.

Dong, B. W. (2005), Asymmetry between El Niño and La Niña in a global coupled GCM with an eddy-permitting ocean resolution, *Journal of Climate*, *18*(16), 3373-3387.

Epstein, E. S. (1969), Stochastic dynamic prediction1, *Tellus*, *21*(6), 739-759.

Fedorov, A. V. (2002), The response of the coupled tropical ocean-atmosphere to westerly wind bursts, *Quarterly Journal of the Royal Meteorological Society*, *128*(579), 1-23.

Fedorov, A. V., and S. G. Philander (2000), Is El Niño changing?, *Science*, *288*(5473), 1997-2002.

Fedorov, A. V., and S. G. Philander (2001), A stability analysis of tropical ocean-atmosphere interactions: Bridging measurements and theory for El Niño, *Journal of Climate*, *14*(14), 3086-3101.

Fedorov, A. V., S. L. Harper, S. G. Philander, B. Winter, and A. Wittenberg (2003), How predictable is El Niño?, *Bulletin of the American Meteorological Society*, *84*(7), 911.

Frauen, C., and D. Dommenget (2010), El Niño and La Niña amplitude asymmetry caused by atmospheric feedbacks, *Geophys Res Lett*, *37*.

Gebbie, G., I. Eisenman, A. Wittenberg, and E. Tziperman (2007), Modulation of westerly wind bursts by sea surface temperature: A semistochastic feedback for ENSO, *Journal of the Atmospheric Sciences*, *64*(9), 3281-3295.

Giese, B. S., and D. E. Harrison (1990), Aspects of the Kelvin wave response to episodic wind forcing, *J. Geophys. Res.*, *95*(C5), 7289-7312.

Giese, B. S., and S. Ray (2011), El Niño variability in simple ocean data assimilation (SODA), 1871-2008, *J. Geophys. Res.*, *116*(C2), C02024.

Giese, B. S., G. P. Compo, N. C. Slowey, P. D. Sardeshmukh, J. A. Carton, S. Ray, and J. S. Whitaker (2010), The 1918/19 El Niño, *Bulletin of the American Meteorological Society*, *91*(2), 177-183.

Graham, N. E., and W. B. White (1988), The El Niño cycle: A natural oscillator of the Pacific ocean—atmosphere system, *Science*, *240*(4857), 1293-1302.

Gu, D. F., and S. G. H. Philander (1997), Interdecadal climate fluctuations that depend on exchanges between the tropics and extratropics, *Science*, *275*(5301), 805-807.

Guilyardi, E. (2006), El Niño-mean state-seasonal cycle interactions in a multi-model ensemble, *Clim Dynam*, *26*(4), 329-348.

Guilyardi, E., A. Wittenberg, A. Fedorov, M. Collins, C. Z. Wang, A. Capotondi, G. J. van Oldenborgh, and T. Stockdale (2009), Understanding El Niño in ocean-atmosphere general circulation models progress and challenges, *Bulletin of the American Meteorological Society*, *90*(3), 325.

Guilyardi, E., S. Gualdi, J. Slingo, A. Navarra, P. Delecluse, J. Cole, G. Madec, M. Roberts, M. Latif, and L. Terray (2004), Representing El Niño in coupled ocean–atmosphere GCMs: The dominant role of the atmospheric component, *Journal of Climate*, *17*(24), 4623-4629.

Hannachi, A., D. B. Stephenson, and K. R. Sperber (2003), Probability-based methods for quantifying nonlinearity in the ENSO, *Clim Dynam*, *20*(2-3), 241-256.

Held, I. M., and B. J. Soden (2006), Robust responses of the hydrological cycle to global warming, *Journal of Climate*, *19*(21), 5686-5699.

Hoerling, M. P., A. Kumar, and M. Zhong (1997), El Niño, La Niña, and the nonlinearity of their teleconnections, *Journal of Climate*, *10*(8), 1769-1786.

Horel, J. D., and J. M. Wallace (1981), Planetary-scale atmospheric phenomena associated with the southern oscillation, *Monthly Weather Review*, *109*(4), 813-829.

Jin, F.-F. (1997), An equatorial ocean recharge paradigm for ENSO. Part I: Conceptual model, *Journal of the Atmospheric Sciences*, *54*(7), 811-829.

Jin, F.-F., J. D. Neelin, and M. Ghil (1994), El Niño on the devil's staircase: Annual subharmonic steps to chaos, *Science*, *264*(5155), 70-72.

Jin, F. F., S. I. An, A. Timmermann, and J. X. Zhao (2003), Strong El Niño events and nonlinear dynamical heating, *Geophys Res Lett*, *30*(3).

Jones, P. W. (1999), First- and second-order conservative remapping schemes for grids in spherical coordinates, *Monthly Weather Review*, *127*(9), 2204-2210.

Kang, I. S., and J. S. Kug (2002), El Niño and La Niña sea surface temperature anomalies: Asymmetry characteristics associated with their wind stress anomalies, *J Geophys Res-Atmos*, *107*(D19).

Kaplan, A., M. A. Cane, Y. Kushnir, A. C. Clement, M. B. Blumenthal, and B. Rajagopalan (1998), Analyses of global sea surface temperature 1856-1991, *J Geophys Res-Oceans*, *103*(C9), 18567-18589.

Karnauskas, K. B., R. Seager, A. Kaplan, Y. Kushnir, and M. A. Cane (2009), Observed strengthening of the zonal sea surface temperature gradient across the equatorial Pacific Ocean, *Journal of Climate*, *22*(16), 4316-4321.

Kessler, W. S. (2002), Is ENSO a cycle or a series of events?, *Geophys Res Lett*, *29*(23).

Kleeman, R., J. P. McCreary, and B. A. Klinger (1999), A mechanism for generating ENSO decadal variability, *Geophys Res Lett*, *26*(12), 1743-1746.

Knutson, T. R., and S. Manabe (1995), Time-mean response over the tropical Pacific to increased CO_2 in a coupled ocean-atmosphere model, *Journal of Climate*, *8*(9), 2181-2199.

Landsea, C. W., and J. A. Knaff (2000), How much skill was there in forecasting the very strong 1997–98 El Niño?, *Bulletin of the American Meteorological Society*, *81*(9), 2107-2119.

Latif, M., and N. S. Keenlyside (2009), El Niño/Southern Oscillation response to global warming, *P Natl Acad Sci USA*, *106*(49), 20578-20583.

Latif, M., et al. (2001), ENSIP: the El Niño simulation intercomparison project, *Clim Dynam*, *18*(3-4), 255-276.

Lee, T., and I. Fukumori (2003), Interannual-to-decadal variations of tropical-sub-tropical exchange in the Pacific Ocean: Boundary versus interior pycnocline transports, *Journal of Climate*, *16*(24), 4022-4042.

Lengaigne, M., E. Guilyardi, J. P. Boulanger, C. Menkes, P. Delecluse, P. Inness, J. Cole, and J. Slingo (2004), Triggering of El Niño by westerly wind events in a coupled general circulation model, *Clim Dynam*, *23*(6), 601-620.

Liu, Z., S. Vavrus, F. He, N. Wen, and Y. Zhong (2005), Rethinking tropical ocean response to global warming: The enhanced equatorial warming, *Journal of Climate*, *18*(22), 4684-4700.

Lloyd, J., E. Guilyardi, H. Weller, and J. Slingo (2009), The role of atmosphere feedbacks during ENSO in the CMIP3 models, *Atmos Sci Lett*, *10*(3), 170-176.

Lohmann, K., and M. Latif (2005), Tropical Pacific decadal variability and the sub-tropical-tropical cells, *Journal of Climate*, *18*(23), 5163-5178.

Matei, D., N. Keenlyside, M. Latif, and J. Jungclaus (2008), Sub-tropical forcing of tropical Pacific climate and decadal ENSO modulation, *Journal of Climate*, *21*(18), 4691-4709.

Mccreary, J. P., and P. Lu (1994), Interaction between the sub-tropical and equatorial ocean circulations - the sub-tropical cell, *J Phys Oceanogr*, *24*(2), 466-497.

McPhaden, M. J., and D. X. Zhang (2002), Slowdown of the meridional overturning circulation in the upper Pacific Ocean, *Nature*, *415*(6872), 603-608.

McPhaden, M. J., and D. X. Zhang (2004), Pacific Ocean circulation rebounds, *Geophys Res Lett*, *31*(18).

McPhaden, M. J., and X. B. Zhang (2009), Asymmetry in zonal phase propagation of ENSO sea surface temperature anomalies, *Geophys Res Lett*, *36*.

Meehl, G. A., G. J. Boer, C. Covey, M. Latif, and R. J. Stouffer (1997), Intercomparison makes for a better climate model, *Eos Trans. AGU*, *78*(41), 445-451.

Meehl, G. A., G. J. Boer, C. Covey, M. Latif, and R. J. Stouffer (2000), The Coupled Model Intercomparison Project (CMIP), *Bulletin of the American Meteorological Society*, *81*(2), 313-318.

Meehl, G. A., C. Covey, B. McAvaney, M. Latif, and R. J. Stouffer (2005), Overview of the coupled model intercomparison project, *Bulletin of the American Meteorological Society*, *86*(1), 89-93.

Meehl, G. A., K. Covey, T. Delworth, M. Latif, B. McAvaney, J. F. B. Mitchell, R. J. Stouffer, and K. Taylor (2007), The WCRP CMIP3 multimodel dataset: A new era in climate change research, *Bulletin of the American Meteorological Society*, *7*, 1383–1394.

Merryfield, W. J. (2006), Changes to ENSO under CO_2 doubling in a multimodel ensemble, *Journal of Climate*, *19*(16), 4009-4027.

Merryfield, W. J., and G. J. Boer (2005), Variability of upper Pacific Ocean overturning in a coupled climate model, *Journal of Climate*, *18*(5), 666-683.

Monahan, A. H., and A. Dai (2004), Spatial and temporal structure of ENSO nonlinearity, *Journal of Climate*, *17*(15), 3026-3036.

Neelin, J. D., M. Latif, and F. F. Jin (1994), Dynamics of coupled ocean-atmosphere models - the tropical problem, *Annu Rev Fluid Mech*, *26*, 617-659.

Okumura, Y. M., and C. Deser (2010), Asymmetry in the duration of El Niño and La Niña, *Journal of Climate*, *23*(21), 5826-5843.

Okumura, Y. M., M. Ohba, C. Deser, and H. Ueda (2011), A proposed mechanism for the asymmetric duration of El Niño and La Niña, *Journal of Climate*, *24*(15), 3822-3829.

Philip, S., and G. J. Van Oldenborgh (2006), Shifts in ENSO coupling processes under global warming, *Geophys Res Lett*, *33*(11).

Picaut, J., F. Masia, and Y. du Penhoat (1997), An advective-reflective conceptual model for the oscillatory nature of the ENSO, *Science*, *277*(5326), 663-666.

Raddatz, T. J., C. H. Reick, W. Knorr, J. Kattge, E. Roeckner, R. Schnur, K. G. Schnitzler, P. Wetzel, and J. Jungclaus (2007), Will the tropical land biosphere dominate the climate–carbon cycle feedback during the twenty-first century?, *Clim Dynam*, *29*(6), 565-574.

Randall, D. A., and Coauthors (2007), Climate models and their evaluation, *Climate Change 2007: The physical Science Basis,* S. Solomon et al., Eds., Cambridge Univeristy Press, 591-648.

Ray, S. and B. S. Giese (2012), Historical changes in El Niño and La Niña characteristics in an ocean reanalysis, *J Geophys Res-Ocean, Sumitted.*

Rayner, N. A., D. E. Parker, E. B. Horton, C. K. Folland, L. V. Alexander, D. P. Rowell, E. C. Kent, and A. Kaplan (2003), Global analyses of sea surface temperature, sea ice, and night marine air temperature since the late nineteenth century, *J Geophys Res-Atmos*, *108*(D14).

Rotstayn, L. D., M. A. Collier, M. R. Dix, Y. Feng, H. B. Gordon, S. P. O'Farrell, I. N. Smith, and J. Syktus (2010), Improved simulation of Australian climate and ENSO-related rainfall variability in a global climate model with an interactive aerosol treatment, *International Journal of Climatology*, *30*(7), 1067-1088.

Saravanan, R., and P. Chang (2000), Interaction between tropical Atlantic variability and El Niño-Southern Oscillation, *Journal of Climate*, *13*(13), 2177-2194.

Schneider, N., A. J. Miller, M. A. Alexander, and C. Deser (1999), Subduction of decadal North Pacific temperature anomalies: Observations and dynamics, *J Phys Oceanogr*, *29*(5), 1056-1070.

Schott, F. A., W. Q. Wang, and D. Stammer (2007), Variability of Pacific sub-tropical cells in the 50-year ECCO assimilation, *Geophys Res Lett*, *34*(5).

Schott, F. A., L. Stramma, W. Wang, B. S. Giese, and R. Zantopp (2008), Pacific sub-tropical cell variability in the SODA 2.0.2/3 assimilation, *Geophys Res Lett*, *35*(10).

Schubert, S. D., M. J. Suarez, P. J. Pegion, R. D. Koster, and J. T. Bacmeister (2004), On the cause of the 1930s dust bowl, *Science*, *303*(5665), 1855-1859.

Seager, R., and R. Murtugudde (1997), Ocean dynamics, thermocline adjustment, and regulation of tropical SST, *Journal of Climate*, *10*(3), 521-534.

Seager, R., Y. Kushnir, C. Herweijer, N. Naik, and J. Velez (2005), Modeling of tropical forcing of persistent droughts and pluvials over western North America: 1856–2000, *Journal of Climate*, *18*(19), 4065-4088.

Smith, D. M., R. Eade, N. J. Dunstone, D. Fereday, J. M. Murphy, H. Pohlmann, and A. A. Scaife (2010), Skilful multi-year predictions of Atlantic hurricane frequency, *Nature Geosci*, *3*(12), 846-849.

Smith, R. D., J. K. Dukowicz, and R. C. Malone (1992), Parallel ocean general-circulation modeling, *Physica D*, *60*(1-4), 38-61.

Sun, D.-Z., Y. Yu, and T. Zhang (2009), Tropical water vapor and cloud feedbacks in climate models: A further assessment using coupled simulations, *Journal of Climate*, *22*(5), 1287-1304.

Taylor, K. E., R. J. Stouffer, and G. A. Meehl (2011), An overview of CMIP5 and the experiment Design, *Bulletin of the American Meteorological Society*, *93*(4), 485-498.

Tziperman, E., L. Stone, M. A. Cane, and H. Jarosh (1994), El Niño chaos: Overlapping of resonances between the seasonal cycle and the Pacific ocean-atmosphere oscillator, *Science*, *264*(5155), 72-74.

van Oldenborgh, G. J., S. Y. Philip, and M. Collins (2005), El Niño in a changing climate: a multi-model study, *Ocean Science*, *1*, 81-95.

Vecchi, G. A., and B. J. Soden (2007a), Effect of remote sea surface temperature change on tropical cyclone potential intensity, *Nature*, *450*(7172), 1066-1070.

Vecchi, G. A., and B. J. Soden (2007b), Global warming and the weakening of the tropical circulation, *Journal of Climate*, *20*(17), 4316-4340.

Vecchi, G. A., and A. T. Wittenberg (2010), El Niño and our future climate: where do we stand?, *Wires Clim Change*, *1*(2), 260-270.

Vecchi, G. A., A. Clement, and B. J. Soden (2008), Examining the tropical Pacific's response to global warming, *Eos Trans. AGU*, *89*(9).

Vecchi, G. A., B. J. Soden, A. T. Wittenberg, I. M. Held, A. Leetmaa, and M. J. Harrison (2006), Weakening of tropical Pacific atmospheric circulation due to anthropogenic forcing, *Nature*, *441*(7089), 73-76.

Walker, G. T. (1923, 1924), Correlation in seasonal variations of weather, VIII : a preliminary study of world weather, Meteorological Office, Poona.

Walker, G. T., and E. W. Bliss (1932), World weather V, Edward Stanford, London.

Wallace, J. M., and D. S. Gutzler (1981), Teleconnections in the geopotential height field during the Northern Hemisphere winter, *Monthly Weather Review*, *109*(4), 784-812.

Wang, D. W., and M. A. Cane (2011), Pacific shallow meridional overturning circulation in a warming climate, *Journal of Climate*, *24*(24), 6424-6439.

Watanabe, S., et al. (2011), MIROC-ESM 2010: model description and basic results of CMIP5-20c3m experiments, *Geosci. Model Dev.*, *4*(4), 845-872.

Whitaker, J. S., and T. M. Hamill (2002), Ensemble data assimilation without perturbed observations, *Monthly Weather Review*, *130*(7), 1913-1924.

Whitaker, J. S., G. P. Compo, X. Wei, and T. M. Hamill (2004), Reanalysis without radiosondes using ensemble data assimilation, *Monthly Weather Review*, *132*(5), 1190-1200.

Wu, T., et al. (2012), The 20th century global carbon cycle from the Beijing Climate Center Climate System Model (BCC-CSM), *Clim Dynam, Submitted.*

Yukimoto, S., et al. (2011), Meteorological research institute-earth system model version 1 (MRI-ESM1) - model description, *64,* 83pp.

Zavala-Garay, J., C. Zhang, A. M. Moore, A. T. Wittenberg, M. J. Harrison, A. Rosati, J. Vialard, and R. Kleeman (2008), Sensitivity of hybrid ENSO models to unresolved atmospheric variability, *Journal of Climate*, *21*(15), 3704-3721.

Zelle, H., G. J. Van Oldenborgh, G. Burgers, and H. Dijkstra (2005), El Niño and Greenhouse warming: Results from ensemble simulations with the NCAR CCSM, *Journal of Climate*, *18*(22), 4669-4683.

Zhang, D. X., and M. J. McPhaden (2006), Decadal variability of the shallow Pacific meridional overturning circulation: Relation to tropical sea surface temperatures in observations and climate change models, *Ocean Model*, *15*(3-4), 250-273.

Zhang, W., J. Li, and X. Zhao (2010), Sea surface temperature cooling mode in the Pacific cold tongue, *J. Geophys. Res.*, *115*(C12), C12042.

APPENDIX

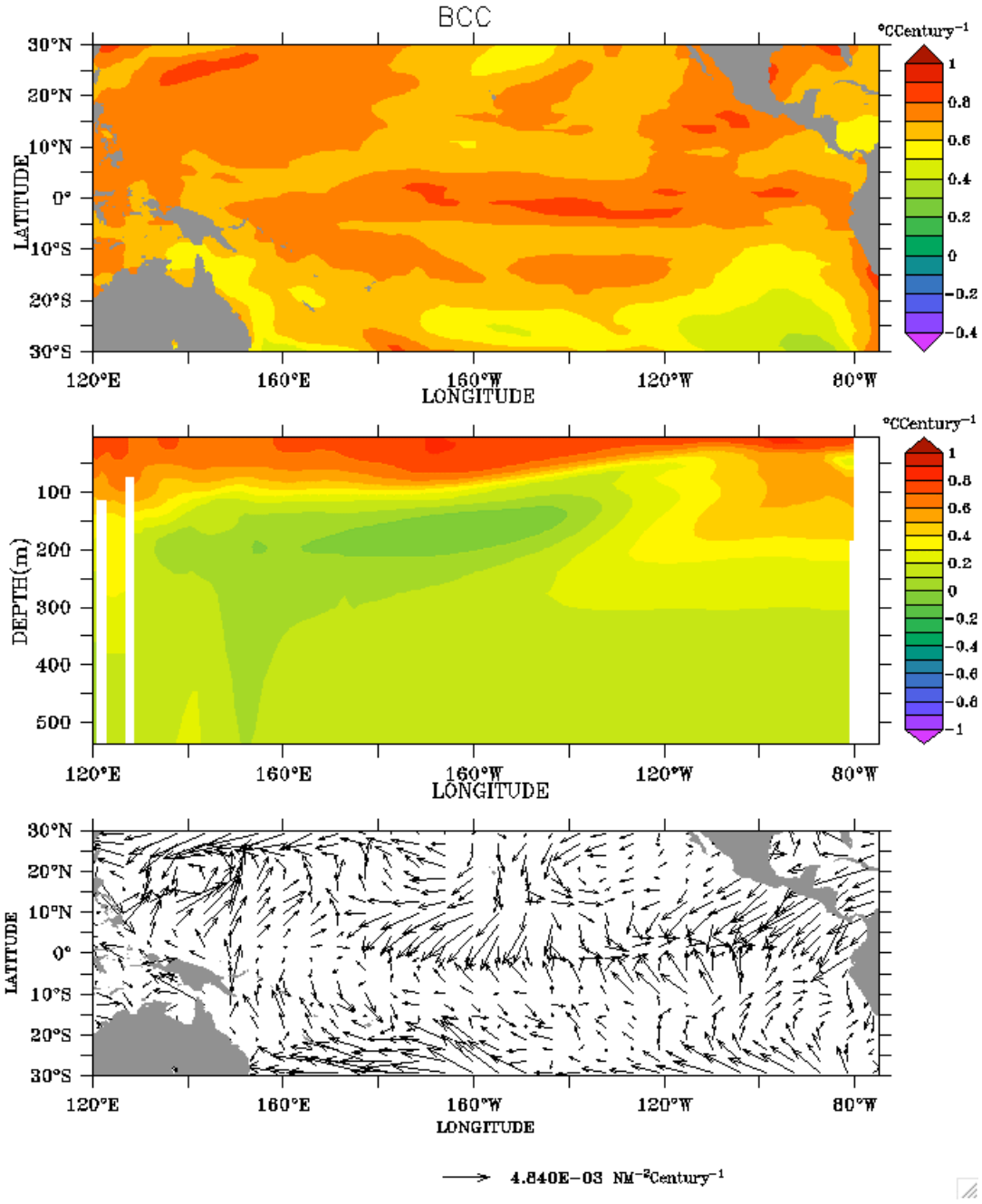

Figure A1. Linear trends in BCC model from 1900 to 2005 of (a) sea surface temperature, (b) temperature as a function of depth on the equator and (c) vectors of zonal and meridional wind stress.

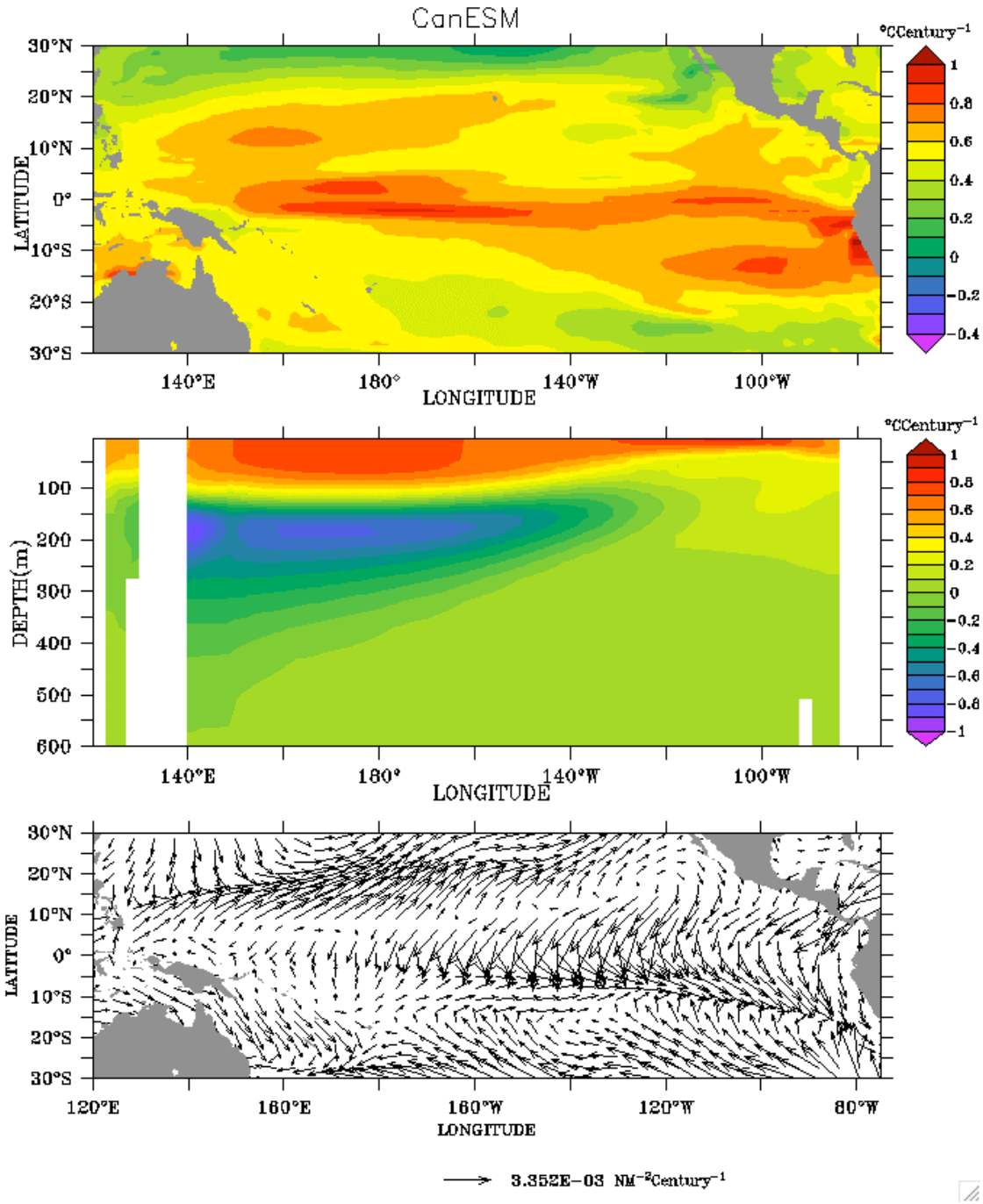

Figure A2. Linear trends in CanESM model from 1900 to 2005 of (a) sea surface temperature, (b) temperature as a function of depth on the equator and (c) vectors of zonal and meridional wind stress.

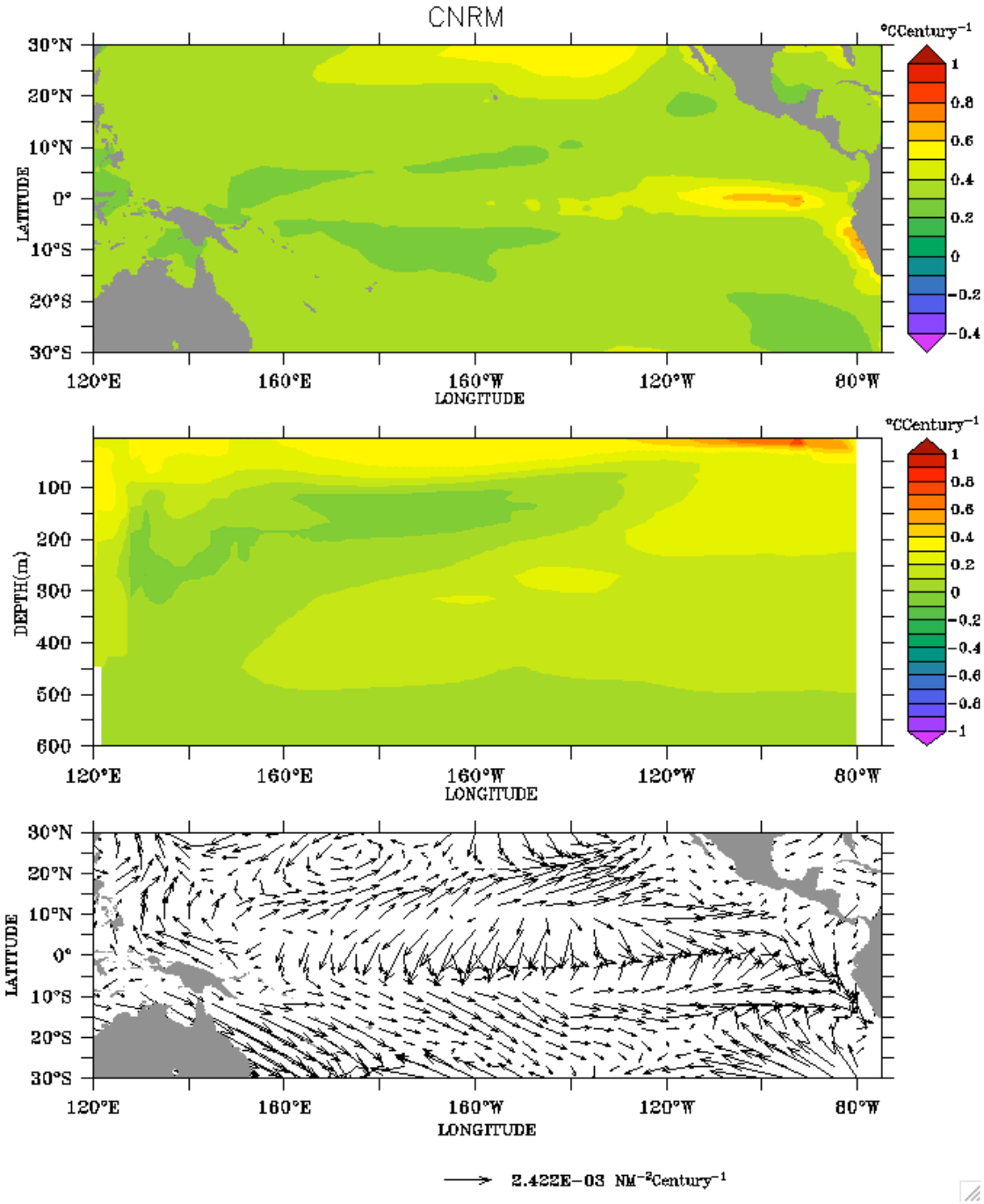

Figure A3. Linear trends in CNRM model from 1900 to 2005 of (a) sea surface temperature, (b) temperature as a function of depth on the equator and (c) vectors of zonal and meridional wind stress.

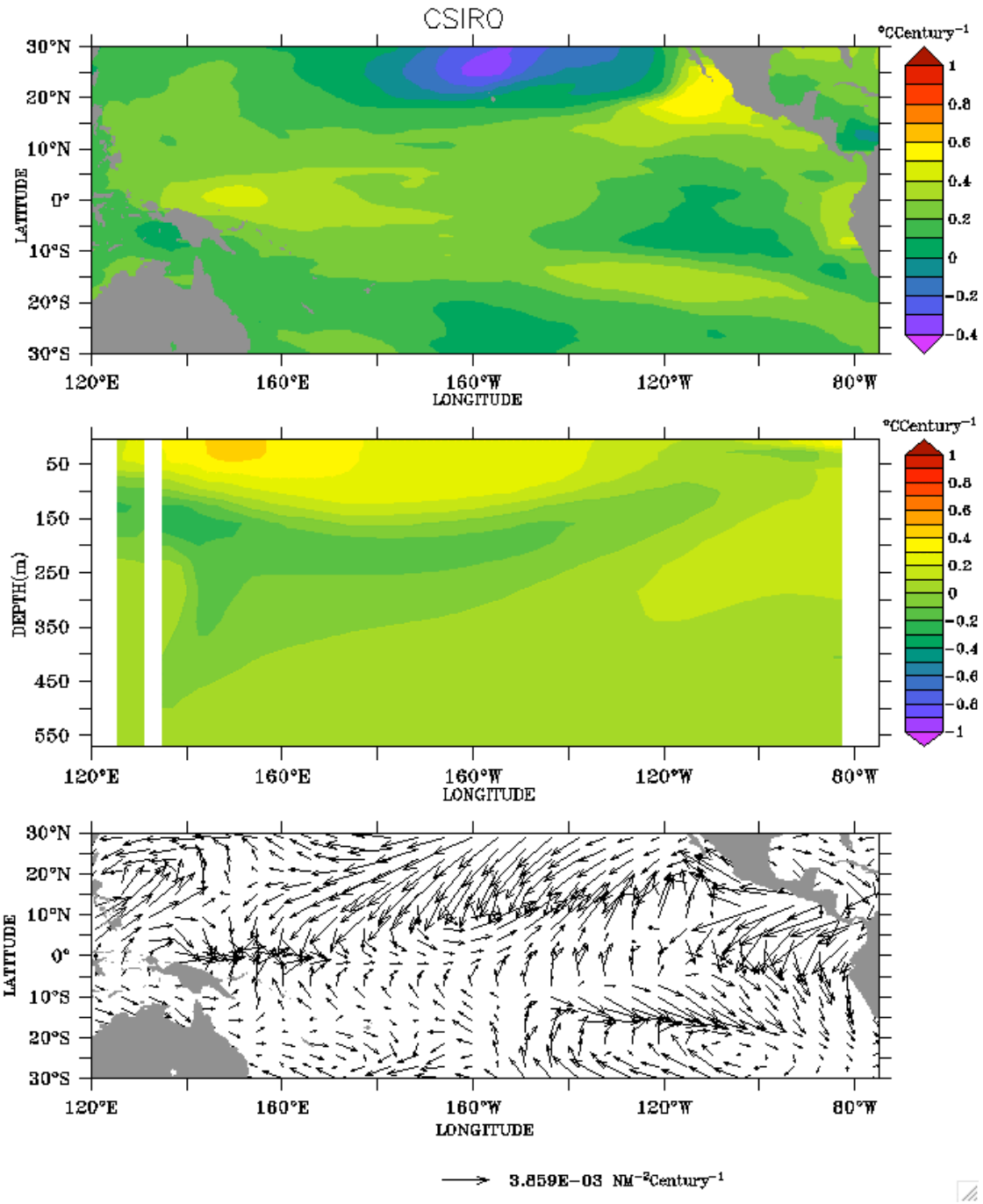

Figure A4. Linear trends in CSIRO model from 1900 to 2005 of (a) sea surface temperature, (b) temperature as a function of depth on the equator and (c) vectors of zonal and meridional wind stress.

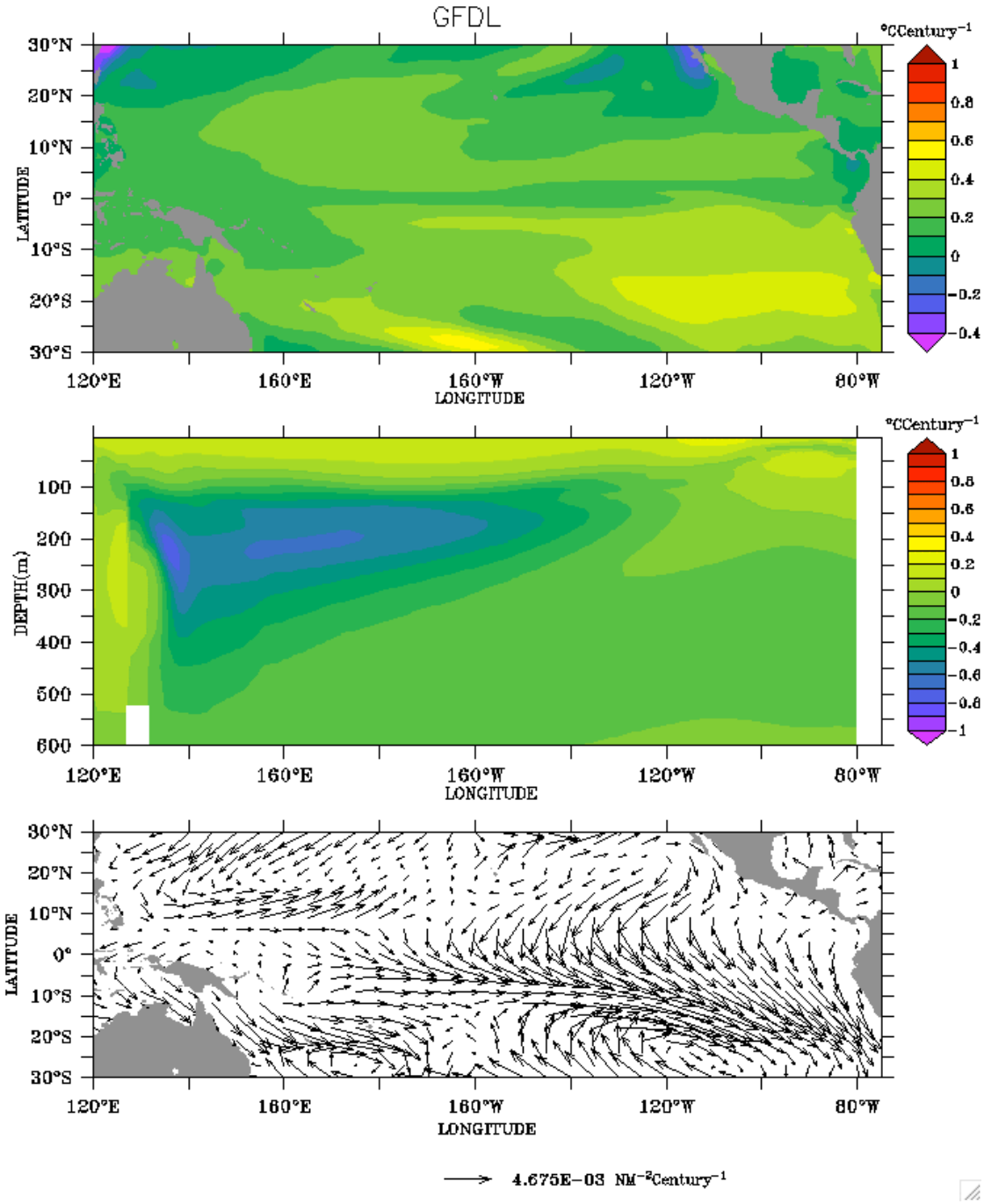

Figure A5. Linear trends in GFDL model from 1900 to 2005 of (a) sea surface temperature, (b) temperature as a function of depth on the equator and (c) vectors of zonal and meridional wind stress.

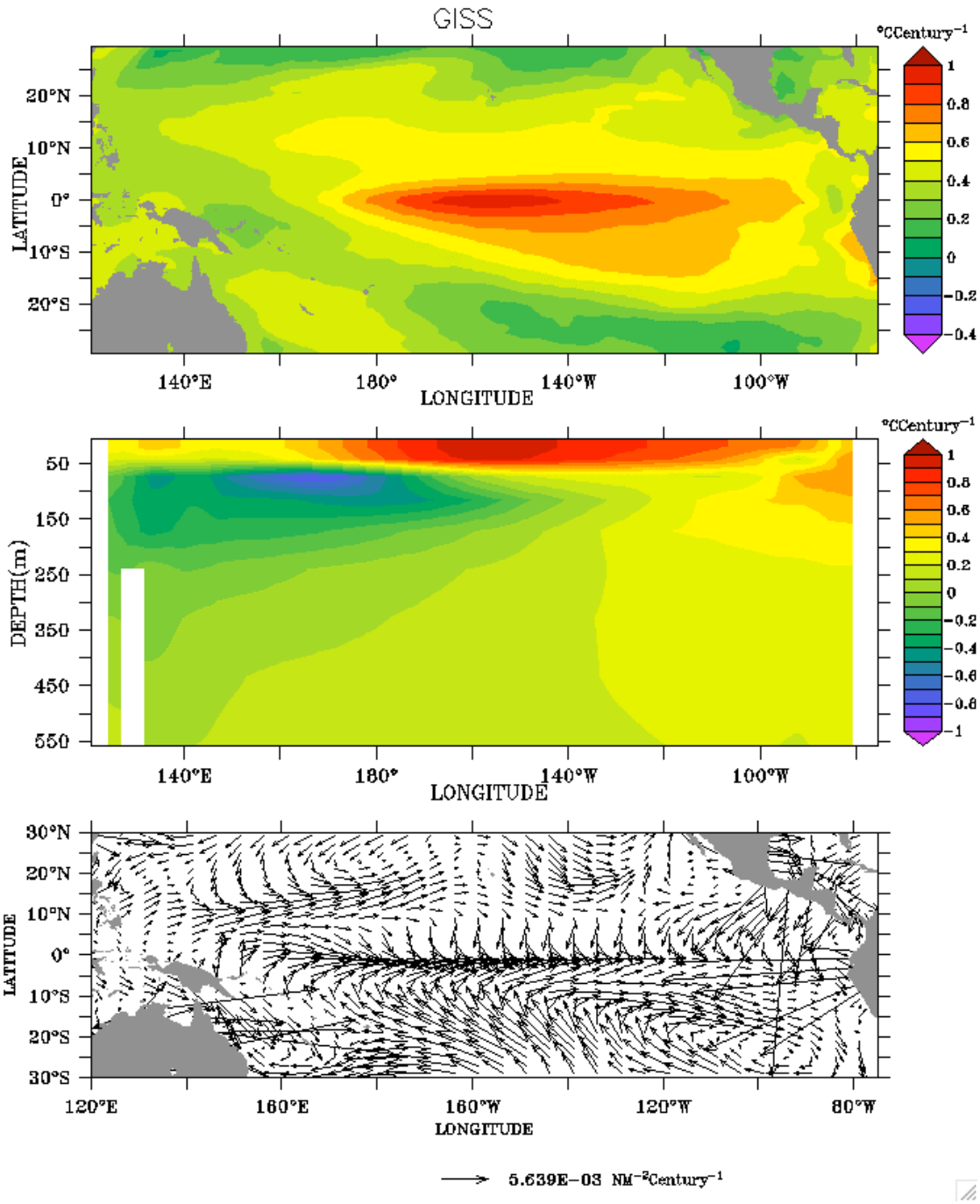

Figure A6. Linear trends in GISS model from 1900 to 2005 of (a) sea surface temperature, (b) temperature as a function of depth on the equator and (c) vectors of zonal and meridional wind stress.

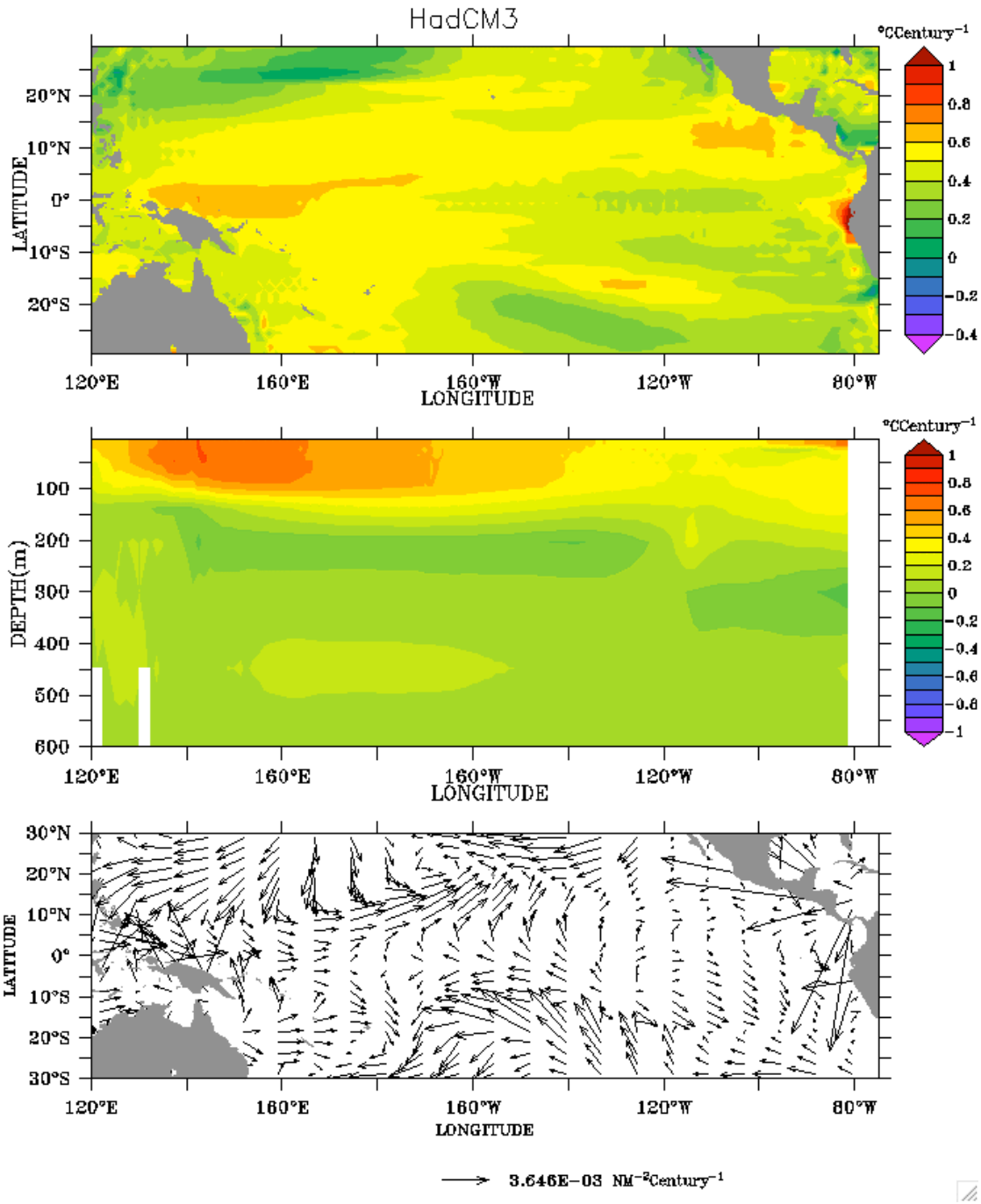

Figure A7. Linear trends in HadCM3 model from 1900 to 2005 of (a) sea surface temperature, (b) temperature as a function of depth on the equator and (c) vectors of zonal and meridional wind stress.

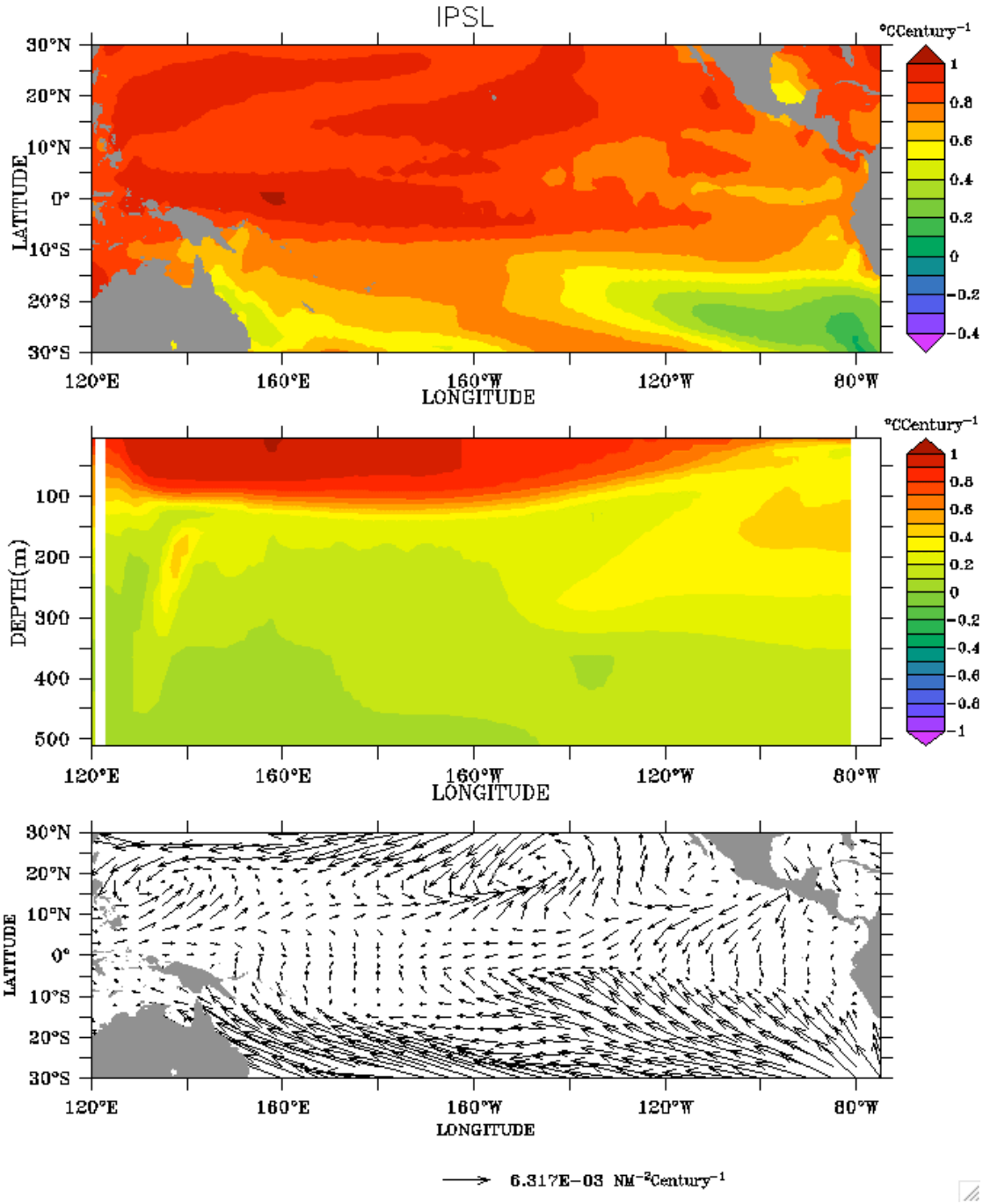

Figure A8. Linear trends in IPSL model from 1900 to 2005 of (a) sea surface temperature, (b) temperature as a function of depth on the equator and (c) vectors of zonal and meridional wind stress.

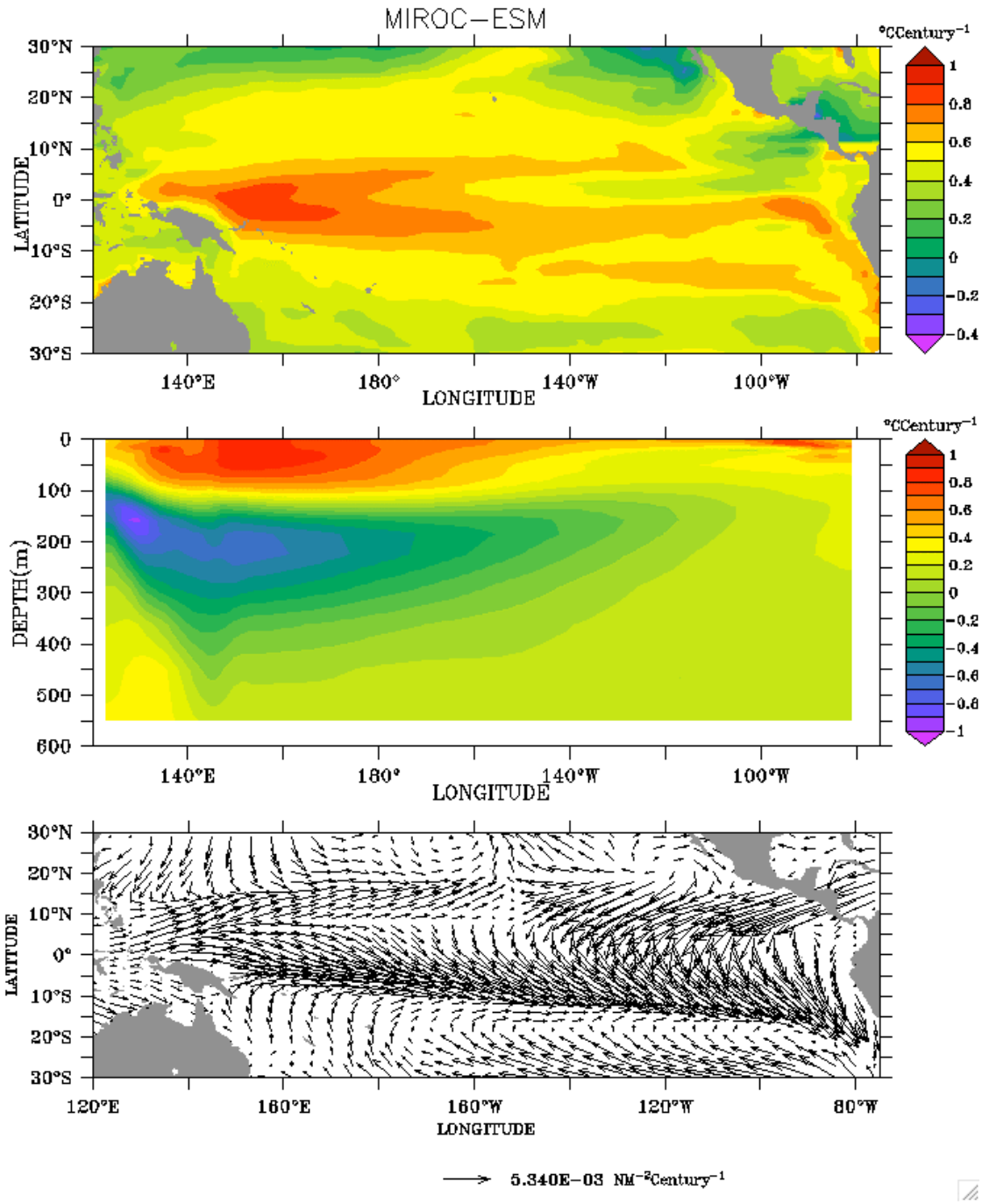

Figure A9. Linear trends in MIROC-ESM model from 1900 to 2005 of (a) sea surface temperature, (b) temperature as a function of depth on the equator and (c) vectors of zonal and meridional wind stress.

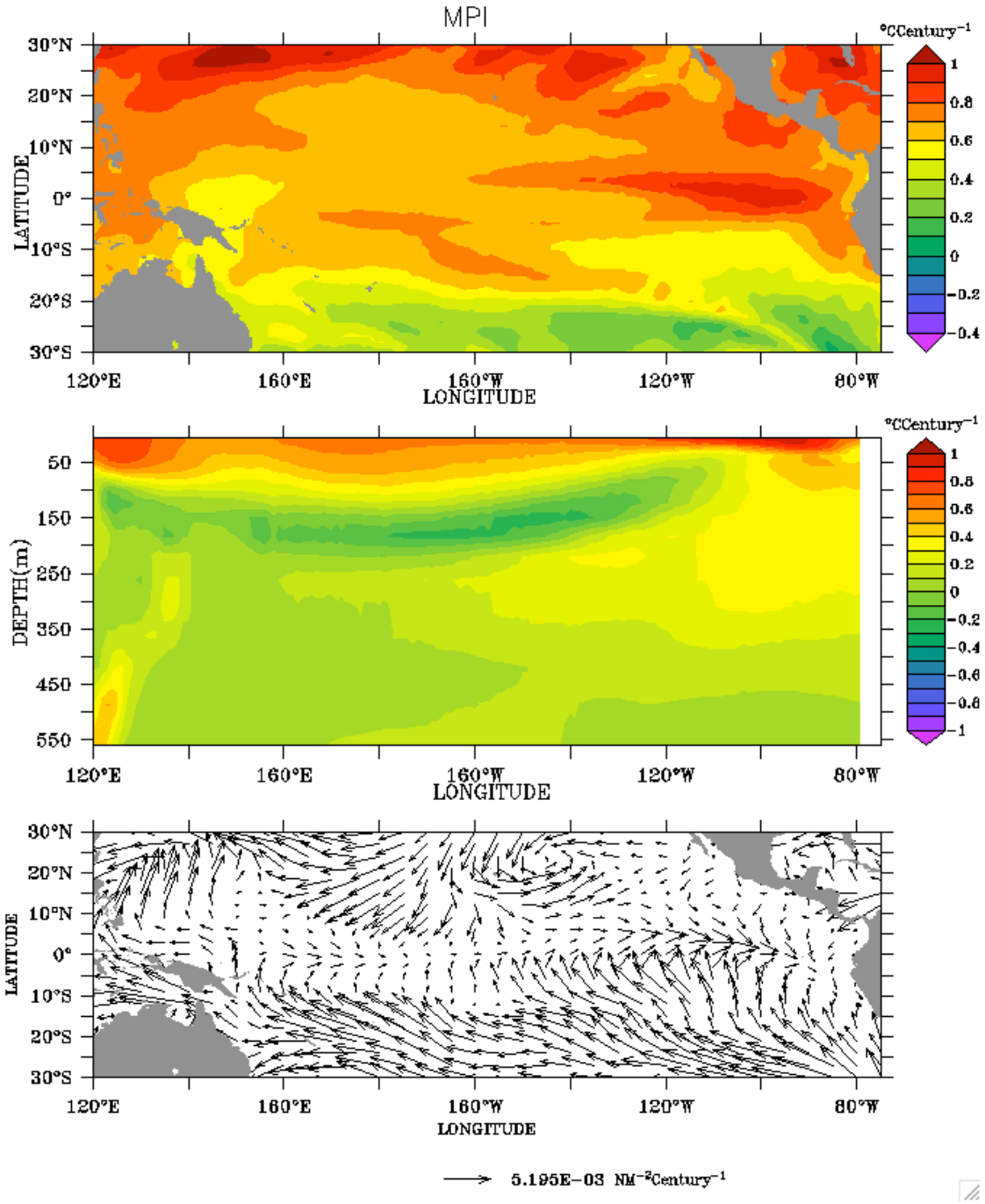

Figure A10. Linear trends in MPI model from 1900 to 2005 of (a) sea surface temperature, (b) temperature as a function of depth on the equator and (c) vectors of zonal and meridional wind stress.

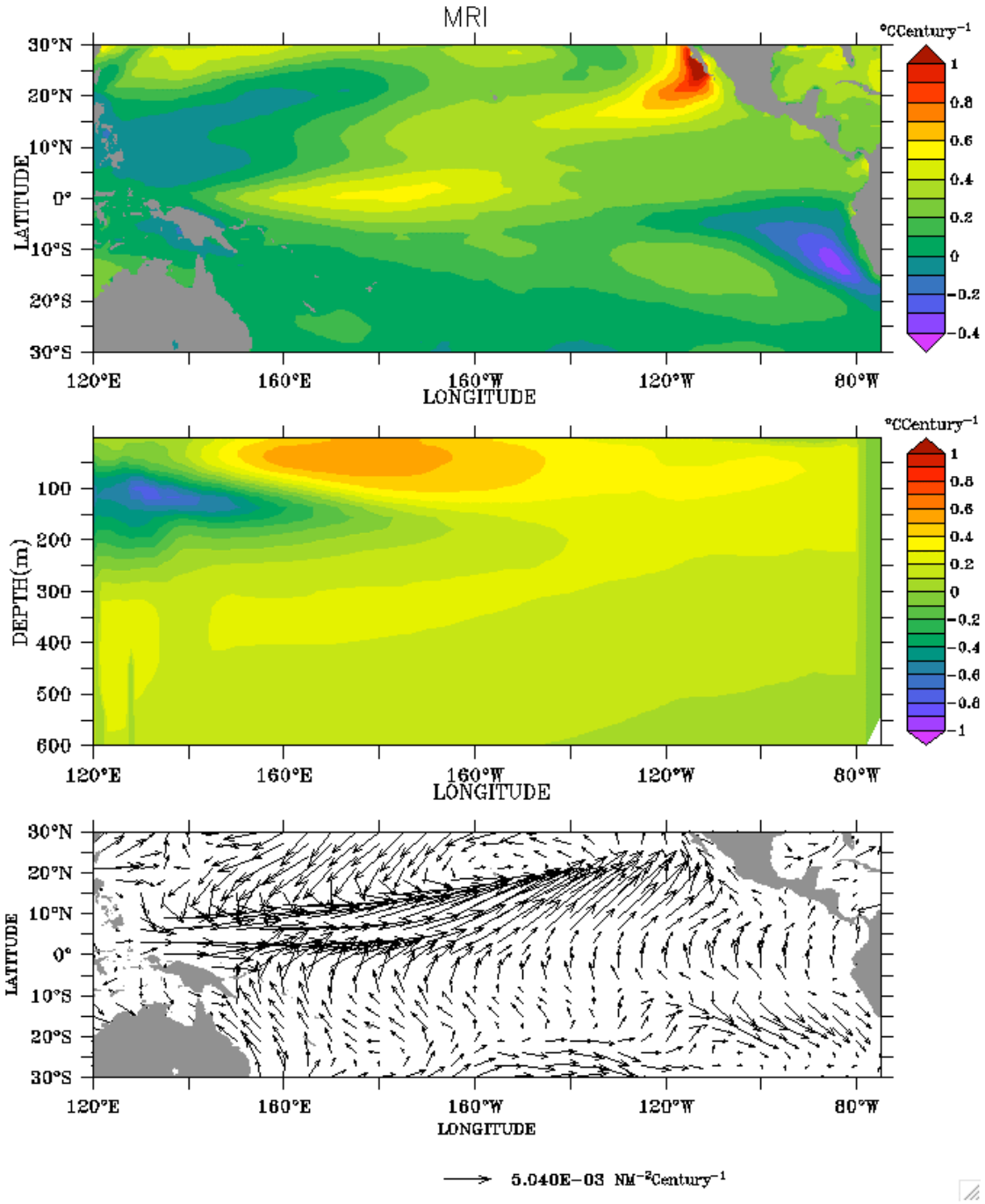

Figure A11. Linear trends in MRI model from 1900 to 2005 of (a) sea surface temperature, (b) temperature as a function of depth on the equator and (c) vectors of zonal and meridional wind stress.

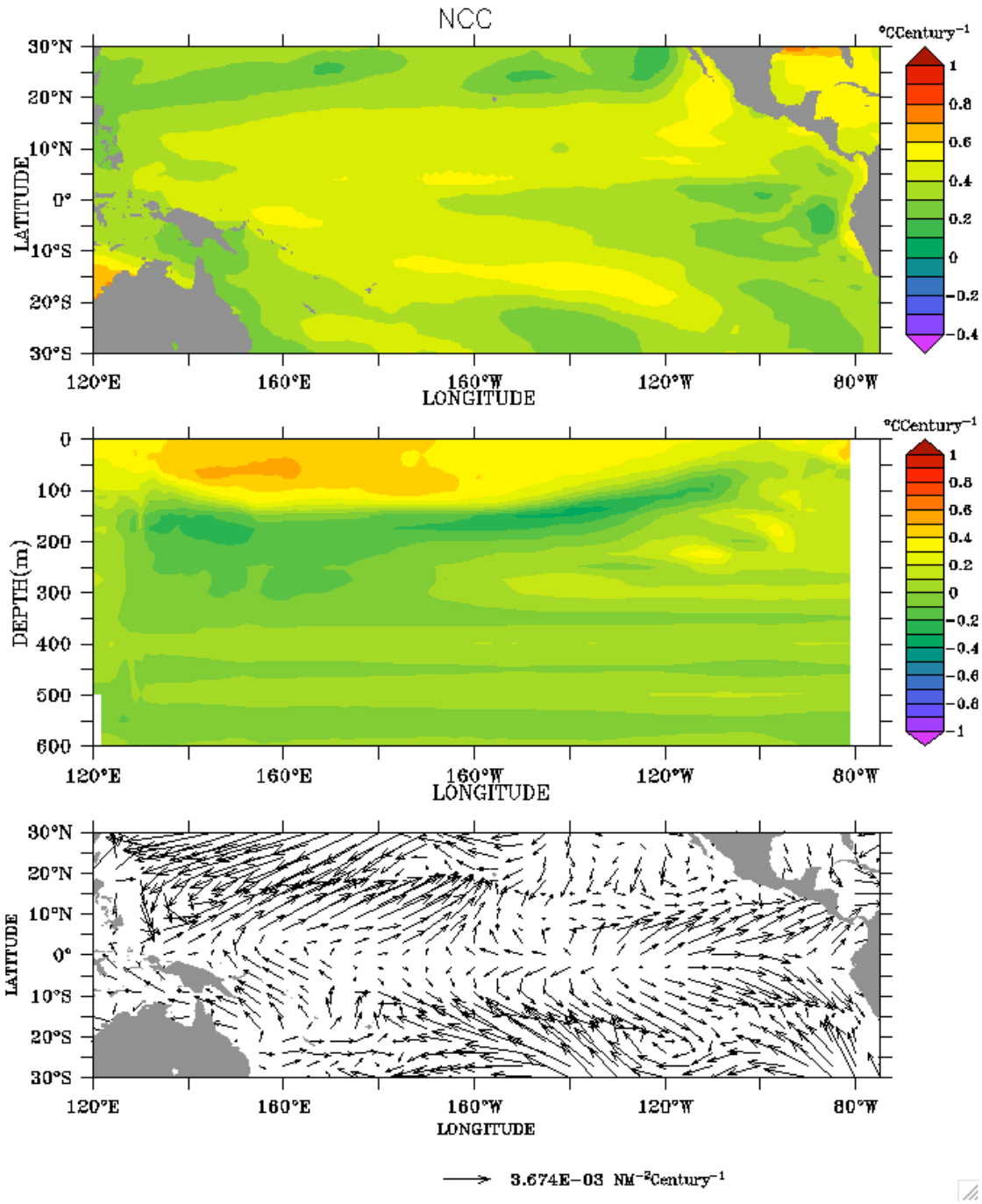

Figure A12. Linear trends in NCC model from 1900 to 2005 of (a) sea surface temperature, (b) temperature as a function of depth on the equator and (c) vectors of zonal and meridional wind stress.

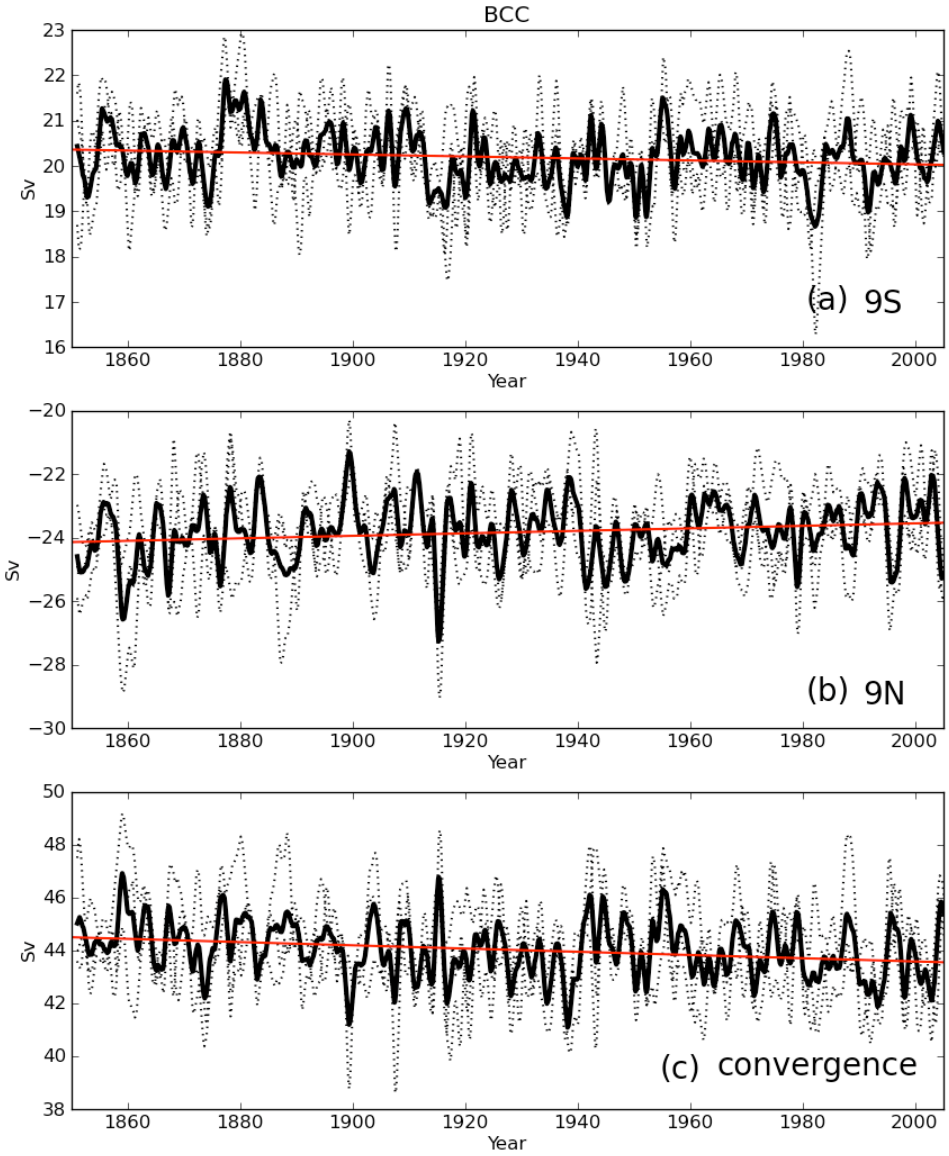

Figure A13. Transport of the STC in BCC model at (a) 9°S, (b) 9°N, and (c) convergence transport between 9°S and 9°N. Dashed lines are for each ensemble members, and thick black is the ensemble mean.

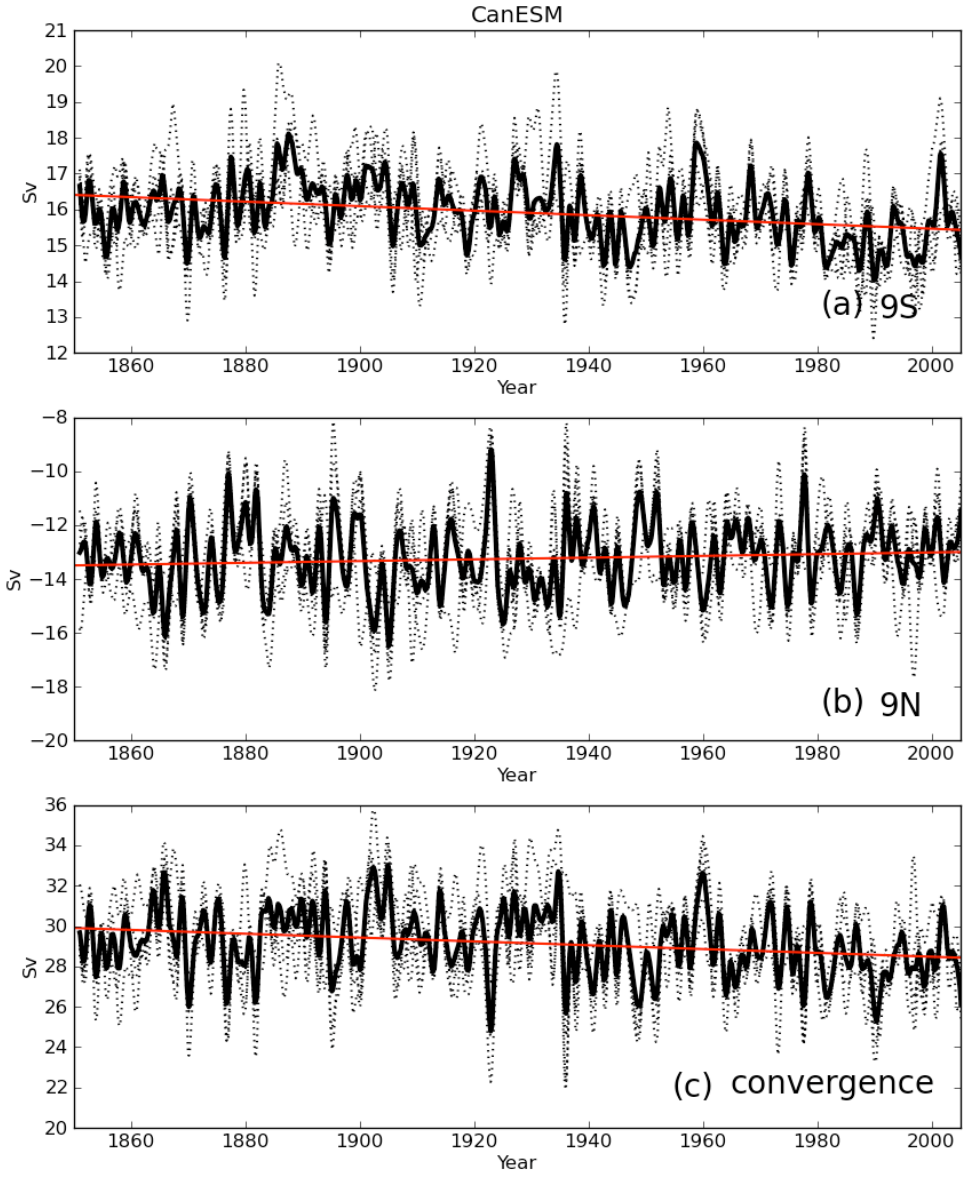

Figure A14. Transport of the STC in CanESM model at (a) 9°S, (b) 9°N, and (c) convergence transport between 9°S and 9°N. Dashed lines are for each ensemble members, and thick black is the ensemble mean.

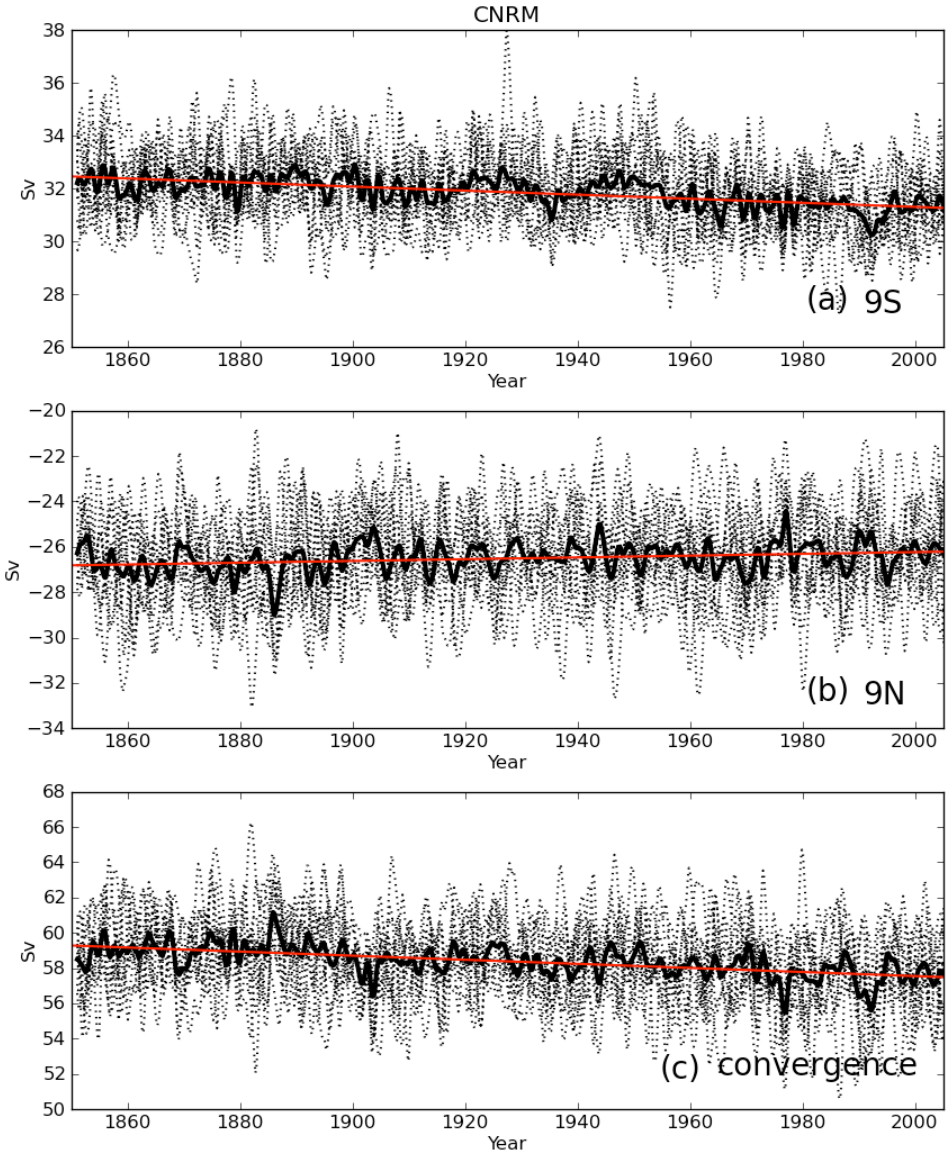

Figure A15. Transport of the STC in CNRM model at (a) 9°S, (b) 9°N, and (c) convergence transport between 9°S and 9°N. Dashed lines are for each ensemble members, and thick black is the ensemble mean.

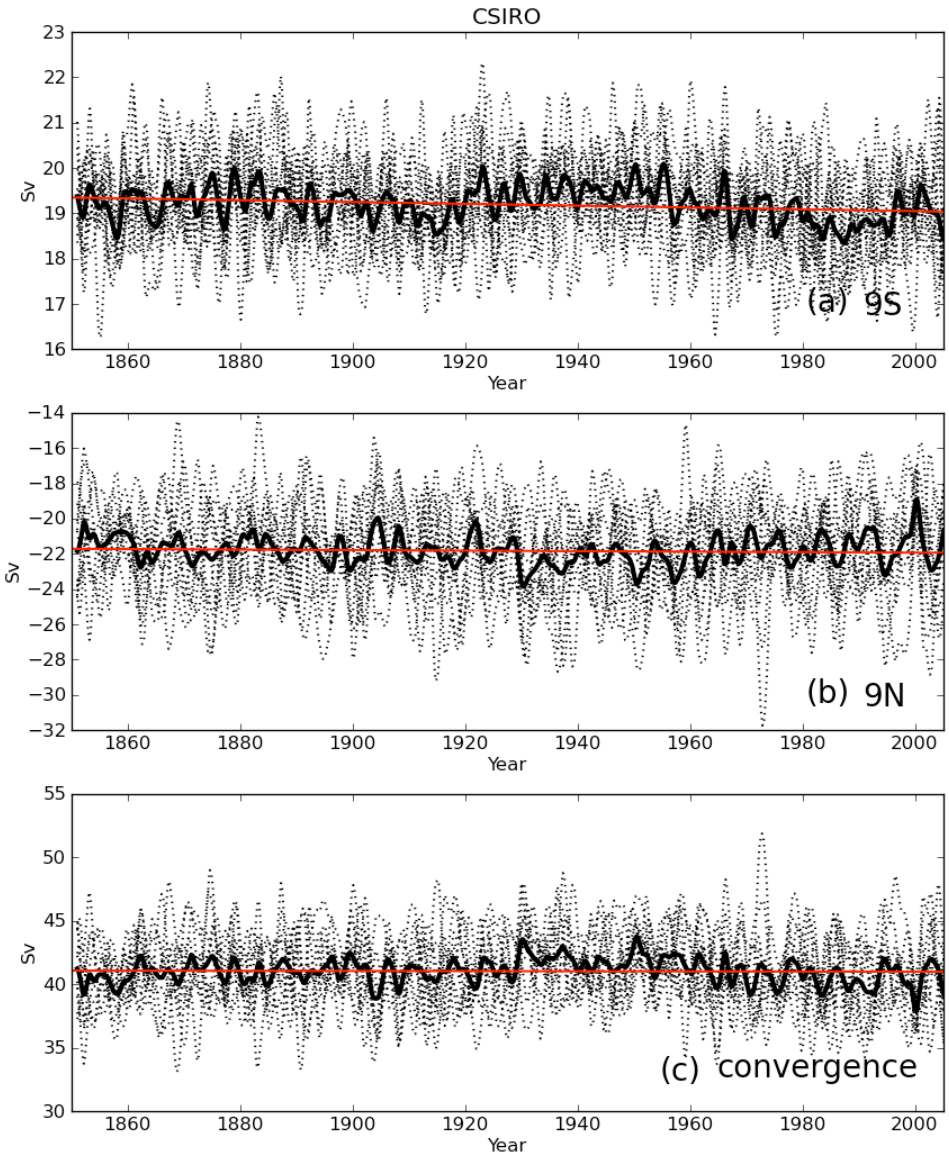

Figure A16. Transport of the STC in CSIRO model at (a) 9°S, (b) 9°N, and (c) convergence transport between 9°S and 9°N. Dashed lines are for each ensemble members, and thick black is the ensemble mean.

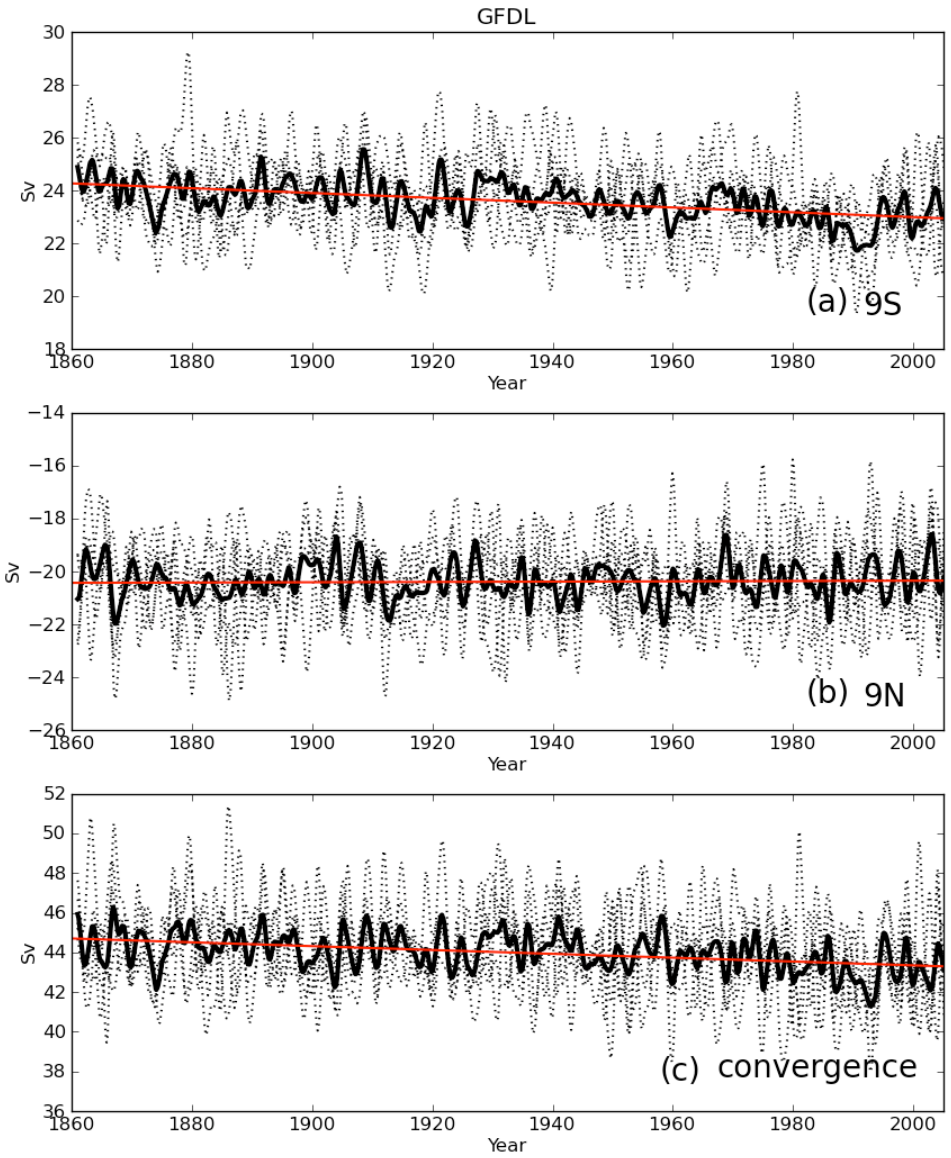

Figure A17. Transport of the STC in GFDL model at (a) 9°S, (b) 9°N, and (c) convergence transport between 9°S and 9°N. Dashed lines are for each ensemble members, and thick black is the ensemble mean.

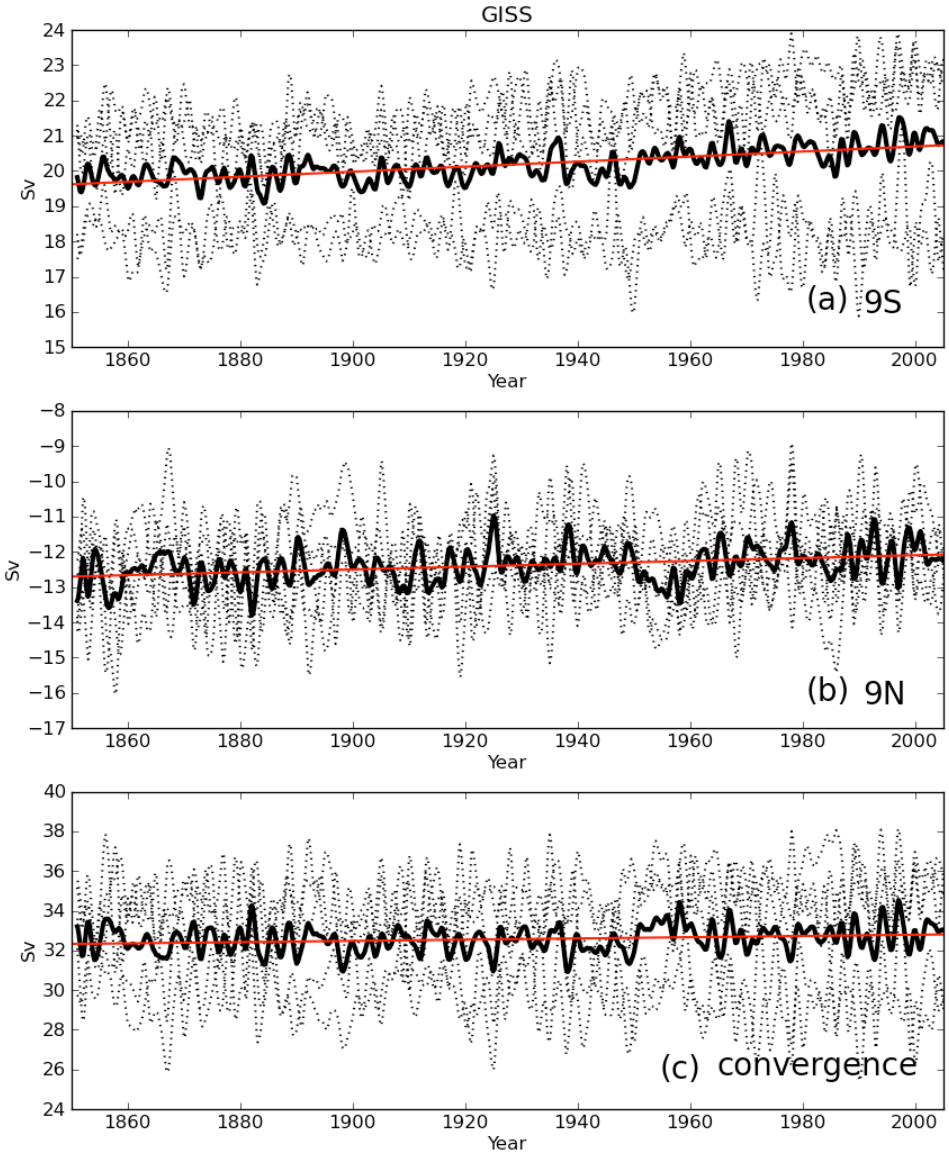

Figure A18. Transport of the STC in GISS model at (a) 9°S, (b) 9°N, and (c) convergence transport between 9°S and 9°N. Dashed lines are for each ensemble members, and thick black is the ensemble mean.

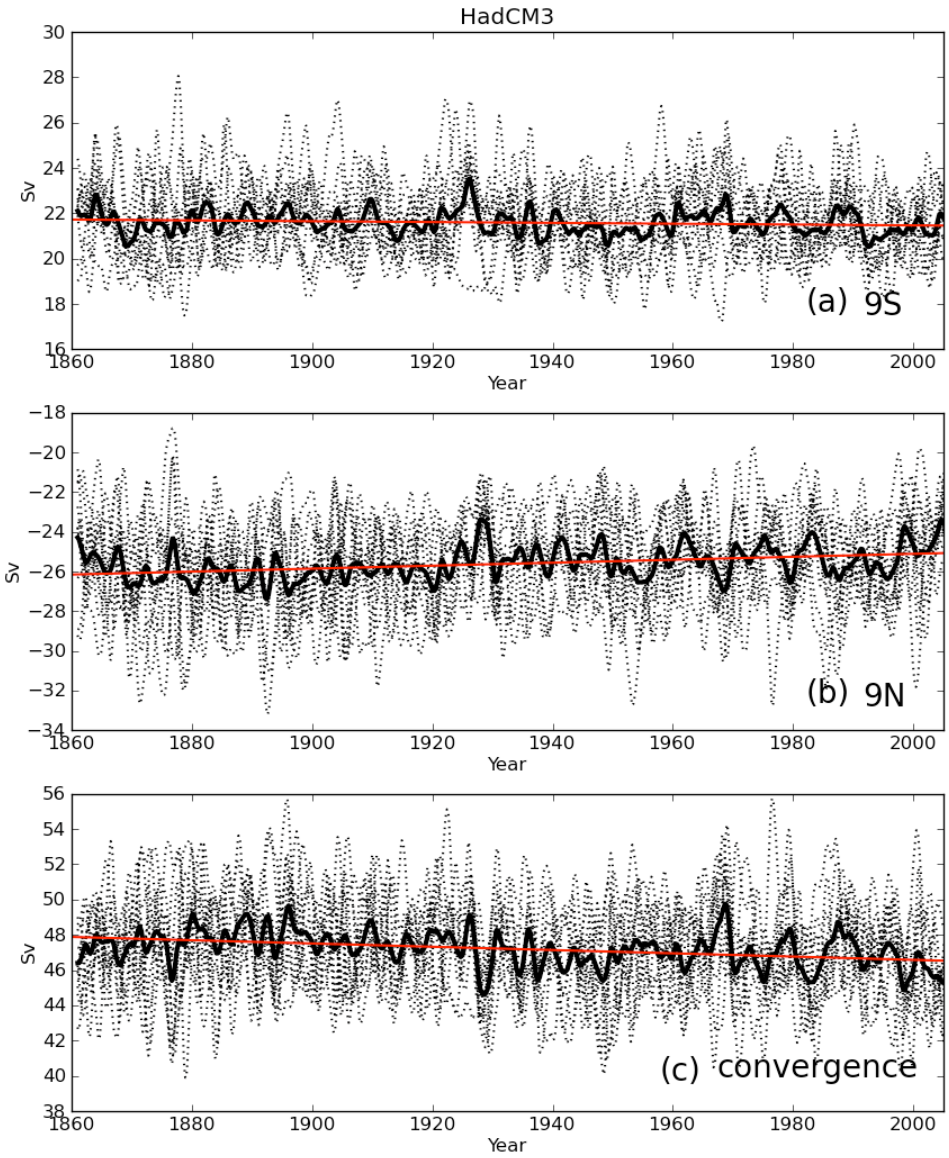

Figure A19. Transport of the STC in HadCM3 model at (a) 9°S, (b) 9°N, and (c) convergence transport between 9°S and 9°N. Dashed lines are for each ensemble members, and thick black is the ensemble mean.

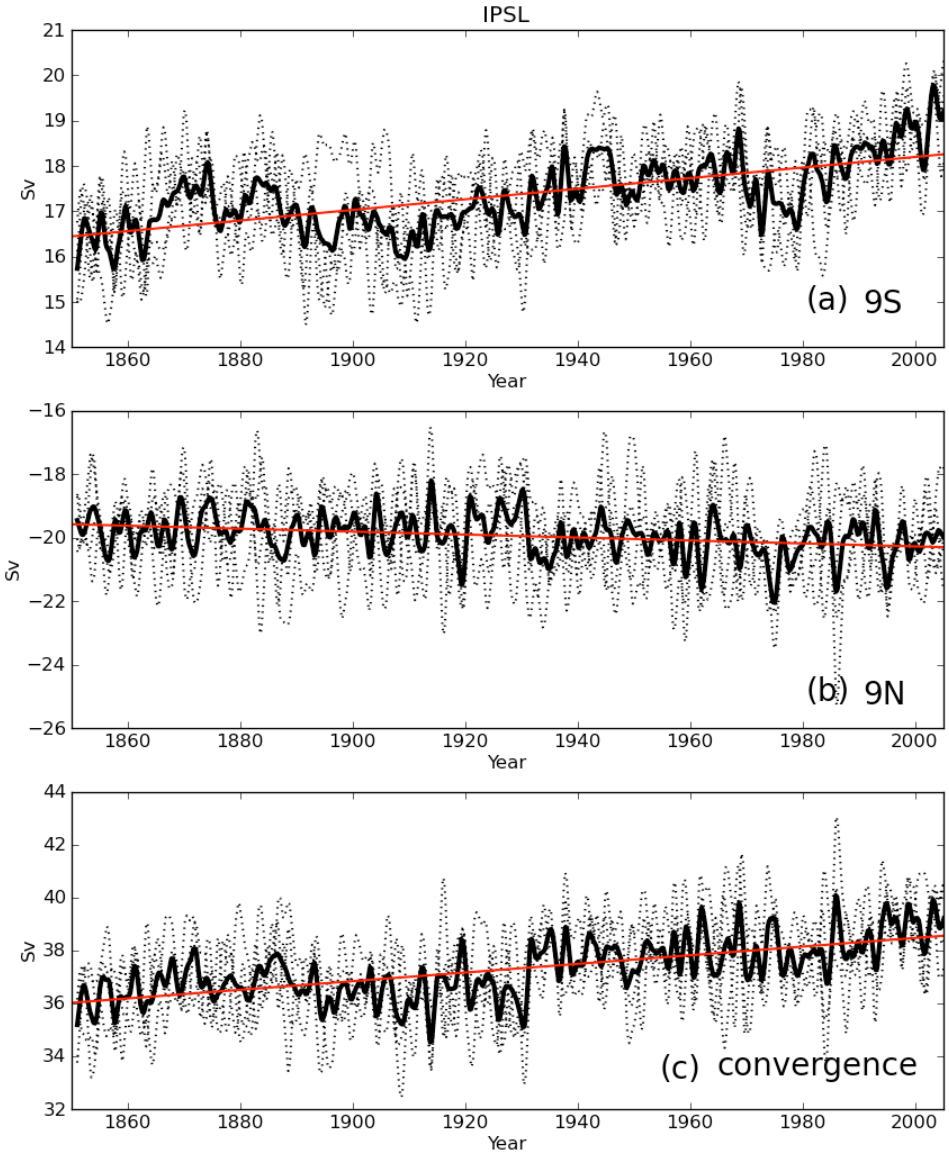

Figure A20. Transport of the STC in IPSL model at (a) 9°S, (b) 9°N, and (c) convergence transport between 9°S and 9°N. Dashed lines are for each ensemble members, and thick black is the ensemble mean.

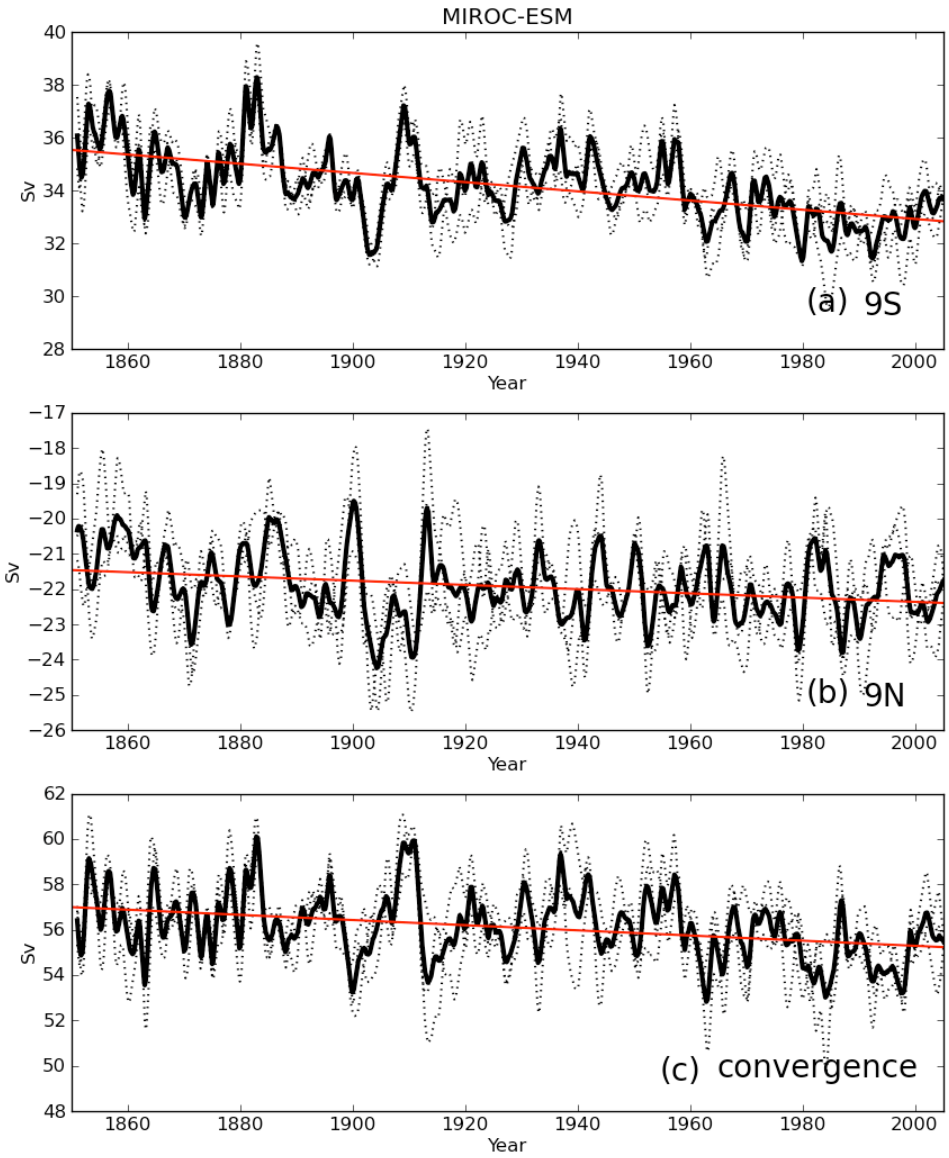

Figure A21. Transport of the STC in MIROC-ESM model at (a) 9°S, (b) 9°N, and (c) convergence transport between 9°S and 9°N. Dashed lines are for each ensemble members, and thick black is the ensemble mean.

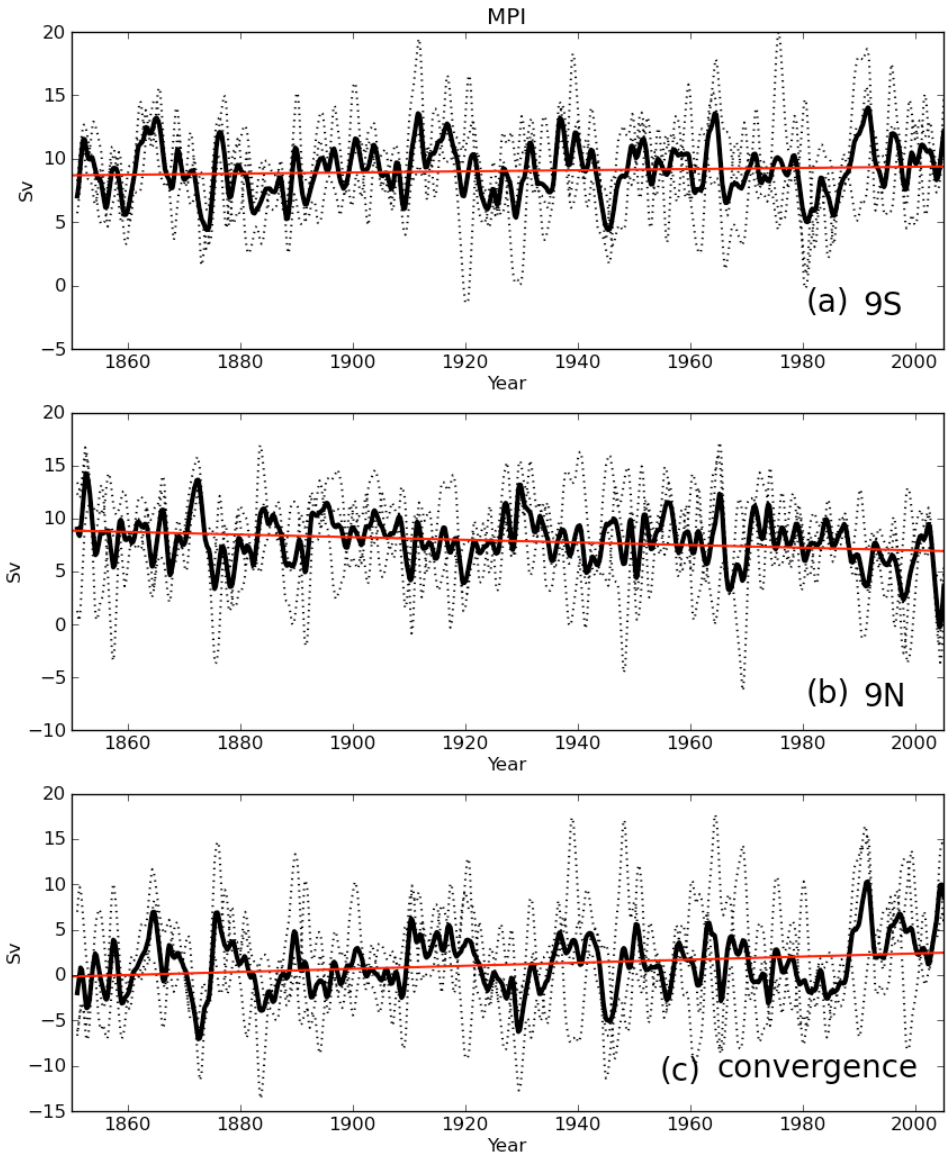

Figure A22. Transport of the STC in MPI model at (a) 9°S, (b) 9°N, and (c) convergence transport between 9°S and 9°N. Dashed lines are for each ensemble members, and thick black is the ensemble mean.

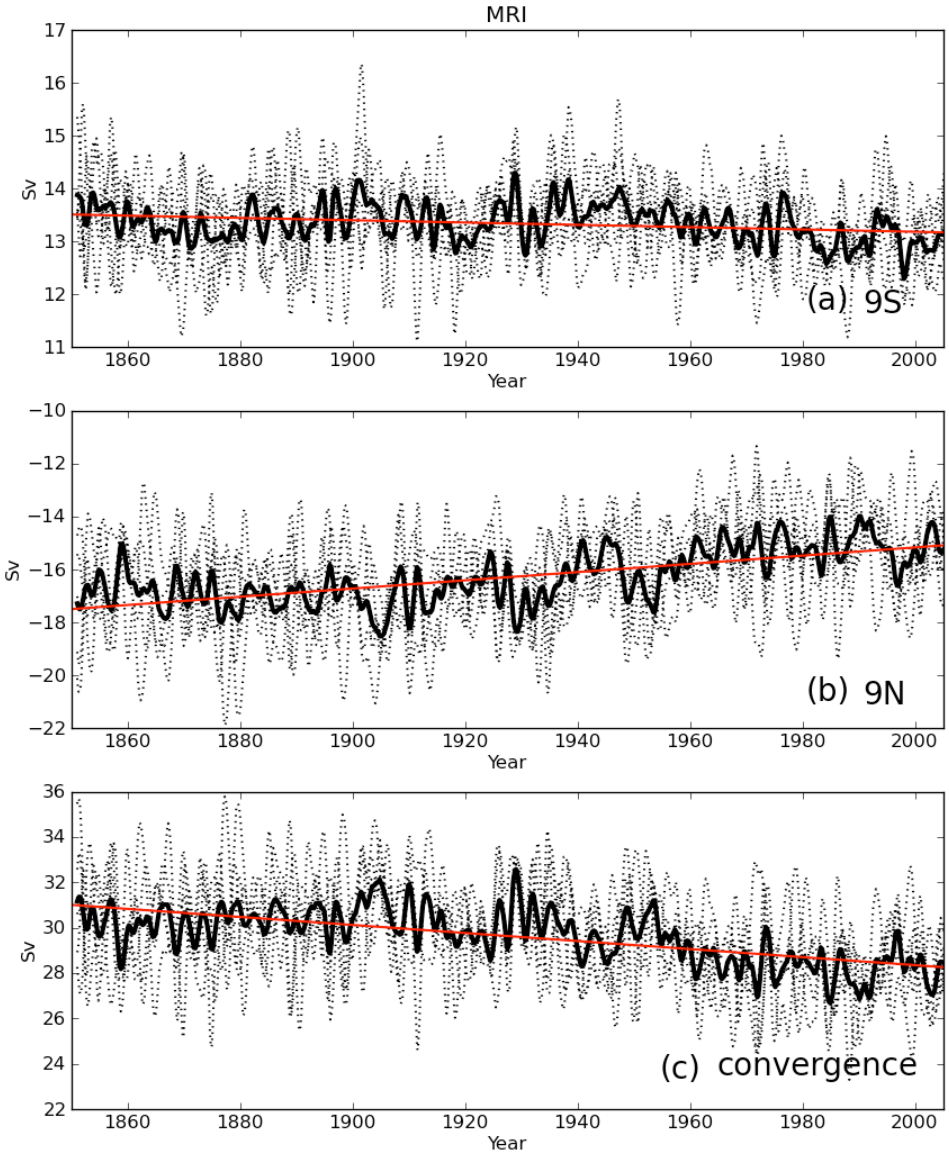

Figure A23. Transport of the STC in MRI model at (a) 9°S, (b) 9°N, and (c) convergence transport between 9°S and 9°N. Dashed lines are for each ensemble members, and thick black is the ensemble mean.

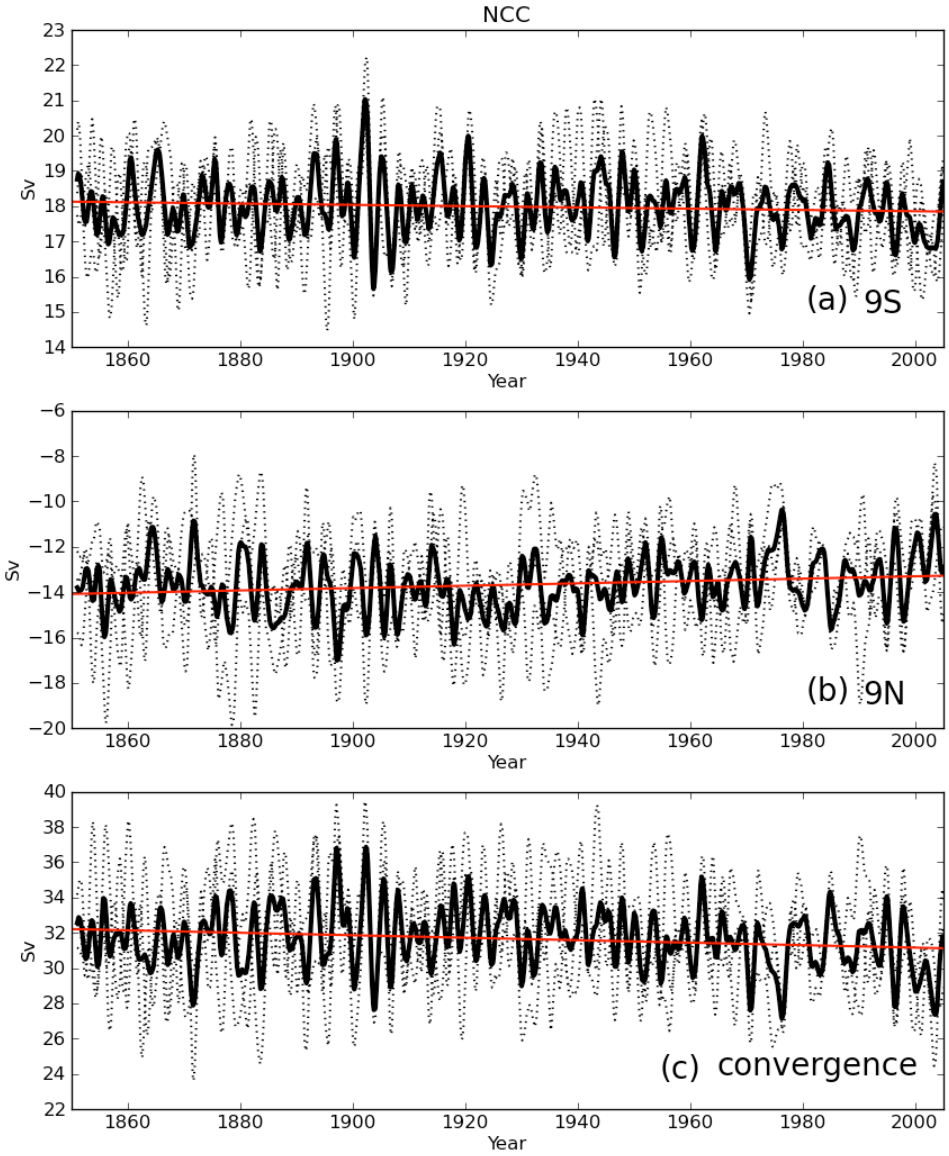

Figure A24. Transport of the STC in NCC model at (a) 9°S, (b) 9°N, and (c) convergence transport between 9°S and 9°N. Dashed lines are for each ensemble members, and thick black is the ensemble mean.